HIGH-STRAIN COMPOSITES AND DUAL-MATRIX COMPOSITE STRUCTURES

Thesis by

Ignacio Maqueda Jiménez

In Partial Fulfillment of the Requirements

for the Degree of

Doctor of Philosophy

California Institute of Technology

Pasadena, California

2014

(Defended May 12, 2014)

Dedicated to my parents, who always encouraged me to follow my dreams. And to Jennifer, for her love and support during these years.

Acknowledgments

First and foremost, I owe my deepest gratitude to my adviser, Professor Sergio Pellegrino. The research work presented in this thesis would not have been possible without his guidance and constant encouragement throughout the last four years. I especially appreciate the time and dedication he put into our discussions, which were always refreshing and motivating.

I would like to thank my thesis committee: Professor Guruswami Ravichandran, Professor Michael Ortiz, Professor Dennis Kochmann and Dr. Thomas Murphey. I really appreciate their advice and comments on my research. I deeply thank all my instructors at Caltech: Professor Dan Meiron, Professor Chiara Daraio, Professor Beverley McKeon, Professor Dale Pullin, Dr. Jay Polk, Professor Oscar Bruno, Professor Kaushik Bhattacharya, Professor Niles Pierce, Professor James Beck, Professor Joel Tropp and Professor Richard Murray. I also thank my Master year adviser, Professor Joseph Shepherd.

My special gratitude goes to Dr. Juan Mejia (L'Garde) for designing and manufacturing the materials studied in this thesis, and for his helpful insight regarding my research. I thank Professor Joseph Constantine (CalState Fullerton) for his input on the conical antenna shell design. I also thank Dr. Andrew Shapiro (JPL) for his helpful comments during our group meetings.

I would like to thank NASA and AFOSR for their financial support. My special gratitude goes to the Fulbright Foreign Student Program for giving me the opportunity to pursue my dreams. I am really privileged.

The staff at GALCIT has always been helpful. I am thankful to Petros Arakelian for his assistance with my experiments in the laboratory. I would also like to acknowledge Ms. Dimity Nelson, Ms. Christine Ramirez, Ms. Kate Jackson, Ms. Lydia Ruiz and Ms. Cheryl Gause, for all their support throughout these years.

I would like to thank the staff at the Registrar's Office, the Graduate Students Office, the International Students Office, and the Library. My thanks also go to the staff at Chandler and Red Door, especially to Martha and Elvira, who from the first day adopted me as another one of their

"Spanish children" at Caltech.

I want to acknowledge my colleagues at the Space Structures Laboratory. My deepest thanks go to Doctor Francisco López Jiménez and Doctor Chinthaka Mallikarachchi for their mentorship during my first couple of years at SSL. My thanks go also to Doctor Keith Patterson, Doctor Olive Stohlman, Doctor Kawai Kwok, Doctor Xiaowei Deng; and my current labmates Xin Ning, John Steeves, Lee Wilson, Manan Arya, Melanie Delapierre, Yamuna Phal and Kristina Hogstrom.

I would have not survived my first year at GALCIT without my classmates and friends: Terry Gdoutos, Victoria Stolyar, Kristen John, Namiko Saito, Andy Galvin, Jocelyn Escourrou and Philipp Oettershagen. I am especially thankful to the friends with whom I shared many great moments during my life at Caltech: Federico Tadei, Britton Sauerbrei, Laura and Benjamin Harrison, Jomela Meng, Stephanie Coronel, Landry Fokoua Djodom, Juan Pedro Méndez Granado, Adrian Sánchez Menguiano, and, last but not least, my roommate and great friend Siddhartha Verma.

I would like to thanks my friends and family from Spain, who have always supported me and welcome me back warmly whenever I flew back home.

My deepest gratitude goes to Jennifer Loesch, who has always encouraged and motivated me when I most needed it. I am truly fortunate for having her at my side.

Last, but most importantly, I want to thank my parents, who always encouraged me to follow my dreams. To them I owe everything I have accomplished. Thank you.

Abstract

Most space applications require deployable structures due to the limiting size of current launch vehicles. Specifically, payloads in nanosatellites such as CubeSats require very high compaction ratios due to the very limited space available in this typo of platform. Strain-energy-storing deployable structures can be suitable for these applications, but the curvature to which these structures can be folded is limited to the elastic range. Thanks to fiber microbuckling, high-strain composite materials can be folded into much higher curvatures without showing significant damage, which makes them suitable for very high compaction deployable structure applications. However, in applications that require carrying loads in compression, fiber microbuckling also dominates the strength of the material. A good understanding of the strength in compression of high-strain composites is then needed to determine how suitable they are for this type of application.

The goal of this thesis is to investigate, experimentally and numerically, the microbuckling in compression of high-strain composites. Particularly, the behavior in compression of unidirectional carbon fiber reinforced silicone rods (CFRS) is studied. Experimental testing of the compression failure of CFRS rods showed a higher strength in compression than the strength estimated by analytical models, which is unusual in standard polymer composites. This effect, first discovered in the present research, was attributed to the variation in random carbon fiber angles respect to the nominal direction. This is an important effect, as it implies that microbuckling strength might be increased by controlling the fiber angles. With a higher microbuckling strength, high-strain materials could carry loads in compression without reaching microbuckling and therefore be suitable for several space applications.

A finite element model was developed to predict the homogenized stiffness of the CFRS, and the homogenization results were used in another finite element model that simulated a homogenized rod under axial compression. A statistical representation of the fiber angles was implemented in the model. The presence of fiber angles increased the longitudinal shear stiffness of the material,

resulting in a higher strength in compression. The simulations showed a large increase of the strength in compression for lower values of the standard deviation of the fiber angle, and a slight decrease of strength in compression for lower values of the mean fiber angle. The strength observed in the experiments was achieved with the minimum local angle standard deviation observed in the CFRS rods, whereas the shear stiffness measured in torsion tests was achieved with the overall fiber angle distribution observed in the CFRS rods.

High strain composites exhibit good bending capabilities, but they tend to be soft out-of-plane. To achieve a higher out-of-plane stiffness, the concept of dual-matrix composites is introduced. Dual-matrix composites are foldable composites which are soft in the crease regions and stiff elsewhere. Previous attempts to fabricate continuous dual-matrix fiber composite shells had limited performance due to excessive resin flow and matrix mixing. An alternative method, presented in this thesis uses UV-cure silicone and fiberglass to avoid these problems. Preliminary experiments on the effect of folding on the out-of-plane stiffness are presented. An application to a conical log-periodic antenna for CubeSats is proposed, using origami-inspired stowing schemes, that allow a conical dual-matrix composite shell to reach very high compaction ratios.

Contents

List of Figures

List of Tables

Chapter 1

Introduction

1.1 Deployable space structures

Deployable structures are structures that can be packaged into a smaller size for transportation or storage. Applications that require large structures in space are often limited by the size of the launch vehicle, so the use of deployable structures is necessary. Examples of large deployable structures are solar panels, solar sails, solar concentrators and reflector antennas.

Figure 1.1: Astromesh reflector. Courtesy of Northrop Grumman.

Several techniques can be used to design deployable structures. Some structures make use of stiff elements connected by mechanical joints to facilitate their relative motion between the members and are actuated with motors or driven by springs. These structures tend to be complex and expensive. An example of this type of structure is the Astromesh reflector (see Figure 1.1), which is an assembly of cables and pairs of rods with intermediate connections that lock when the structure reaches the deployed configuration.

Other deployable structures use thin (shell) elements that deform elastically. This method allows the structure to deploy autonomously without the use of heavy mechanical joints or actuators, as it stores strain energy during stowage. This type of structure allows for curvatures up to the elastic range of the materials. The simplest flexible shell concept is the STEM (Stored Tubular Extendible Member), invented in Canada in the 1960s. Another example of this type of structure is the Hughes Spring Back Reflector, which is a single-piece shell structure that folds elastically around a central axis, like a taco shell (Figure 1.3).

Figure 1.2: DLR CFRP boom, taken from [58].

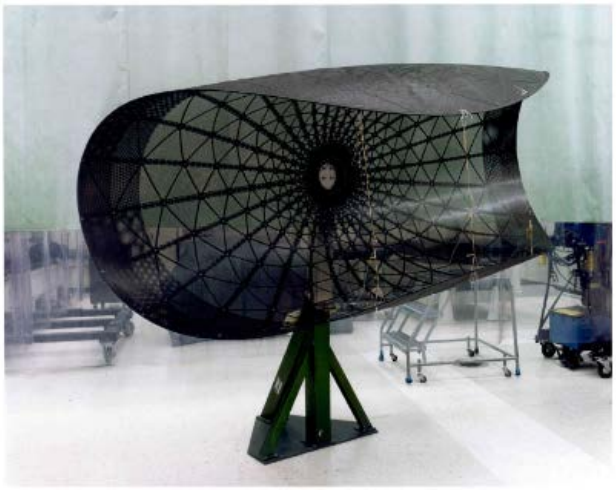

Figure 1.3: Hughes Spring Back Reflector, courtesy of Boeing.

Other deployable structures such as inflatables and rigidizables are able to reach very high compaction. However, they cannot be deployed passively, as they require the presence of external systems, such as gas injection or heating.

1.2 High-strain composites used in deployable space structures

The development of fiber composites led to the design of thinner, lighter structures with higher stiffness and strength, which allow for higher stowage curvatures, better compaction ratios and autonomous deployment capabilities. However, there is a limitation on the curvatures that traditional, high-performance composite materials can reach, which limits the degree of compaction that can be achieved in deployable structures based on such materials. The failure strain of carbon fiber composites is in the range of $1 - 1.5\%$, with corresponding limits on the bend ratio (the ratio of the bending radius over the thickness) of 35-50. The corresponding values of $\kappa_{max}t$ are 0.02-0.03, where κ_{max} is the maximum curvature, and t is the thickness of the composite.

High-strain composites are materials in which the fibers are embedded in a soft, elastomeric matrix. High-strain composites are commonly used in applications such as car tires and biological tissues, and have also been proposed for novel aerospace applications, such as morphing wings [50] or as a substitute for mechanical hinges or joints. These materials are able to reach higher values of $\kappa_{max}t$ when folded, due to elastic microbuckling of the fibers in compression, which acts as a stress relief mechanism that avoids fiber breakage (Murphey et al. [45]). Additionally, these materials can retain enough strain energy to self-deploy. Therefore, they can be used as flexure hinges to connect different parts of a foldable structure, providing an almost equivalent function to a mechanical hinge.

Microbuckling has been experimentally observed through folding of rigidizable composites (Campbell et al. [9], Mejia et al. [38]) or silicone composites (Datashvili et al. [14], Figure 1.4). Previous studies by López Jiménez and Pellegrino [34, 33] analyze the folding mechanism and behavior under transverse tension of unidirectional carbon fiber-reinforced silicone (CFRS). Values of $\kappa_{max}t$ up to 0.4 were estimated in high strain composites with AS4 fibers and a silicone matrix for a probability of 1% fiber failure in the most compressed layer of a lamina under bending [33].

Murphey compared stiffness-based and concentrated strain-based performance metrics of unidirectional traditional composites and high-strain composites for flexure hinge applications [44]. These metrics were based on the maximum strain achievable for the material under bending and the composite stiffness in the fiber direction. While showing a similar stiffness-related behavior, concentrated strain-based performance in high-strain composites is 5 to 10 times superior than in traditional composites.

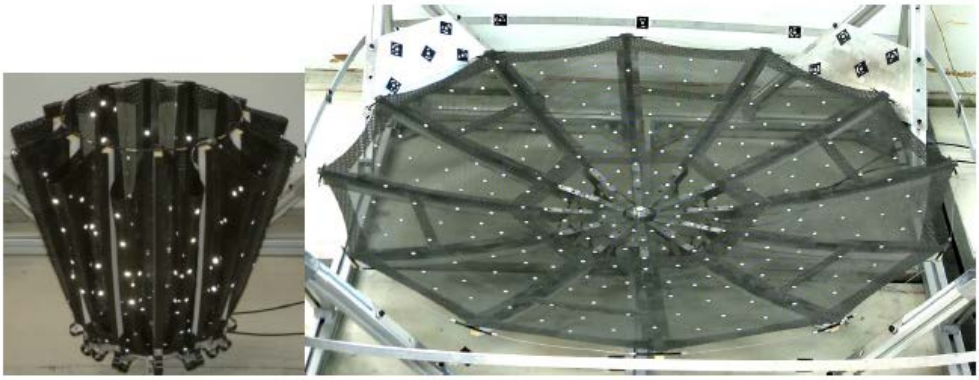

Figure 1.4: SMART (Shield-membrane antenna reflector technology) demonstrator, taken from [14]. The reflector is made of triaxial weave carbon fiber-reinforced silicone.

1.3 Motivation

An important mechanical property for the design of flexure hinges for deployable trusses is the strength in compression of the material. For a high-strain composite, the strength in compression is controlled by fiber microbuckling, which occurs at a much lower stress than the failure in compression of traditional composites. However, the flexure folding capability and its buckling load need to be taken into account to understand the performance of the two different materials in a flexure hinge application, such as the one presented in Mejia and Murphey [39].

For this comparison, two slender flexural hinges attached to a solid strut are considered. They are part of a deployable structure that requires each hinge to fold 90^o. The hinges have a length L, a width w, and a thickness t. In the deployed configuration, the hinges are required to carry a compressive force. The Euler buckling stress of the strut is assumed to be much higher than the hinges.

Two materials are considered for the hinges. One is a traditional composite with a longitudinal stiffness $E_1 = 100$ GPa and a maximum strain $\epsilon_{max} = 1.5\%$. For this material, $\kappa_{max}t = 0.03$. The other material considered is a high-strain composite with a longitudinal stiffness $E_1 = 100$ GPa and a $\kappa_{max}t = 0.4$, as was found in López Jiménez and Pellegrino [33].

The length of the hinges is calculated as the minimum length needed for them to fold 90^o. This minimum length is obtained when the maximum curvature is reached:

$$L = \frac{\pi}{2}\frac{1}{\kappa_{max}} = \frac{\pi}{2}\frac{t}{\kappa_{max}t}. \tag{1.1}$$

For the traditional composite hinge, $\kappa_{max}t = 0.03$, and the minimum length is

$$L_{\text{traditional}} = 16.6\pi t, \tag{1.2}$$

whereas for the high-strain composite hinge, with $\kappa_{max}t = 0.4$,

$$L_{\text{high-strain}} = 1.25\pi t, \tag{1.3}$$

The Euler buckling stress of the hinges is given by

$$\sigma_{crit} = \frac{\pi^2 E_1 I}{A(2L)^2}, \tag{1.4}$$

where A is the cross-sectional area of the hinge, $A = wt$, and I is the area moment of inertia, $I = wt^3/12$. Substituting the values of L, A, and I, the Euler buckling stress are:

$$(\sigma_{crit})_{\text{traditional}} = \frac{E_1}{13333} = 7.5 \text{ MPa} \tag{1.5}$$

$$(\sigma_{crit})_{\text{high-strain}} = \frac{E_1}{75.5} = 1.3 \text{ GPa}. \tag{1.6}$$

For the high-strain composite hinge, the critical Euler buckling stress is much higher than the strength in compression, actually dominated by fiber microbuckling. Typical values of fiber microbuckling strength found in this thesis (for unidirectional carbon fiber embedded in a 1-MPa modulus silicone matrix) are in the range 4-6 MPa, which makes the high-strain hinge strength in compression lower than the traditional composite hinges Euler strength. Stronger and thinner fibers would allow high-strain composites to achieve higher values of $\kappa_{max}t$.

Peel found that fiber angle changes in multidirectional laminates of high-strain composites allowed to obtain extreme Poisson's ratio, both positive and negative [49]. The fact that some mechanical properties of high-strain composites are very sensitive to the fiber direction suggest that the microbuckling strength might be also sensitive.

This thesis aims to characterize the onset of fiber microbuckling under pure compression of a high-strain composite material with experimental measurements and numerical simulations through homogenization of the microstructure. The effect of the fiber angles with respect to the nominal

fiber direction on the microbuckling strength is also studied. Finite element results suggest that the fiber microbuckling strength can reach values of $\sim$ 40 MPa for some fiber angle distributions with a very small standard deviation $\sim 1^o$, and a elastomeric matrix with a 1-MPa modulus. Modifying the fiber angle could potentially make high-strain composites suitable for flexural hinges that carry compression loads. Another approach to increase the strength of the composite is to use an elastomeric matrix with higher stiffness. Alternatively, these composites may be suitable for tension-carrying foldable connectors in trusses, in which the strength in compression is not critical.

High-strain composites can also be used as self-deployable shell structures such as the Shell-Membrane Reflecting Surface (Figure 1.4). These structures have excellent compaction capabilities, but they are characterized for their low out-of-plane stiffness. The concept of dual-matrix composite shells, in which the soft material is localized in the hinge lines, while traditional composites are elsewhere, improves the stiffness out-of-plane while allowing the shell to be foldable. First attempts to manufacture dual-matrix composite shells were limited due to the excessive resin flow and curing inhibition. This thesis presents an alternative technique, which uses UV-cure silicone and epoxy on a fiberglass composite and avoids the issues previously stated.

The use of dual-matrix composite shells on self-deployable antennas for CubeSats is also discussed. The limiting stowage size in CubeSats make these shells very advantageous as deployable structures in this type of platform. In particular, the design of a origami-inspired foldable antenna for a CubeSat mission using dual-matrix shells is discussed.

1.4 Outline

This thesis contains two studies on high-strain composite materials. The first one, which comprises chapters 2 through 6, addresses the behavior in compression of unidirectional carbon fiber-reinforced silicone (CFRS). The final chapters focus on dual-matrix partially-foldable composite shell structures, and their application on a self-deployable antenna structure for a CubeSat.

Chapter 2 presents a review of existent models for instabilities in compression of unidirectional fiber composites.

An experimental characterization of the microstructure and mechanical properties of unidirectional CFRS can be found in Chapter 3, with a focus on the failure in compression of CFRS rods.

Chapter 4 presents two homogenization models used to calculate the effective mechanical properties of the material, and describes their numerical implementation and results. The homogenization results from chapter 4 are used to simulate the instability in compression of a CFRS rod. The description of the finite element model, along with the results of the simulations, can be found in Chapter 5.

Chapter 6 treats dual-matrix composite shells. The manufacturing, estimation of the mechanical properties, and experimental study of the behavior out-of-plane of pre- and post-folded shell are described in this chapter. Examples of concepts of dual-matrix structures are mentioned.

One of the concepts described in chapter 6 is addressed more deeply in chapter 7, which considers the use of a dual-matrix structure to support a self-deployable UHF log-periodic antenna for a CubeSat. The mechanical properties obtained in chapter 6 are used here to perform a vibration analysis of the structure.

Finally, chapter 8 summarizes and concludes this thesis.

Chapter 2

Background

The compression instability of unidirectional fiber composites is a problem that has been extensively investigated. This chapter reviews the most relevant models for failure in compression found in the literature, and discusses their applicability for soft matrix composites. Some of the models reviewed here will be used in later chapters and compared with experimental and numerical results for the composite material studied in this thesis.

The failure mechanism known as fiber microbuckling acts in a special way in high-strain fiber composites, providing a relief mechanism that avoids fiber breakage when the composite is folded to large curvatures. This property makes this type of material advantageous in deployable structures. A review of studies in the mechanics of high-strain composites is provided here as well.

2.1 Compression instability of unidirectional composites

Unidirectional composites are characterized as being anisotropic, i.e., their material properties are directionally dependent. In particular, they are orthotropic materials, as they present two planes of symmetry. The stiffness and strength are larger in the direction of the fibers.

This thesis studies the compression instability of unidirectional CFRS rods whose axes coincide with the fiber and loading direction. For this reason, the first model to consider is Timoshenko and Gere's solution for a homogeneous anisotropic column in compression [62]. This model considers the effect of the shearing force acting on the cross sections of the column during buckling. The shearing force is

$$Q = P\frac{dy}{dx}, \tag{2.1}$$

where $y(x)$ is the lateral deflection of the column and P is the compressive load. The total curvature of the deflection is given by adding the curvature due to the bending moment and the curvature due to the shearing force:

$$\frac{d^2y}{dx^2} = \frac{P(\delta - y)}{EI} + \frac{nP}{AG}\frac{d^2y}{dx^2}, \tag{2.2}$$

where the second term in the right-hand side of the equation represents the rate of change in slope of the deflection due to the shearing force. The geometrical factor is $n = 1.2$ for a rectangular cross-section, and is $n = 1.11$ for a circular cross-section; δ is the end deflection, G is the shear stiffness of the beam, A is the cross-sectional area, and EI is the bending stiffness of the column. If the material is orthotropic, E is the stiffness in the axial direction. Equation (2.2) can be solved by assuming sinusoidal solutions for the deflection, similarly to the classic Euler buckling solution, obtaining a critical load

$$P_{cr} = \frac{P_e}{1 + nP_e/AG}, \tag{2.3}$$

where P_e is the Euler buckling load, $P_e = \pi^2 EI/4l^2$, where l is the length of the column. For highly orthotropic materials, as in the case of high-strain composites, values of $E/G \sim 10^5$ can exist, and hence the resulting critical load can be extremely small in comparison to the Euler buckling load.

Other models focus on the micromechanics of the unidirectional composite in order to understand the failure in compression. The theory of fiber microbuckling was originally developed by Rosen, who studied the onset of compression instability in fiber composites, assuming that the fibers buckle as columns on a elastic foundation [55]. Fiber microbuckling can occur in two modes. The first is called extension mode, in which the fibers buckle in phase, while the second is called shear mode, in which the fibers buckle out of phase (Figure 2.1).

Rosen studied the stability of a two-dimensional array of layers with fibers of modulus E_f and matrix of modulus E_m. By making use of the energy method, the strain energy of fiber and matrix has to be equal to the work done by the compressive loads:

$$\Delta U_f + \Delta U_m = \Delta T \tag{2.4}$$

In the cases studied, all the fibers are buckling with the same wavelength, with adjacent fibers

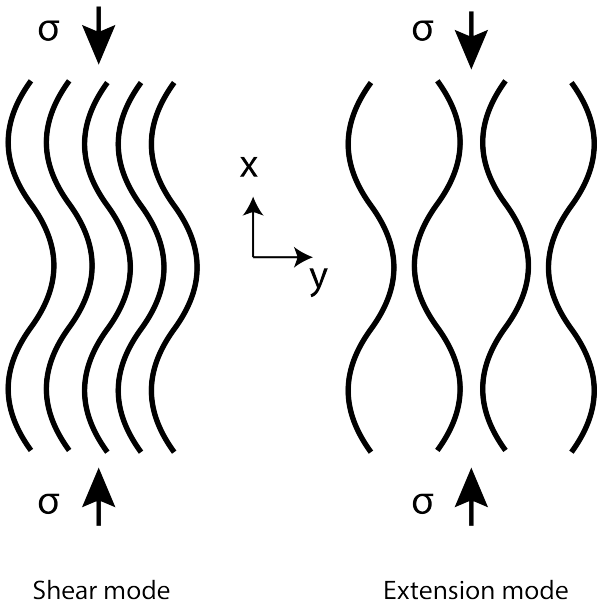

Figure 2.1: Modes of fiber microbuckling: shear and extension. Initially, fibers are straight and parallel to the x axis.

either in-phase or out-of-phase. The fibers are assumed to buckle as a sinusoid of wavelength λ,

$$v = a \sin \frac{x}{\lambda}. \tag{2.5}$$

The fibers shear deformations are neglected, as they are assumed to be relatively stiff compared to the matrix. Hence, the strain energy of the fibers can be computed as

$$\Delta U_f = \frac{\pi^2 a^2 E_f}{48 L^3}. \tag{2.6}$$

In extension mode, the strain energy of the matrix is given by the transverse strain, as the axial and shear stresses are neglected. Therefore,

$$\Delta U_{m,ext} = \frac{1}{2} \int_V \sigma_y \epsilon_y dV = \frac{a^2 E_m \lambda}{2c}, \tag{2.7}$$

as the transverse strain is $\epsilon_y = v/c$, where $2c$ is the distance between two fibers.

The change in strain energy of the matrix associated with the shear mode of microbucking can

be calculated, assuming the shear strains are a function of only the longitudinal coordinate, as

$$\gamma_{xy} = \partial u_y/\partial x + \partial u_x/\partial y = \left(1 + \frac{h}{2c}\right) du_y/dx, \tag{2.8}$$

where h is the fiber thickness. The strain energy is given by

$$\Delta U_{m,sh} = \frac{1}{2}\int_V \tau_y \epsilon_y dV = \frac{a^2\pi^2 G_m c}{2\lambda}\left(1 + \frac{h}{2c}\right). \tag{2.9}$$

Finally, the work done by the external forces depends on the compression load and the fiber deflection

$$\Delta T = \pi^2 a^2 P/4\lambda. \tag{2.10}$$

Equations (2.10), (2.6) and (2.7) for microbuckling in extension or (2.9) for microbuckling in shear can be substituted in Equation (2.4) to obtain the critical stress. The microbuckling critical stress for the extension mode is

$$\sigma_{cr,ext} = 2V_f\left[\frac{V_f E_m E_f}{3(1-V_f)}\right]^{(1/2)}, \tag{2.11}$$

where $V_f = h/(h+2c)$ is the fiber volume fraction, and the composite critical stress is $\sigma_{cr} = V_f \sigma_{cr,fibers}$. The critical stress for the shear mode is

$$\sigma_{crit} = \frac{G_m}{1-V_f} + \frac{\pi^2 V_f E_f h^2}{12\lambda^2}. \tag{2.12}$$

For wavelengths that are large compared to the fiber diameter, the buckling stress is approximated to the classical expression

$$\sigma_{crit} = \frac{G_m}{1-V_f} = G, \tag{2.13}$$

where G is the shear modulus of the composite. Rosen showed that for most composites the fibers only microbuckle in extension if the fiber volume fraction is small ($V_f \leq 0.2$), as the critical stress for the shear mode is lower. Rosen's shear mode of microbuckling has been used extensively to predict the failure strength of fiber composites, but it overpredicts the compression strength by as much as 200% [3].

Waas et al. [66] modeled the buckling of a single fiber and of a composite of n layers in an

elastic foundation, considering the presence of a free surface. The authors found that the minimum buckling stress was given for a sinusoidal buckle with a finite wavelength for both single fiber and laminate models. Thus, they concluded that the presence of free surfaces affects Rosen's solution for the microbuckle critical stress, and that the microbuckling wavelength is not necessarily infinite. Through a 2-D analysis of the matrix stress/strain fields, Parnes and Chiskis showed that the extension mode of microbuckling is spurious [48] . They also stated that for common composites, where $E_f/E_m < 10^2$, elastic microbuckling is not a realistic mechanism, as Rosen's model predicts failure strains that are too high compared to the elastic range of the materials.

This idea had been previously explored by Argon [2], Budiansky [7] and Budiansky and Fleck [8], introducing the concept of plastic microbuckling. Under plastic microbuckling, the compressive strength is controlled by the fiber misalignment and the plastic shear deformation of the matrix. Argon's value for the compression strength is

$$\sigma_{crit} = \frac{k}{\bar{\phi}}, \tag{2.14}$$

where k is the shear yield strength of the composite, and $\bar{\phi}$ is the misalignment of the fibers inside a band of infinite length, width w, and an angle $\beta = 0$, with respect to the fiber direction. This expression was extended by Budiansky to an elastic-perfectly plastic composite, with yield strain $\gamma_y = k/G$ in longitudinal shear [7]:

$$\sigma_{crit} = \frac{G}{1 + \bar{\phi}/\gamma_y}. \tag{2.15}$$

Experimental results found in the literature were summarized by Fleck, supporting the hypothesis that microbuckling is a plastic rather than an elastic event for common matrix polymer composites [19]. Kyriakides showed the presence of kink bands in unidirectional composite rods after being tested in compression, and confirmed that the most complex analysis assuming perfectly aligned fibers triplicates the failure strain found in experiments [29]. Barbero and Tomblin estimated the failure in compression using a non linear shear stress-strain law that considered the effect of the fiber misalignment distribution and the matrix shear strength [4]. Finite element simulations were done by Drapier et al. using a homogenized medium to study the influence of the initial misalignment, ply thickness, laminate stacking, and loading type [16, 17]. They showed that

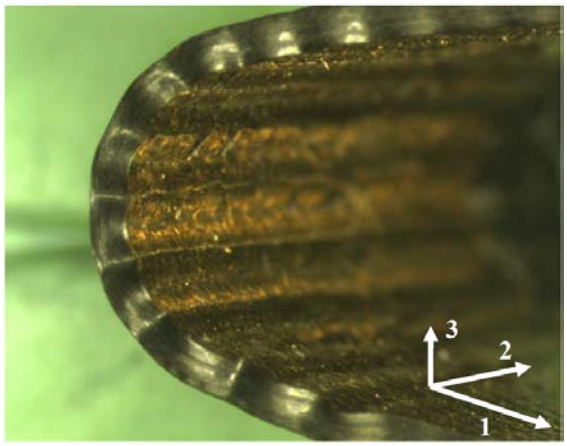

(a) Elastic microbuckling of the compression side of a folded elastic memory composite, taken from Francis et al. [20]

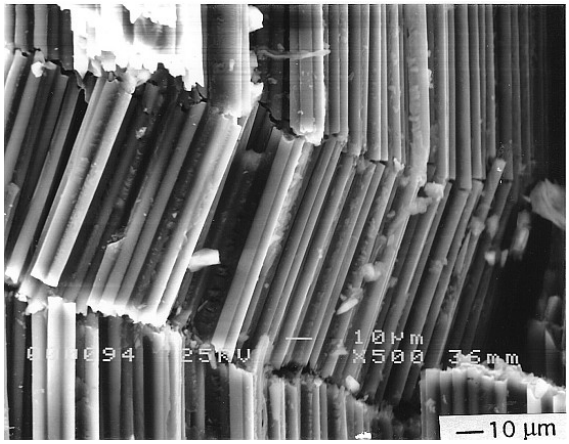

(b) Kink band of a fiber composite after plastic microbuckling, taken from [13].

Figure 2.2: Examples of failure modes in compression of unidirectional composites.

the development of microbuckling is heterogeneous along the thickness, which explains why the strength is high in bending.

Fiber crushing is another mode of compression failure in composites. When the matrix is relatively stiff and strong in comparison to the fibers, the uniaxial strain can reach the crushing strain of the fibers. The failure in the fibers can be due to plastic yielding in metallic fibers, longitudinal splitting in glass fibers, or microscopic microbuckling and kinking in carbon, Kevlar, or wood fibers [19].

The matrix can also fail in compression through a splitting mode, whose strength depends on the mode I fracture toughness of the matrix and the size and number of voids. Delamination in compression of layered composites is another possible mode of compressive failure.

2.2 Compression instability in high-strain composites

In common composites, the failure in compression is dominated by the matrix strength. However, if the matrix is compliant enough, as is the case in high strain composites, the composite reaches instability in compression through elastic microbuckling. Christensen found that Rosen's estimate is more accurate when the material is highly anisotropic, i.e., the ratio between the longitudinal and transversal stiffness of the material is large [10]. DeBotton and Schulgasser determined a third-order

approximation for the critical strength of a linear elastic orthotropic solid, which asymptotically approaches Rosen's estimation for large ratios of stiffness [15]. Jelf and Fleck fabricated composite materials made from baked wheat flour (spaghetti), which reinforced a silicone elastomeric matrix [27]. Testing a flat specimen in pure compression, they found in-plane microbuckling with a wavelength twice the specimen height, obtaining a compressive strength in good agreement with Rosen's formula.

In this section, several models that predict the instability or failure in compression of anisotropic materials are described. Some models predict the macroscopic onset of instability, i.e., for the homogenized, effective materials; while others predict the microscopic onset of failure, i.e., at the microstructural level.

2.2.1 Macroscopic instabilities

Extensive research has been focused on developing models to understand the instabilities of finitely-deformed transversely isotropic elastic materials. Triantafyllidis and Abeyaratne [64] and Merodio and Ogden [40, 41] studied the loss of ellipticity of the homogenized response given by the strain energy defined by the principal scalar invariants of the right Cauchy-Green tensor ($C = F^T F$):

$$W(I_1, I_2, I_3, I_4, I_5) = W_{iso}(I_1, I_2, I_3) + W_{ani}(I_4, I_5), \tag{2.16}$$

where I_1, I_2 and I_3 are the invariants that represent the isotropic material (matrix), while I_4 and I_5 represent the anisotropoc reinforcement (fibers).

Geymonat et al. demonstrated that the onset of macroscopic instabilities (with a wavelength much larger than the characteristic size of the microstructure) can be determined from the loss of strong ellipticity of the homogenized response of a heterogeneous hyperelastic material [24]. Additionally, the microscopic instabilities are a rigorous upper bound to the onset of microscopic instabilities. Triantafyllidis and Schnaidt found that the global instabilities dominate when the matrix stiffness is below a threshold [65]. In this case, the critical strength of the periodic representative unit cell is higher than the global critical strength, of much higher instability wavelength.

To determine the onset of macroscopic instabilities, Ponte Castañeda introduced the second-order homogenization methods in the context of small-strain nonlinear elasticity [51, 52]. One method uses a tangent linearization valuated at the phase average of the deformation, and the

other uses a generalized secant linearization. These methods were extended to finite deformation elasticity applied to reinforced elastomers by Ponte-Castañeda and Tiberio [53] and by López-Pamiés and Ponte-Castañeda [35].

Agoras et al. [1] and Rudykh and deBotton [56] derived the same expression for the critical compressive stretch ratio in the fiber direction of a two-dimensional transversely isotropic composite with incompressible Neo-Hookean phases, using Ponte Castañeda's second-order homogenization and a nonlinear comparison variational method, respectively. The authors found that the critical stretch ratio applying the strong ellipticity condition is:

$$\lambda_{crit} = \left(1 - \frac{\tilde{G}}{\bar{G}}\right)^{1/3}, \tag{2.17}$$

where $\tilde{G}$ and $\bar{G}$ are the longitudinal and axisymmetric shear modulus for the linear regime. The expressions for these moduli are:

$$\bar{G} = (1 - V_f)G_m + V_f G_f, \tag{2.18}$$

which is the stiffness of the fiber-dominated response; and

$$\tilde{G} = \frac{(1 - V_f)G_m + (1 + V_f)G_f}{(1 + V_f)G_m + (1 - V_f)G_f}, \tag{2.19}$$

which is equal to the Hashin-Strickman lower bound for the initial shear modulus of transversely isotropic materials with incompressible components. V_f is the fiber volume fraction, and G_f, G_m are the shear moduli of fibers and matrix respectively. Agoras et al. also gives an expression for the longitudinal stress on the onset of microbuckling [1]:

$$\sigma_{crit} = -\tilde{G}\left(\frac{\bar{G}}{\bar{G} - \tilde{G}}\right)^{2/3}. \tag{2.20}$$

These authors also considered the effect of the loading angle on the compressive instability:

$$\lambda_{crit}^3 cos^2(\alpha) - \lambda_{crit}(1 - \frac{\tilde{G}}{\bar{G}})^{2/3} + \sin^2(\alpha) = 0. \tag{2.21}$$

The influence of the angle on the critical stretch from Agoras et al. [1] can be observed in Figure 2.3

for composites of different moduli ratios $t = \bar{G}/\tilde{G}$. The plot represents the dependence of the critical stretch with the angle described by Equation (2.21).

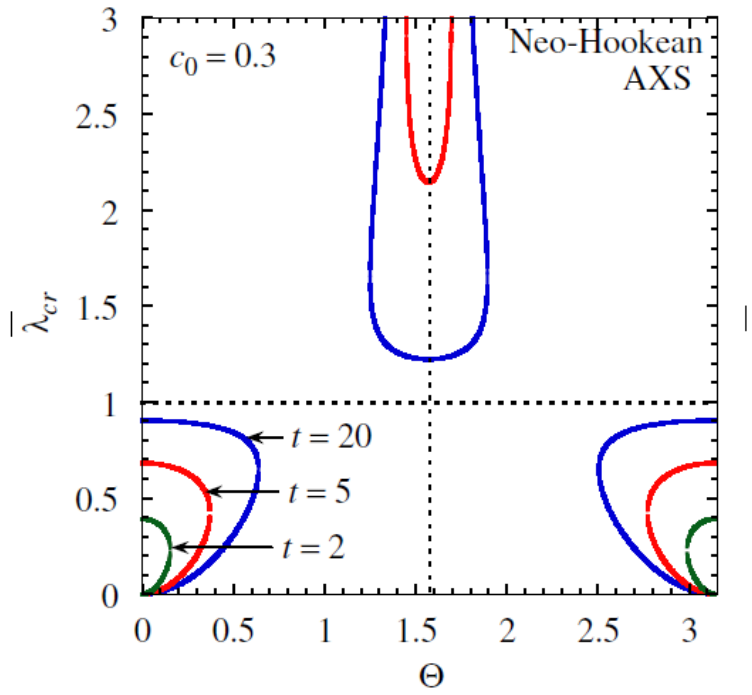

Figure 2.3: Influence of the loading angle on the macroscopic critical stretch, taken from Agoras et al. [1]. The angle Θ is given in radians. The parameter t indicates the shear stiffness ratio, $t = \tilde{G}/\bar{G}$.

This effect can be seen in the lower left part of the plot in Figure 2.3. For each material, there is a maximum angle for which there exists instability in compression. The stretch at the onset of the instability at 0^o is closer to 1 for increasing ratios of shear moduli, t. This means that highly anisotropic materials are also highly unstable. This effect will be seen in the material studied in this thesis. The other important conclusion that can be reached from Figure 2.3 is that, for small angles Θ, when $\Theta = 0$ is the fiber direction, the compressive strength increases as the stretch for the onset of instability decreases.

2.2.2 Microscopic instabilities

To study the stability of the periodic microstructure, the length of the buckling waves needs to be taken into account. However, Rosen's model predicts failure for wavelengths $\lambda \gg 1$ that minimize the strength in compression. This implies that the material will buckle with a semiwavelength as

long as the specimen size, which was confirmed by Jelf and Fleck [27].

Experiments have shown that microbuckling occurs at a wavelength smaller than the specimen size. Francis et al. found wavelengths of 1 to 3 mm for elastic memory composites under bending, with a linear correlation with the thickness of the composite [21]. Campbell et al. proposed an alternative solution for compressive microbuckling with a model that combined the shear energy with Timoshenko's elastic foundation energy, assuming a sinusoidal fiber buckling shape [9]. They found that the critical wavelength of a unidirectional composite with a square fiber arrangement is

$$\lambda_{crit} = \frac{\pi d_f}{4}\sqrt{\frac{E_f V_f}{G_m(1-V_f)}}, \tag{2.22}$$

where d_f is the fiber diameter. λ_{crit} is the length at which a pin-jointed beam buckles at σ_{crit}, and is equivalent to a half wave of the fibers' sinusoidal shape. With this model, the critical stress becomes

$$\sigma_{crit} = \frac{2G_m(1-V_f)}{V_f}, \tag{2.23}$$

which is equal to Rosen's strength for a fiber volume fraction, $V_f = 0.5$.

The discrepancies of the observed microbuckling wavelength with respect to the predicted ones are due to the strong influence of fiber misalignment, initial waviness, presence of free edges, fiber-matrix interaction, or stress concentrations [4, 66]. Experimental work by Waas and Babcock using optical microscopy with real-time holographic interferometry found that the failure in compression originated at a traction-free edge. The effect of free-traction surfaces appears to be stronger in stiffer composites [66].

Robbins developed finite element techniques to study microbuckling of a representative volume element (RVE), representing two fibers in a hexagonal packing through the application of periodic boundary conditions [54]. The model introduced a geometric nonlinearity through the application of a shear force that was released after applying compression, hence inducing the RVE to buckle, with the length of the RVE representing a half wavelength. A parametric study was done to understand the influence of the wavelength on the critical buckling, as can be seen in Figure 2.4.

Some of the models mentioned here will be used in the next chapter to predict the critical stress in compression of the carbon fiber-reinforced silicone composite studied in this thesis. The following chapters attempt to predict the onset of macroscopic instabilities using a linear homogenization

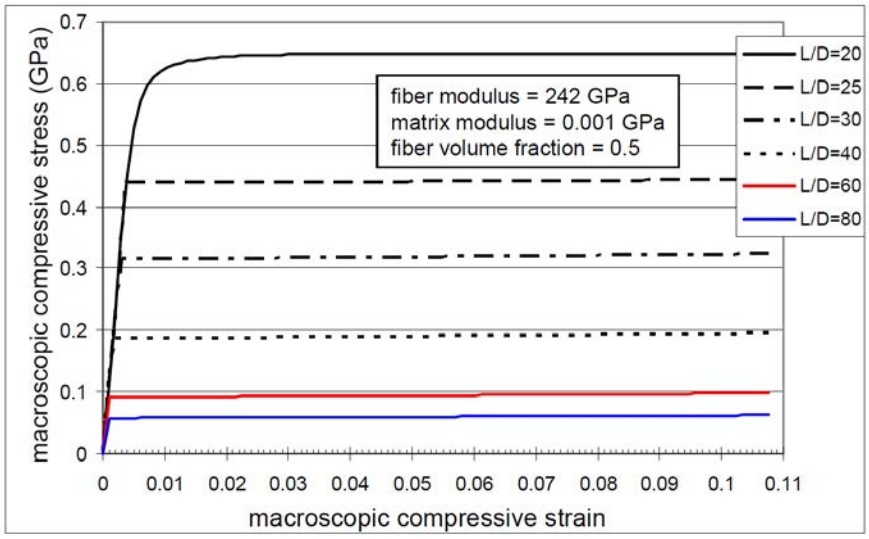

Figure 2.4: Influence of the RVE length (or microbuckling semiwavelength) on the critical buckling stress. L/D is the ratio between the length of the RVE and the fiber radius. Matrix and fiber modulus are very similar to the materials studied in this thesis. Taken from Robbins [54].

model, and the onset of microscopic instabilities with a non-linear simulation of an RVE representing the buckle wavelength, in a similar approach to Robbins [54].

Chapter 3

Experimental characterization of unidirectional CFRS

This chapter describes the experimental work done on a unidirectional carbon fiber-reinforced silicone (CFRS) composite material manufactured by L'Garde, Inc. Experimental work in this type of materials is still scarce [20, 21, 49, 38]. An extensive characterization of the bending behavior of a similar material was recently performed by López Jiménez [31].

The main focus of this work is to find the onset of failure in compression of high-strain composite rods. To that end, the microstructure of the rods has been studied to characterize the fiber volume fraction and the fiber misalignment distributions on the samples. Additional experiments in tension, bending and torsion are discussed in this chapter in order to obtain a further understanding of the behavior of this material.

3.1 L'Garde unidirectional CFRS material

The L'Garde unidirectional CFRS material consists of unidirectional carbon fibers embedded in a silicone matrix. L'Garde provided samples with different geometries that were tested to measure the mechanical properties of the material. This section contains a brief description of the constituents and the geometry of the most relevant samples tested.

3.1.1 Matrix

The matrix used by L'Garde to manufacture the composite is an optically clear silicone. The properties provided by the manufacturer are summarized in Table 3.1.

Density	1.09 g/cm^3
Hardness (shore A)	33
Tensile strength	5 MPa
Elongation at break	450 %

Table 3.1: Silicone matrix properties.

Mix and Giacomin derived equations for all durometry scales standarized by ASTM D2240 [43]. In particular, the Shore A scale uses a 35^o truncated cone to perform the indentation on the rubber. The equation that relates the non-dimensional Young's modulus, E, to the hardness S is:

$$\Upsilon = \frac{1 + M_i \mathscr{H}}{(1 - \mathscr{H})^2}, \tag{3.1}$$

where $\mathscr{H}$ is the scaled hardness, $\mathscr{H} = \sigma S/p_0$. σ is the spring sensitivity, M_i the mechanical indentability and p_0 the initial indentor protrusion. The Young's modulus is

$$E = \frac{\Upsilon F_0(1 - \nu^2)}{2rp_0}, \tag{3.2}$$

where r is the indenter radius. The Poisson's ratio of a hyperelastic rubber is $\nu \approx 0.5$. Using the values provided in [43] corresponding to the scale Shore A, the Young's modulus of the matrix is determined:

$$E_m \approx 1.71 \text{ MPa}. \tag{3.3}$$

L'Garde prepared sheets of pure silicone that were cut into bone-shaped samples and tested in tension by López Jiménez (see Figure 3.1). The test showed a perfectly hyperelastic behavior in the matrix, and the Young's modulus can be assumed to be linear for a stretch $\lambda < 1.2$, or a strain $\epsilon < 0.2$. The stiffness in compression of pure silicone was not measured, and it was assumed to be equal to the stiffness in tension for small strains.

The matrix modulus averaged for low strains was found to be

$$E_m \approx 1 \text{ MPa}, \tag{3.4}$$

which is in agreement with Peel's measurements for the same silicone matrix [49].

Additionally, the matrix behavior was fitted to a hyperelastic Gent model with a potential given

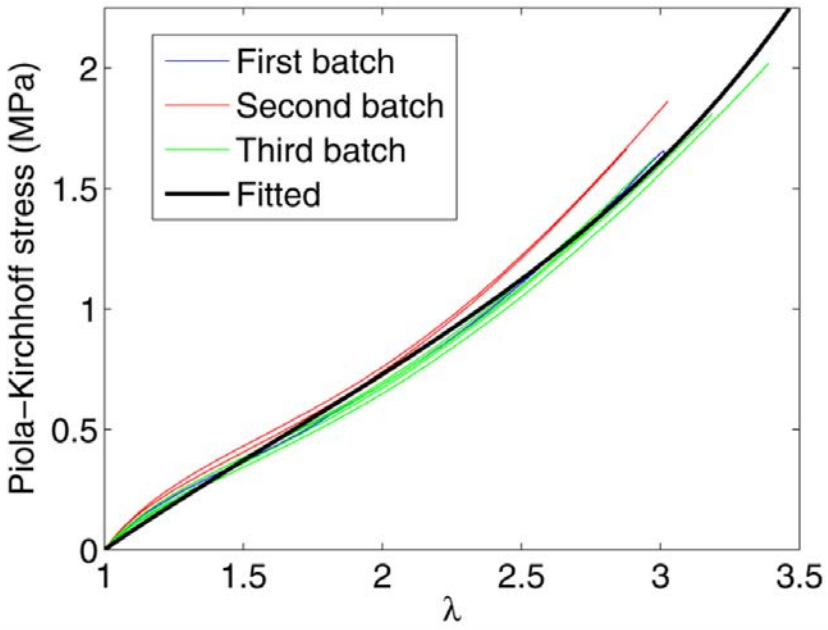

Figure 3.1: Tension tests on silicone samples.

by [23]:

$$W = -C_1 J_m \ln\left(1 - \frac{J_1}{J_m}\right) + C_2 \ln\left(\frac{J_2 + 3}{3}\right), \tag{3.5}$$

where

$$J_1 = \lambda_1^2 + \lambda_2^2 + \lambda_3^2 - 3, \tag{3.6}$$

$$J_2 = \lambda_1^{-2} + \lambda_2^{-2} + \lambda_3^{-2} - 3, \tag{3.7}$$

and $C_1 = 0.2208$ mJ, $C_2 = -0.2591$ mJ and $J_m = 26.8461$ from the fitted data.

3.1.2 Fibers

The fibers used to manufacture the CFRS material are HexTow® AS4 carbon fibers, which are continuous, high-strength, high-strain, PAN based fibers [26]. 12K tows (12000 filaments) have been used to fill the silicone rubber on every sample.

The material properties provided by the manufacturer are summarized in Table 3.2.

Density	1.79 g/cm^3
Tensile modulus	231 GPa
Tensile strength	2.2 GPa
Ultimate elongation at failure	1.7 %
Fiber diameter	7.1 μm
Carbon content	94 %

Table 3.2: 12K AS4 fiber properties.

3.1.3 Composite samples

Four types of experiments were performed in unidirectional CFRS samples. Tension and bending experiments were performed on flat samples, while rod samples were tested in compression and torsion. Tables 3.3 and 3.4 detail the dimensions of each type of specimen.

Test	Tension and bending
Length, l_f	300 and 150 mm
Width, w	12 and 25 mm
Thickness, t	0.75 and 1.5 mm

Table 3.3: Dimension of the flat samples.

Test	Compression and torsion
Length, l_r	50 mm
Diameter, d	6.05 mm

Table 3.4: Dimension of the rod samples.

The fibers were parallel to the length direction in all samples except the ones used for transverse tension, see Figure 3.2. The Z axis was taken parallel to the fibers, and the plane X-Y transverse to them.

The flat samples were provided by L'Garde with the dimensions in Table 3.3. However, the rod samples were manufactured with a length of 300 mm and were cut with a razor in planes perpendicular to the fibers and the axis of the rod to obtain the desired geometry.

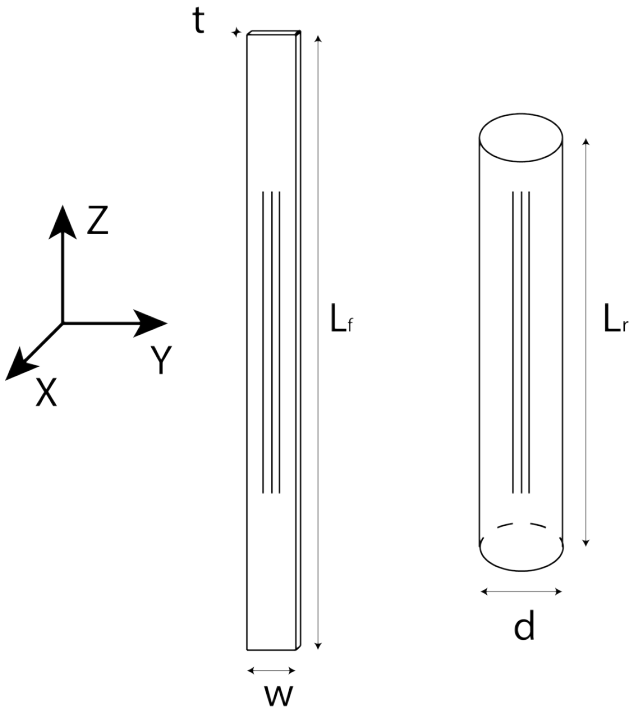

Figure 3.2: Schematics of the samples and reference coordinates. The Z axis is parallel to the fiber direction.

3.2 Characterization of the microstructure

To understand the behavior of the material and to be able to produce estimates of its mechanical properties, the microstructure of the composite had to be studied. This was done in two ways: through micrographs of perpendicular cuts to the fiber direction, to observe the fiber volume fraction; and through micrographs of cuts parallel to the fibers, to study the fiber angles respect to the nominal fiber direction. Rod samples were used to perform the study of the microstructure.

3.2.1 Fiber volume fraction

In order to study the fiber volume fraction of the composite in detail, it is necessary to obtain pictures of sections perpendicular to the fibers with a microscope. Calling A the area of the analyzed section and A_f the area of all the fibers within the section, the fiber volume fraction is

$$V_f = \frac{A_f}{A}. \tag{3.8}$$

For common composites, with non-compliant matrices, the usual approach is to pot the composite in epoxy resin and to polish the surface to obtain a perfectly flat surface perpendicular to the fibers. However, the high compliance of the silicone did not allow for this method. For this reason, sections were obtained by cutting the samples with a box cutter or a razor blade.

The method of obtaining micrographs on the rod samples was as follows. A series of cuts were made along the length of the rod to divide the rod in sections. The resulting sections were held under the microscope, and micrographs were taken in random places of the cross-section of the rod.

The sections were observed with a Nikon Eclipse LV100 with 20x and 50x objective magnification, and bright-field pictures were taken with a Nikon DS-Fi2 digital camera. Focusing on the entire image was not possible: the cut section was not flat enough; hence parts of it were outside the depth of field of the camera. To solve this issue, the extended depth of focus (EDF) module in the software NIS-Elements was used [46]. The EDF module takes pictures of the sample under different depth of focus, and constructs a stacked image where all regions are focused.

Fiber volume fractions were measured by counting the number of fibers inside cross-sectional areas of 200 μm x 100 μm. The fibers were counted visually with the help of a MATLAB code to mark and store the counted fibers. The number of fibers was multiplied by the area of a single fiber with diameter = 7.1 μm and divided by the total area. Volume fractions from the different regions were stored to obtain statistical data from all the observed regions.

The measured values presented a high spread over the cross-section of the rods. Particularly, the volume fractions were smaller in the regions close to the surface of the rod, while the fibers clustered more near the center of the rod (see Figures 3.3 and 3.4). Between the regions of high concentration of fibers in the center of the rod, large zones with silicone matrix were found as well. These regions probably were the space between two or more fiber tows (see Figure 3.5).

The average values and error (represented with the standard deviation of the measured volume fractions) are shown in Table 3.5. Averages for the center of the rod and an annular region of ~ 1 mm near the surface are also included.

Due to the high spread encountered, the fiber volume fraction was estimated in a more reliable way, using the mass and volume of the samples, along with the density values of the constituents provided by the manufacturer. The equation that relates composite, constituent densities and fiber

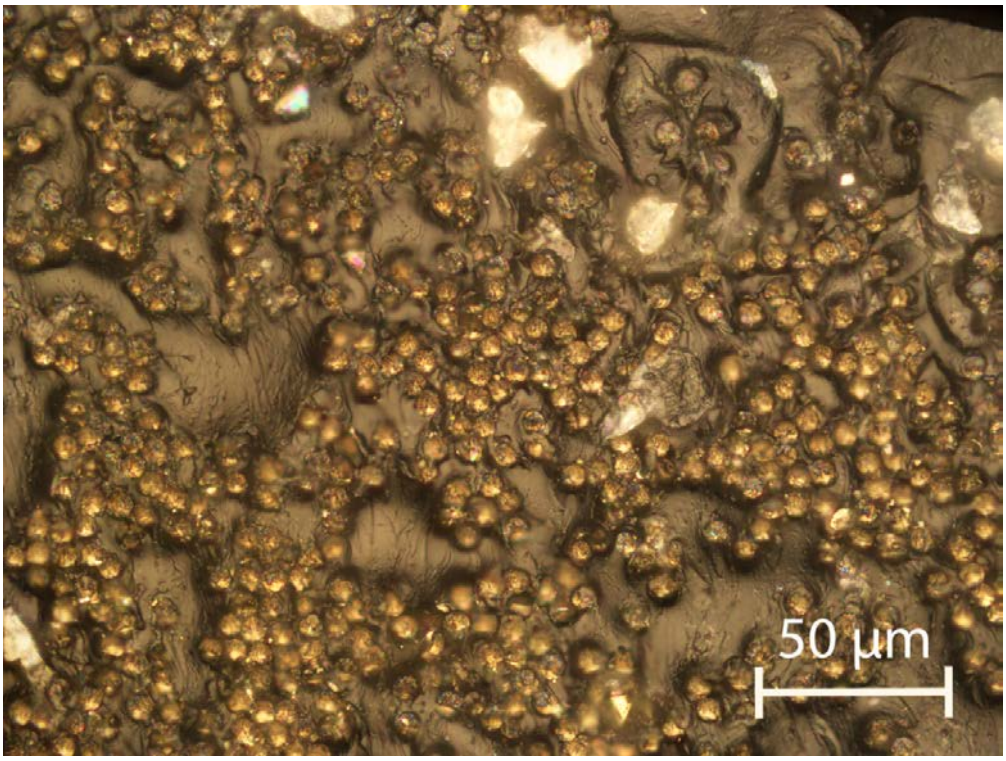

Figure 3.3: Micrograph of the cross-section near the surface of the rod, with $V_f \sim 20\%$.

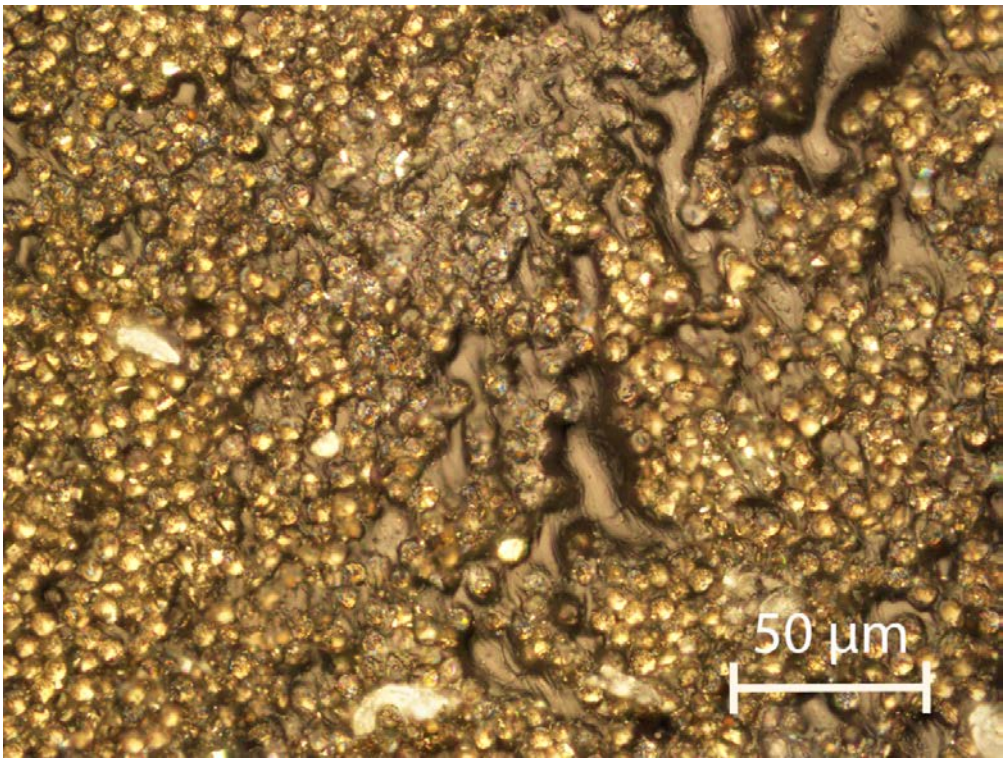

Figure 3.4: Micrograph of the cross-section at the center of the rod, with $V_f \sim 42\%$.

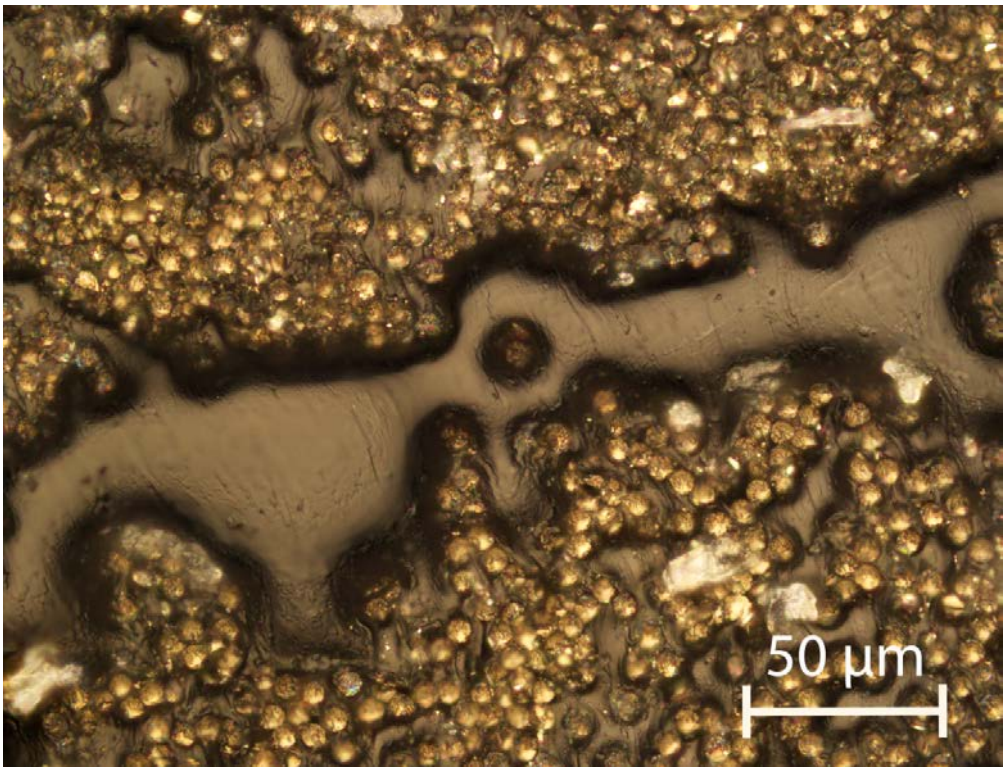

Figure 3.5: Zone with a large concentration of pure silicone.

Region	Average $V_f(\%)$	Standard deviation (%)
All	38.7	13.4
Center	45.9	5.7
Surface	21.9	4.4

Table 3.5: Fiber volume fraction and standard deviation near the center, near the surface and through all the measured regions.

volume fraction is

$$\rho = V_f \rho_f + (1 - V_m)\rho_m. \tag{3.9}$$

The fiber volume fraction was estimated $V_f = 40\%$, with an uncertainty of $\pm 0.4\%$, calculated from the error propagation of mass and geometry measurements.

3.2.2 Fiber angles

Analogously to measuring the fiber volume fraction, the distribution of fiber angles respect to the nominal fiber direction, i.e., the rod axis, was studied. The fiber angles were measured on 500 x 500 μm bright-field micrographs of plane cuts of the rods parallel to the fiber direction. As in the fiber volume fraction micrographs, the cuts were done with a blade. The micrographs were obtained with a Nikon Eclipse LV100 digital microscope with the same effective depth-of-focus method described previously.

The fiber angles were measured manually through a MATLAB code that stores the position of any point clicked on the image using the *guinput* command. With the coordinates of two points of a fiber, the angle of that fiber with respect to the image reference can be calculated. This reference was taken initially parallel to the axis of the angle, with an error of $\sim 0.1^o$. The points taken on each fiber were at a distance of ~ 1 mm. The error in the measured fiber angles is $\sim 0.1^o$ as well, and it is due to the pixel resolution of the graphical input in MATLAB.

Figure 3.6 is an example of the micrographs used for this characterization. A total of 500 fibers were measured with this method, taken from 20 different longitudinal cuts of the composite rods.

A different method to measure the fiber angle was attempted with the Hough transform [37]. To detect the fibers, the micrographs were converted into black-and-white images in MATLAB and the functions *hough*, *houghpeaks* and *houghlines* were used to extract the line angles. Different thresholds had to be adjusted to obtain a clear black-and-white image and as many lines detected as possible within one micrograph.

This method is fast and efficient; however, many of the fibers that were easily detectable to the human eye were either erased in the process of converting the image to binary or not detected by the Hough algorithm (see Figure 3.7). The error of the method has been estimated to be the radius of a fiber divided by the length of the fibers in the measured section, i.e., 1 mm. This gives an error of $\sim 0.2^o$.

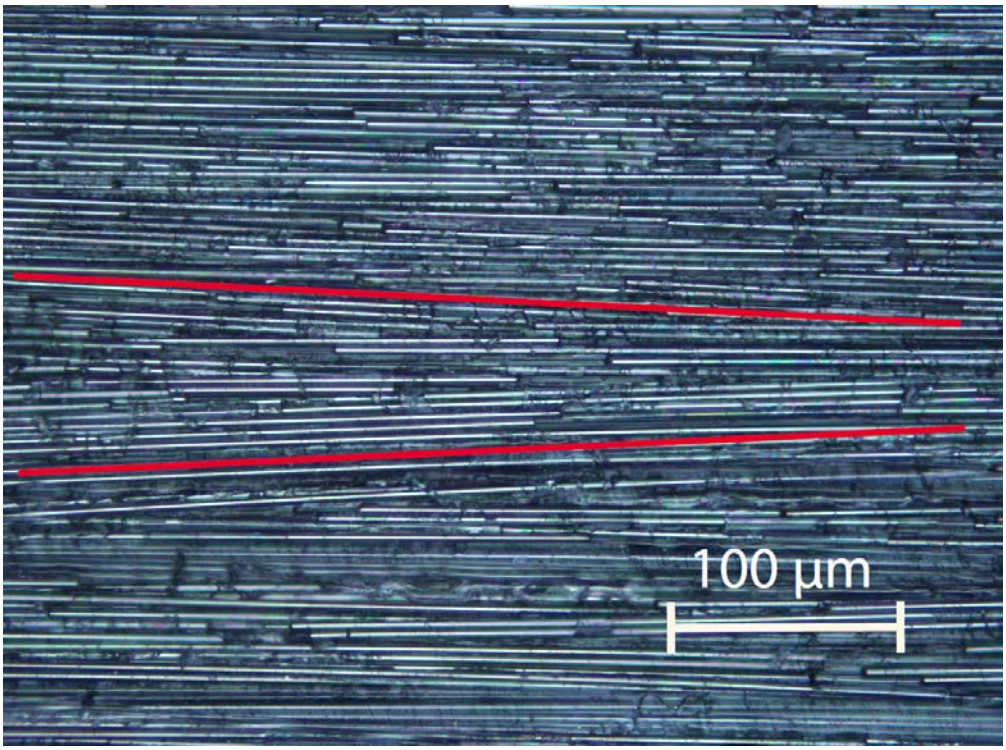

Figure 3.6: Micrograph of a section along the fibers. The red lines show the relative angle between two groups of fibers.

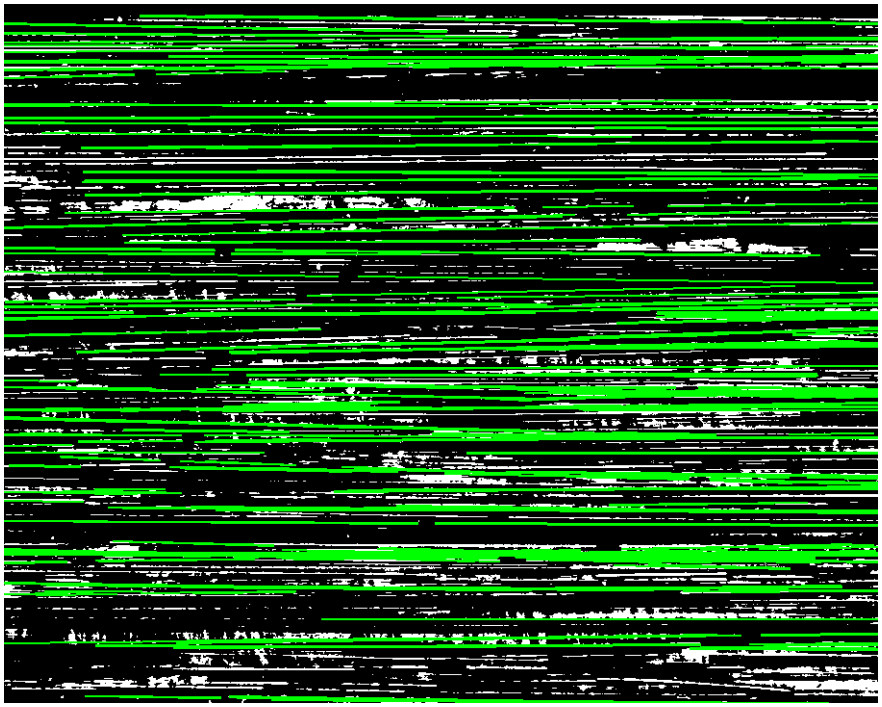

Figure 3.7: In green, lines detected by the Hough transform on a black-and-white image of the fibers.

A total of 4500 fiber angles from 20 different sections were obtained with this method. The data obtained has been approximated to a normal distribution. The histograms showing the normal approximation for both methods can be seen in Figure 3.8. The results are compared in Table 3.6.

Method	Visual	Hough transform
Average angle (^{o})	0.23	0.49
Region of minimum angle (^{o})	0.13	0.1
Standard deviation (^{o})	0.92	1.4
Region of minimum standard deviation (^{o})	0.3	0.49

Table 3.6: Comparison between average and standard deviation of fiber angle respect to the nominal direction for the total number of regions analyzed, and values for the region of minimum angle and minimum standard deviation.

The minimum angle measured for both methods was within the error of the measurements. The total standard deviation and the minimum standard deviation of misalignment obtained with the visual method are taken into account in Chapter 5, in order to study the influence of the fiber angle on the strength in compression of the rods.

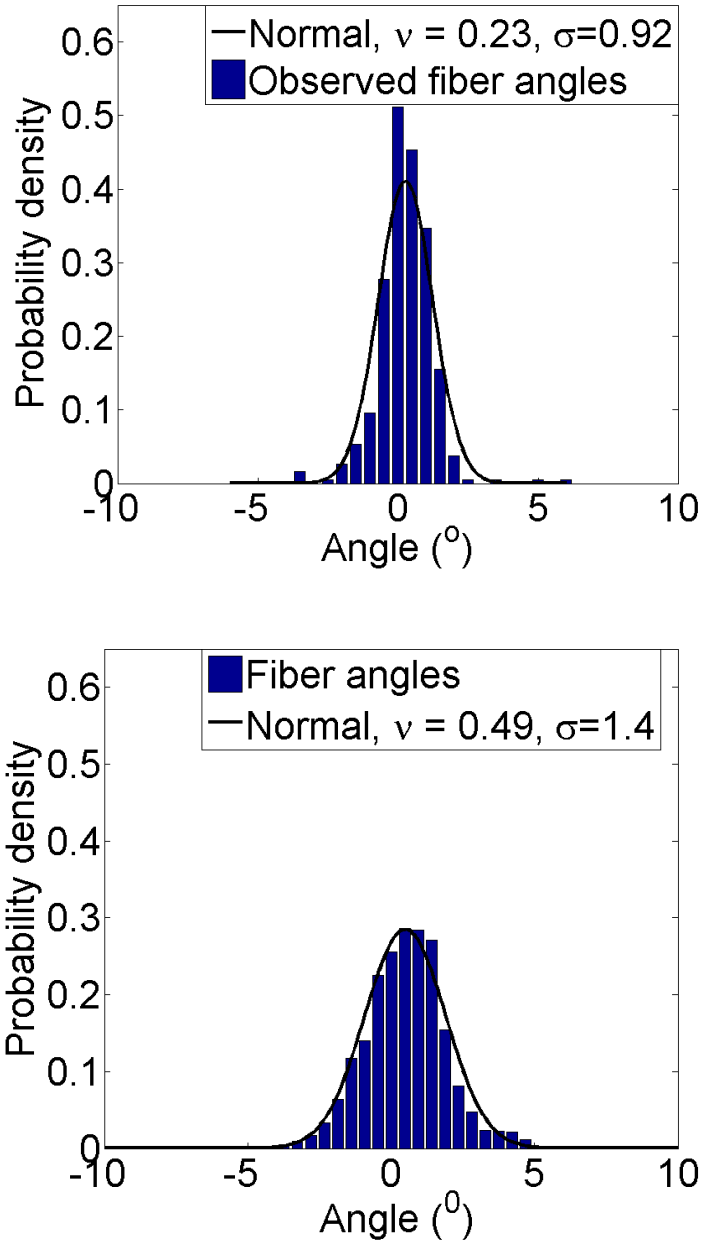

Figure 3.8: Histograms of the fiber angles measured with the visual and the Hough transform methods.

3.3 Tension experiments

These tests, based on ASTM D3039, used the samples described in Table 3.3. The samples were gripped between Wyoming tensile wedge grips with a saw pattern. Common composites are tested in tension with the help of glued fiberglass/epoxy or metallic tabs to protect the specimen. However, this is not possible for CFRS, due to the difficulty of bonding silicone to any other material. For this reason, emery cloth was wrapped around the clamped region of the sample to delay edge-slipping and the breaking of the fibers in the surface of the material due to the high compliance of the silicone matrix. Figure 3.9 shows the experiment set-up.

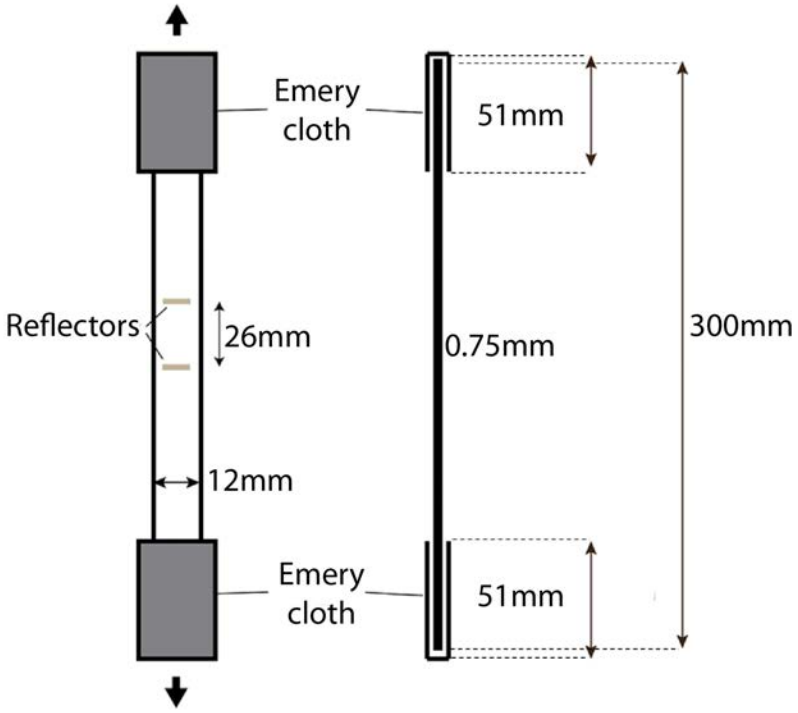

Figure 3.9: Schematic diagram of the tested sample.

The testing machine used was an Instron 5569 with a 50 kN load cell. The relative displacement between two reflecting strips was measured by an Epsilon LEO1 laser extensometer. The test consisted in five cycles on 3 nominally identical samples, up to a maximum strain of $0.2-0.3\%$ at a displacement rate of 1 mm/min. It was not possible to achieve higher strains due to edge slippage.

Figure 3.11 shows the stress-strain relationship obtained from a set of 5 load-unload cycles on 3 samples. The extensometer measurements were smoothed using a 500-point moving average. At

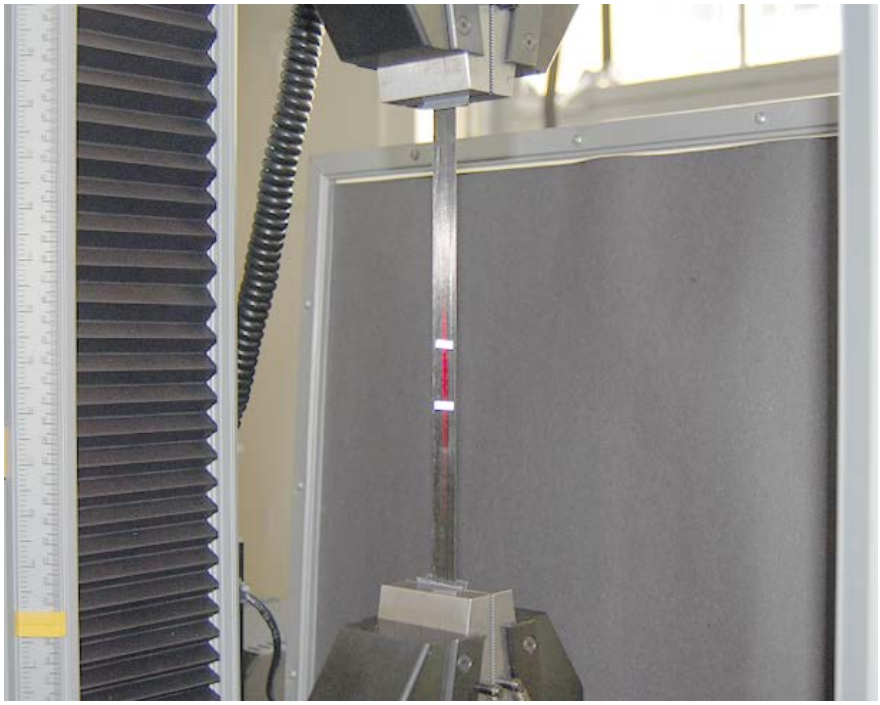

Figure 3.10: Sample tested in the Instron 5569.

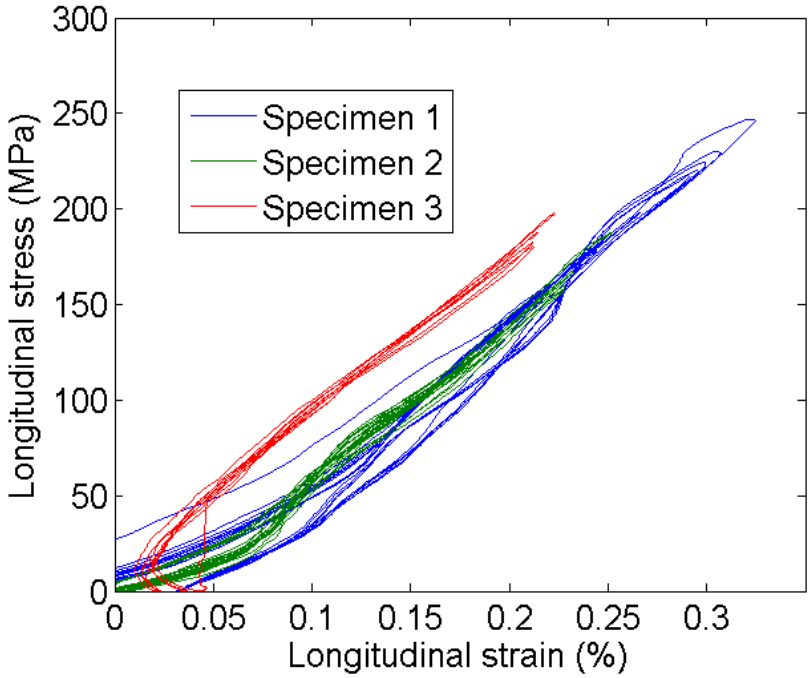

Figure 3.11: Tensile behavior at small strains. The initial non-linearity in the tests was attributed to initial slackness and twisting of the samples.

strains of less that 0.1% all samples showed some non-linearity, which was attributed to initial slackness and twisting of the sample, due to its low transverse stiffness. There was no change in the stiffness after any cycle. The modulus of each sample has been estimated by a least-squares linear fit for strains higher than 0.1%, assuming the linear relation:

$$E_z = \frac{\Delta\sigma_z}{\Delta\epsilon z}. \tag{3.10}$$

The resulting values are presented in the last section of this chapter.

3.4 Bending experiments

Four-point bending tests were carried out, based on the ASTM D6272 standard. The setup and geometry for these tests, on unidirectional flat samples as detailed in Table 3.3, are shown in Fig. 3.12. The span between the outer supports was 176 mm, and the distance between the inner load points was 50 mm. This relatively long span was chosen to minimize shearing near the points of application of the loads, by limiting the force that would need to be applied.

In a four-point bending test, the mid-span is only subjected to a uniform moment, and, due to symmetry, it can analyzed as a cantilever. The moment is

$$M = 2Fh, \tag{3.11}$$

and it can be related to the bending curvature κ through

$$\kappa = \frac{M}{E_z I} = \frac{2Fs}{EI}. \tag{3.12}$$

The tip deflection of the cantilever due to the applied moment is given by

$$\delta = \frac{Ms^2}{2E_z I}, \tag{3.13}$$

and hence we obtain the relation curvature - deflection:

$$\kappa = \frac{2\delta}{s^2}. \tag{3.14}$$

The deflection is the vertical distance between the center of the sample and the inner points where the load is applied, and it is measured with the laser extensometer. The load was measured with a 10-N load cell in the Instron 5569 testing machine. Figure 3.12 shows the experimental set-up. The upper part of the bending fixture had to be replaced with an aluminum block as the original fixture was too heavy for the 10-N load cell. The vertical force on the samples was applied on the contact points between block and samples. No kinking effects were observed due to this substitution.

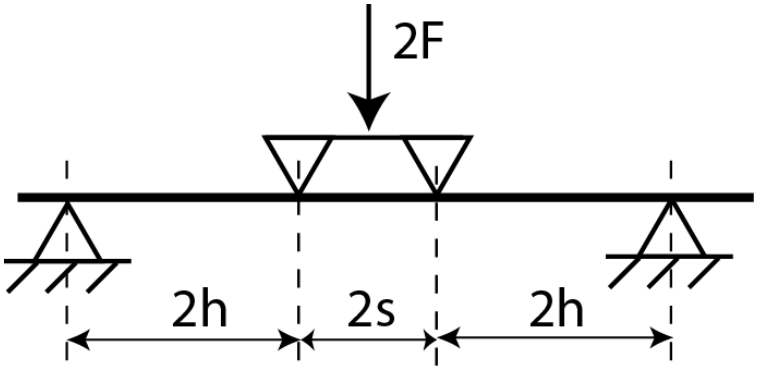

Figure 3.12: Schematics of the bending test. h=73 mm, s=25 mm.

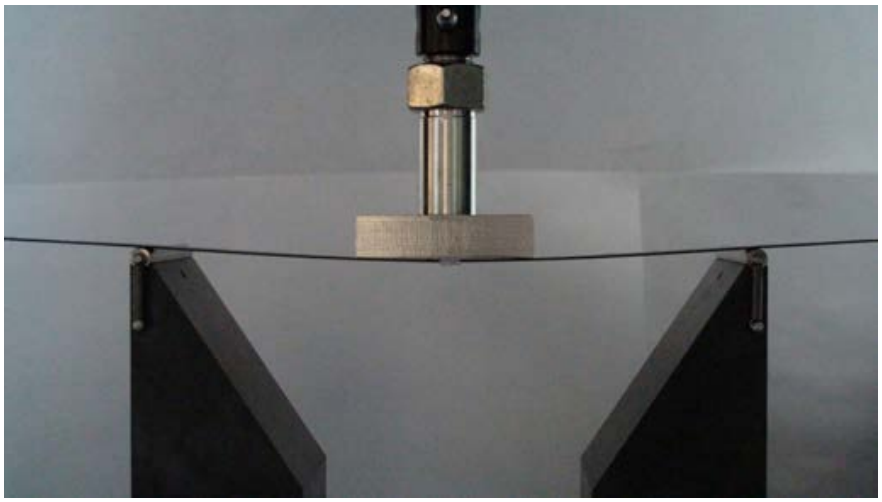

Figure 3.13: Bending test. The bending fixtures have been chosen and adjusted to achieve the maximum span possible to minimize the shearing force and avoid kinking.

Figure 3.14 shows the measured moment-curvature behavior of two test samples. The first load-unload cycle showed an initial linear response upon loading, reaching a plateau that was believed to be due to fiber microbuckling, followed by hysteretic behavior upon unloading. The behavior of both samples was softer during the second and third cycles, as already observed in previous tests by Lopez and Pellegrino [34]. The moment-curvature relation for the second sample had a negative slope for moments of less than 0.02 Nm, due to initial out-of-flatness of this sample.

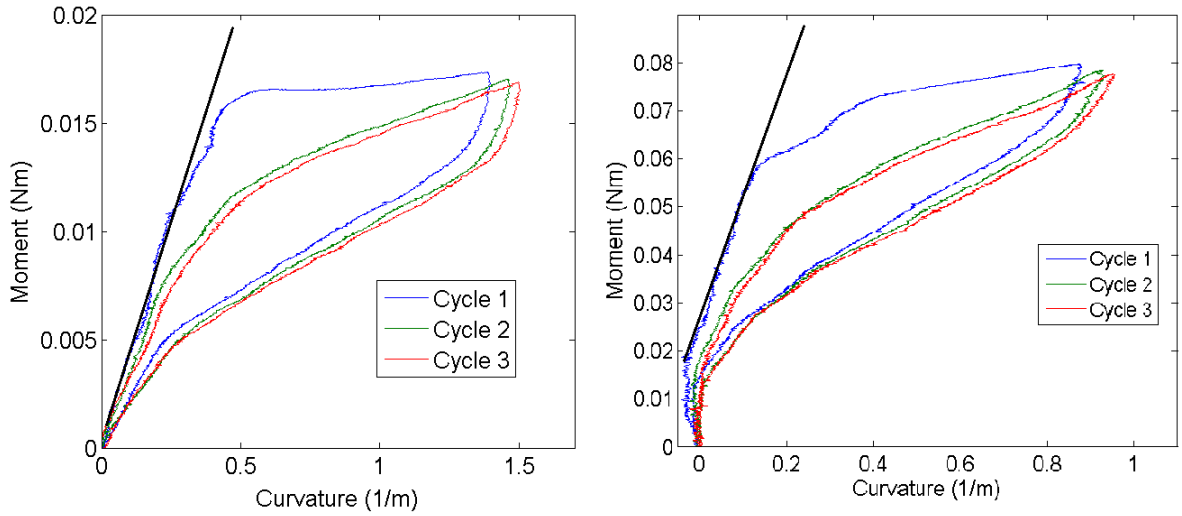

Figure 3.14: Moment-curvature plots for 3 load-unload cycles on samples with thickness of $t = 0.75$ mm and $t = 1.5$ mm. The straight lines define the bending stiffness during the first cycle, before fiber microbuckling.

The stiffness of these samples was obtained from the slope of the linear part of the loading curve. The bending stiffness is calculated from

$$E_z I = \frac{\Delta M}{\Delta \kappa}. \tag{3.15}$$

By dividing the measured bending stiffness by the second moment of area of the sample the modulus E_z can be obtained.

The softening that marks the end of the approximately linear part in the moment-curvature plots corresponds to the onset of fiber microbuckling in the regions of highest compressive stress. The critical moment at which this happens can be calculated from the fiber microbuckling stress

$\sigma_{z,crit}$:

$$M_{crit,th} = \frac{\sigma_{z,crit} I}{y_{max}}, \tag{3.16}$$

where $y_{max} = t/2$

The transition from elastic to buckled state is very well defined in the first cycle, but at later cycles the transition starts at earlier curvatures and is more progressive. This is due to the residual waviness that remains in the fibers after microbuckling. The same behavior was observed on other samples, with good repeatability in both stiffness and strength.

3.5 Compression experiments

Compression tests were performed to understand the mechanism that drives failure under pure compression of unidirectional elastomeric composites. However, testing the composite in compression was not an easy task. Its high compliance makes it difficult to find a compression fixture light enough that the composite will not collapse under its weight. Additionally, the alignment needs to be very precise, as any small misalignment can cause transverse loads on the sample and therefore undesired bending.

Compression tests based on ASTM D 6641 use combined loading compression (CLC) fixtures. A Wyoming CLC fixture was used for these experiments. The thin, flat samples could not be used, as they would have to be very short to avoid structural buckling. Furthermore, if a sample is clamped at its ends in a standard compression rig, the load is transmitted to the sample through shearing tractions on the end surface. This results in a non-uniform distribution of compression stress on the cross-section of the sample, due to the softness in shear of the material. This leads to obtain incorrect measurements of the compression stiffness and a very low critical load.

To tackle these issues, the rod samples were used for these tests (see Table 3.4). The rods are thick enough so that they do not buckle under the weight of the fixture. However, the fixtures are designed to hold flat samples. In order to make the samples compatible to the fixture geometry without damaging them, the tips of the rods were inserted inside square aluminum caps in which two holes had been drilled. The hole diameter was chosen so the rod would fit snugly inside the cap. Also, the distance from the holes to the walls of the aluminum caps was made equal to ensure a good alignment. The holes were filled with epoxy resin right before the rods were inserted to eliminate

the possibility of having any voids between the rod and the cap. This procedure was needed, as the tips of the rods need to be in complete contact with the caps to apply the end compression as uniformly as possible. Tolerances in the testing apparatus yielded a maximum misalignment of the rods with respect to the load direction of 0.1^o.

Figure 3.15 shows a schematic diagram of the sample geometry. A photo of a sample taken apart to show its pieces and a picture of the sample before being adjusted to the Wyoming CLC compression fixture can be seen in Figure 3.16.

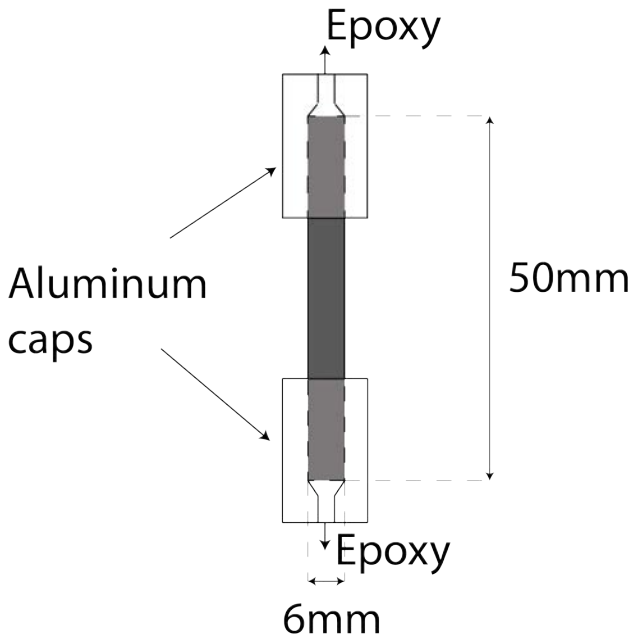

Figure 3.15: Compression test: schematic.

Once the sample had been mounted in the compression fixture, the fixture was placed between two compression platens in the Instron 5569 testing machine and tested in compression with a 1-kN load cell, at a displacement rate of 0.05 mm/s. Since the strain at which microbuckling occurs is small and a visualization of the failure mode was desired, a VIC-3D Digital Image Correlation System from Correlated Solutions [61] was chosen. Digital Image Correlation is an optical method used to measure deformation on an object surface. During deformation, a grey-value speckle pattern (Figure 3.17) divided in small neighborhoods called subsets is tracked. The 3D system is able to track a pattern on a three-dimensional surface, using two cameras and the required calibration.

To create the speckle pattern, the surface of the rod was covered in white paint. After the

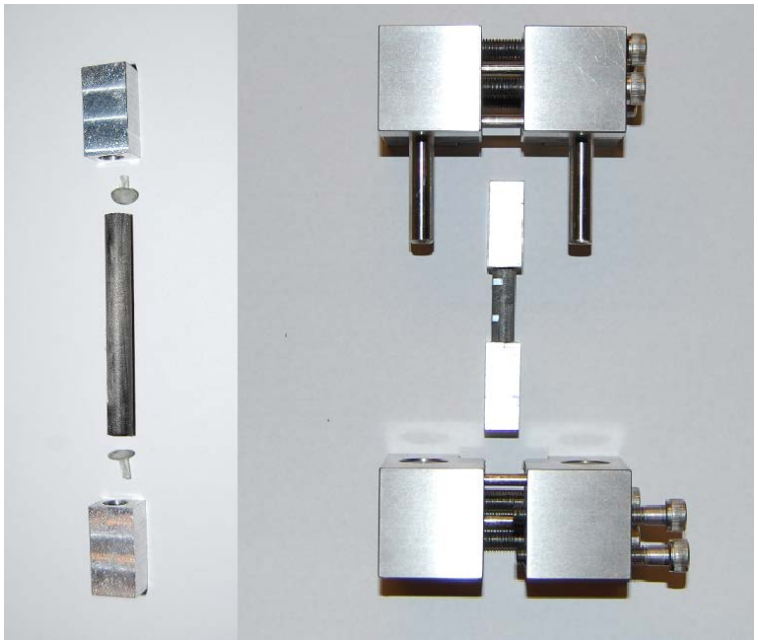

Figure 3.16: Pictures of the sample and the CLC fixture. The first photograph shows a sample after testing, with aluminum tabs and epoxy debonded purposely to describe the setup. The second photograph shows a sample bonded inside between the tabs, ready to be adjusted in the Wyoming CLC compression fixture.

paint was dry, a spray of black paint was used to create a random pattern with small black paint droplets. The speckles had to be small and dense enough to provide the required spatial resolution. The DIC system was able to track the full displacement field of the patterned surface. The error of the in-plane displacements measured by the DIC was 1/50000 the length of the field of view used. For a field of view of 20 mm, the error in local displacements was 0.4 μm.

During each compression test, images of the sample were recorded at a speed of 2 frames/second. Those frames were then analyzed with the DIC software VIC-3D, from Correlated Solutions, to obtain the three-dimensional displacements of the surface of the sample. Additionally, the load measured by the load cell was synchronized with the images.

The area of the sample that was imaged with DIC had a length of $\sim$ 20 mm and a frontal apparent width of $\sim$ 5 mm (Figure 3.17). The strain in the area of study was found by defining a 15-mm-long virtual extensometer in the longitudinal direction. It was found that averaging the longitudinal strain over the whole area of study would yield similar results. The estimated errors in the measurements are $\sim 2 \cdot 10^{-5}$ in strain and $\sim$ 0.1 MPa in stress.

The tests were made on several rods with the same volume fraction, $V_f = 40\%$. Figure 3.18

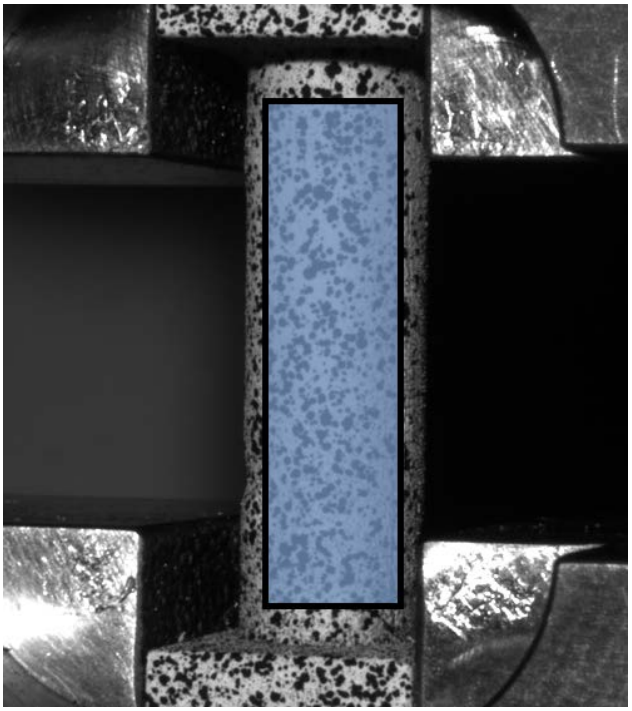

Figure 3.17: Sample inside the compression fixture. The area of study is highlighted in blue.

shows strain-stress plots for four of these rods. The longitudinal strain was measured with the 15-mm-long virtual extensometer defined on the surface of the rod, whereas the longitudinal stress is the load measured by the load cell divided by the cross-section of the rod.

The compressive stiffness has been calculated from the slope of the steepest part of the stress-strain curves. There is an initial load applied to the samples due to the weight of the compression fixture and to eliminate any slack in the system. The initial strain due to that preload is not shown in Figure 3.18. However, assuming that the initial regime is purely elastic, the resulting initial strain would be smaller than the error of the DIC strain measurements ($\sim 2 \cdot 10^{-5}$). The initial nonlinear behavior of some samples indicates that some slack was still present.

The onset of fiber microbuckling can be identified at the limit load of the measured stress-strain behavior. There is a large spread in the behavior of the samples shown in Figure 3.18, both in initial behavior and in failure stress. This large discrepancies are attributed to the presence of imperfections through the material, such as fiber angle distributions, waviness, or fiber volume fraction concentrations. Other imperfections such as macroscopic waviness or the presence of voids may also be the cause for this high spread. The behavior of rods 1 and 4 is similar to the behavior

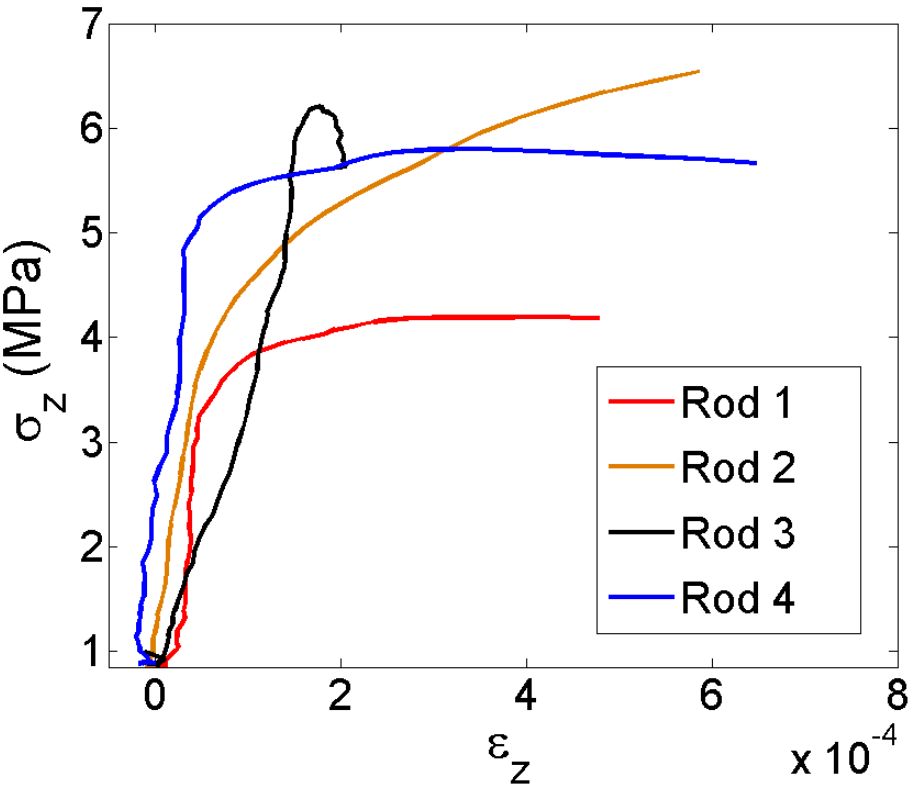

Figure 3.18: Compressive stress-strain curves for four different samples.

expected for microbuckling, and will be later used to validate the results from the finite element model presented in Chapter 5.

Figure 3.19 shows the local axial displacement components of the surface of two different samples under compression and after buckling occurs. Local strains at buckling are too small to be measured (of the order of the error of the DIC). However, displacements are a good way to observe the buckling mode of the rods. Both images (Rods 3 and 4) show different failure modes for two different samples, with a kink-like deformation for Rod 3 and a wavy mode of wavelength of ~ 1.8 mm for Rod 4. Other kinks were observed at the ends of the rods or the back surface, so they could not be captured by the DIC. These kinks were observed at a higher strain than the buckling strain. The microbuckling wavy modes could be identified by the DIC at longitudinal compression strains of $\epsilon_z \geq 10^{-3}$. A range of wavelengths from 1.5 to 2.3 mm were observed in these experiments.

The different wavelengths observed may be directly related with the difference in compression strength throughout the samples. However, these wavelengths are measured at a strain which is 10 times larger than the microbuckling strain, and it might be affected by post-microbuckling behavior and the presence of imperfections in the samples. Robbins studied the influence of the wavelength on the critical stress [54], predicting lower critical stressed for higher values of the microbuckling wavelength.

3.6 Torsion experiments

Torsion tests on the solid rods were designed to measure the longitudinal shear stiffness, G_{xz}, of the composite. According to the models reviewed in the previous section, the longitudinal shear stiffness of the composite dominates the strength in compression of unidirectional composites. Thus, a correct estimation of the shear stiffness was necessary to estimate the strength in compression.

The goal of the torsion test was to measure the torsional stiffness of the rod by applying a torque in the axial direction and measuring the torsion angle of the rod. To perform this test, the rod was fixed vertically with a wheel bonded to the top with epoxy. Two cables were glued and rolled on the wheel so that the ends of the cables came horizontally from opposite sides of the wheel and in opposite directions, so that a torque is applied (Figure 3.20). The cables had to be well aligned so that there is equilibrium of forces and the rod is not subject to any bending moments. Both cables pass through pulleys situated on opposite sides of the rod. As the same force had to be applied to

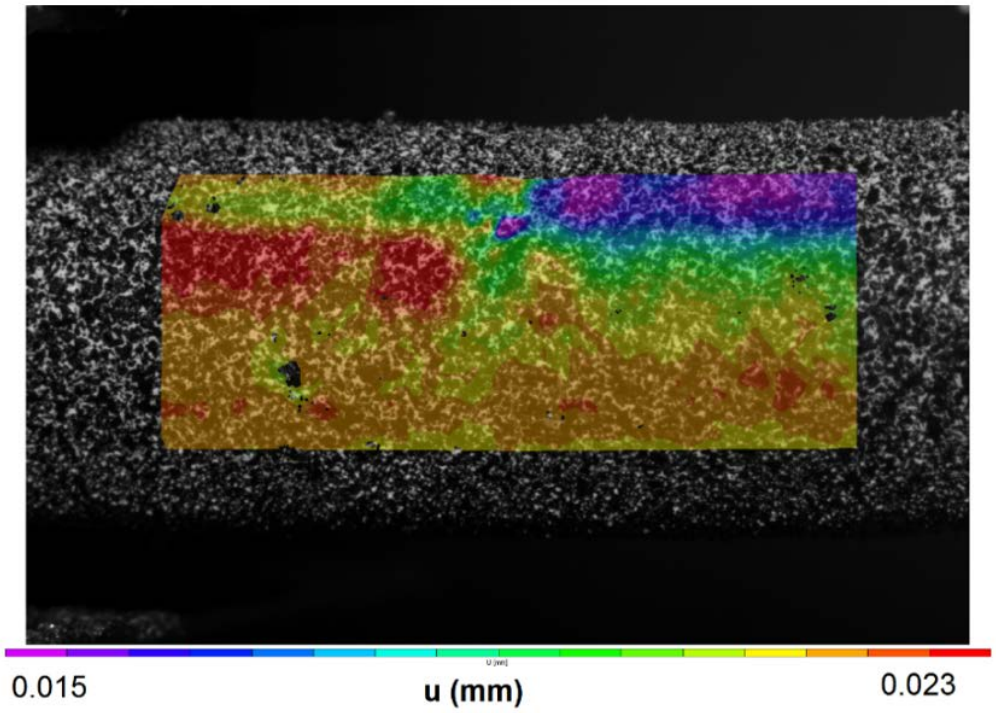

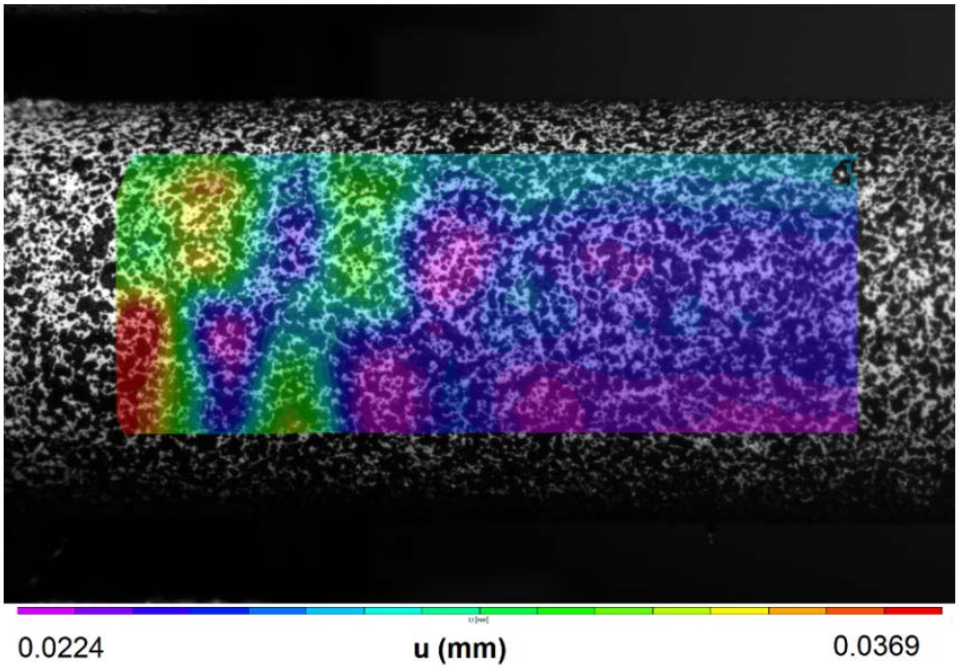

Figure 3.19: Axial components of the displacement on the surface of the rod after microbuckling. $V_f = 40\%$. The images correspond to rods 3 and 4. For Rod 4, the axial distance between regions of minimum displacement has been taken as the microbuckling wavelength.

generate a torque without bending, the same incremental weight was added to containers attached to the end of both cables. Weighed lead beads were used for this task.

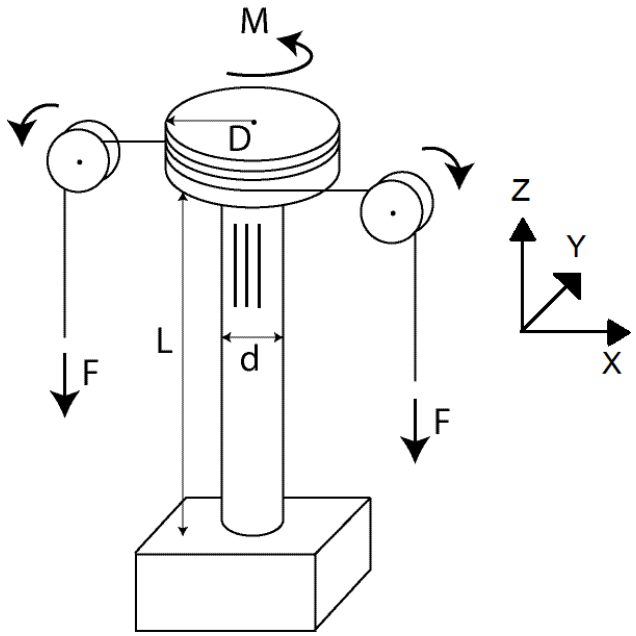

Figure 3.20: Schematic of the torsion tests on the unidirectional CFRS rods. The Z direction is parallel to the axis of the rod, coinciding with the nominal fiber direction.

The experiment was done quasi-statically in increments of 1 Nmm. A linear elastic behavior was observed, and it did not show any signs of failure. The measurements had very good repeatability, with errors of ~ 0.02 rad in angle and ~ 0.2 Nmm in torque. The longitudinal shear modulus was calculated from the torsional stiffness:

$$T = \frac{G_{xz} J \theta}{L_{rod}}. \tag{3.17}$$

L_{rod} is the length of the rod, and J is the second moment of area of the rod with respect to the longitudinal axis. Assuming the rods are transversely isotropic, $G_{xz} = G_{yz}$ is the shear component that affects torsional stiffness if the torque is applied in the direction of the fibers.

The longitudinal shear modulus measured with this test could depend of the end conditions of the test setup, and therefore be a structural rather than a material property. For this reason, tests were performed on rods of similar volume fraction but different lengths. The moment-curvature behavior is compared in Figure 3.21. The plots show good agreement between rods of different lengths for the small torsional strain regime, and it starts to differ for higher torsional strains. Therefore it can be concluded that the shear modulus measured is not affected by the end conditions

and possible warping for small strains. The plots represent the average over a series of 5 successive tests for each rod.

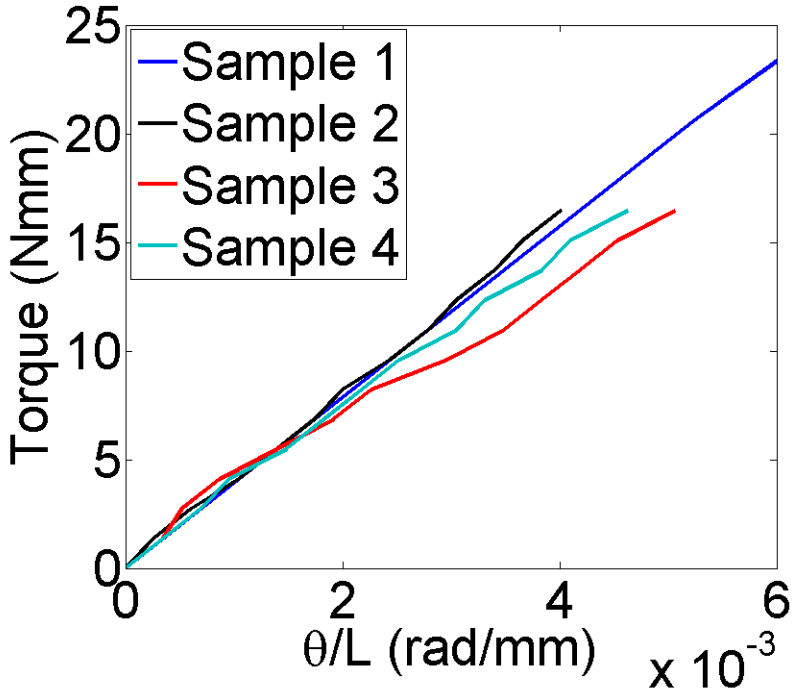

Figure 3.21: Torsion tests on four rods. The length of the rods is L = 100 mm for sample 1 and L = 50 mm for samples 2 to 4.

3.7 Summary of the results

In this section the measured stiffnesses and strengths are compared with the values that can be obtained from analytical models.

For a unidirectional composite, the longitudinal stiffness can be estimated by the rule of mixtures:

$$E_z = V_f E_{f1} + (1 - V_f) E_m. \tag{3.18}$$

Table 3.7 shows the average values of the longitudinal stiffness obtained from tension and bending tests on the thin samples, and compares them with the rule of mixtures (R.O.M.) estimate. The thin samples had a fiber volume fraction $V_f = 33\%$.

	Tension experiments	Bending experiments	R.O.M.
E_z (GPa)	71.6	80.3	78

Table 3.7: Comparison of experimental and estimated stiffness.

These results are in close agreement with the theoretical estimate, with a maximum measured error of 12% from the theoretical estimate. For the compression tests on the rods, the average $E_z = 90$ GPa, also close to the R.O.M. estimate for a volume fraction $V_f = 40\%$, which is $E_z = 93$ GPa. The measured longitudinal stiffness may be lower than the estimated one due to small misalignments, both in the fibers and in the testing fixture.

The theoretical strengths predicted by Timoshenko and Gere (Equation (2.3)) and Rosen (Equation (2.1)) have been used to estimate the strength in compression of the unidirectional CFRS rods. The solution suggested by Agoras et al. has also been calculated (Equation (2.20)). The solution for a fiber buckling on a elastic foundation in the presence of a free edge has been computed from Equations $23 - 26$ of Waas et al. [66].

The critical stress from Timoshenko and Gere's model has been calculated for a circular rod of radius $r = 3$ mm, $L = 50$ mm with clamped ends and an homogenized $G \sim G_m/(1 - V_f)$, with $V_f = 40\%$. The strain has been calculated by dividing the strength by the longitudinal homogenized modulus from the rule of mixtures.

For the model from Agoras et al., a Neo-Hookean isotropic model of the fibers and matrix is assumed. The approximate Young's modulus of the matrix is $E_m = 1$ MPa, and $E_f = 230$ GPa for the fibers. The shear stiffness of the fibers is $G_f \sim 88$ GPa assuming they are isotropic. The matrix is assumed incompressible, with a shear stiffness $G_m \sim 0.33$ MPa, and the volume fraction of the composite is $V_f = 40\%$. The compressive strain is $\epsilon_{crit} = 1 - \lambda_{crit}$. The Timoshenko and Gere, and the Agoras et al. models consider the macroscopic instability of the material, as the first is used for a homogeneous elastic rod and the second considers the homogenized strain energy of a material made of Neo-Hookean phases. The Rosen and the Waas et al. models take into account the microscopic buckling of the fibers. The first considers an infinite space of parallel fibers buckling out of phase, and the second represents the buckling on one fiber in a elastic foundation in the presence of a free edge. The assumptions differ greatly, but they give an idea of the order of magnitude of the critical strain and stress expected for this highly orthotropic material.

Model	ϵ_{crit}	$\sigma_{crit}(MPa)$
Timoshenko and Gere	$5.3 \cdot 10^{-6}$	0.50
Rosen (shear mode)	$5.9 \cdot 10^{-6}$	0.55
Waas et al.	$1.45 \cdot 10^{-4}$	13.3
Agoras et al	$7.33 \cdot 10^{-6}$	0.77
Experiments	$3.5 - 6 \cdot 10^{-}5$	$3.5 - 6$

Table 3.8: Estimated critical strain and stress for the onset of instability according to the different models, compared with the experimental strength in compression.

The predicted critical stress from the analytical models (0.5-0.77 MPa) for this material and geometry is much smaller than the observed critical stress (3.5-6 MPa). The possible causes of this difference were thought to be an incorrect estimation of the shear modulus of the matrix, and the presence of fiber misalignment in the composite. However, the torsion tests provided a shear stiffness of G_{xz} = 24 - 28 MPa. These values are much higher than the estimated composite shear stiffness $G_{13} \sim 0.55$ MPa. This was thought to be the effect of the fiber misalignment of the fibers as the effective shear stiffness increases with small values of the angle of misalignment.

Another interesting observation is that the critical moment observed in the bending experiments is about three times larger than for pure compression, which is the condition assumed in the estimation of σ_{crit}.

Chapter 4

Homogenization of the microstructure

Composite materials are heterogeneous media whose properties depend on the properties of the phases, the volume ratios and the geometry of the microstructure. Therefore, to study the macroscopic behavior of composites, the material needs to be replaced with a fictitious homogenized medium that is a good approximation of the original. This chapter focuses on the numerical estimation of the effective stiffness of the CFRS composite through finite element models. This effective stiffness will be used in Chapter 5 to perform finite element simulations of CFRS rods.

From the experiments of Chapter 3, the onset of failure in compression occurs at strains $\epsilon_{z,c} \sim 10^{-4}$ mm/mm. Additionally, the maximum transverse and shear strain observed in the simulations presented in Chapter 5 are of the order $\epsilon_x, \gamma_{xz} \sim 10^{-2}$ mm/mm. From Figure 3.1 we can assume that the matrix behaves as linear at strains $\epsilon_m \sim 0.1$ mm/mm. Hence, the techniques presented here assume small strains.

The goal is to obtain the effective stiffness matrix of the homogenized transversely isotropic composite material

$$\bar{\mathbf{C}} = \begin{bmatrix} c_{xx} & c_{xy} & c_{xz} & 0 & 0 & 0 \\ c_{xy} & c_{yy} & c_{yz} & 0 & 0 & 0 \\ c_{xz} & c_{yz} & c_{zz} & 0 & 0 & 0 \\ 0 & 0 & 0 & c_{yyzz} & 0 & 0 \\ 0 & 0 & 0 & 0 & c_{xxzz} & 0 \\ 0 & 0 & 0 & 0 & 0 & c_{xxyy} \end{bmatrix}, \tag{4.1}$$

which is written in Voigt notation. The coupling terms are assumed to be 0 due to orthotropicity.

$c_{xx} = c_{yy}, c_{xz} = c_{yz}, c_{yyzz} = c_{xxzz}$, as the material is transversely isotropic. Hooke's law relates the effective stress and effective strain of the homogenized material:

$$\bar{\sigma} = \bar{\mathbf{C}} \cdot \bar{\epsilon}, \tag{4.2}$$

where $\bar{\sigma} = (\bar{\sigma}_x, \bar{\sigma}_y, \bar{\sigma}_z, \bar{\tau}_{yz}, \bar{\tau}_{xz}, \bar{\tau}_{xy})$, and $\bar{\epsilon} = (\bar{\epsilon}_x, \bar{\epsilon}_y, \bar{\epsilon}_z, \bar{\gamma}_{yz}, \bar{\gamma}_{xz}, \bar{\gamma}_{xy})$ are the effective engineering stress and strain in Voigt notation.

The effective stress and strain can be found averaging the microscopic strain and stress tensor in a periodic Representative Volume Element (RVE) that represents the microstructure of the composite:

$$\bar{\sigma} = \frac{1}{V} \int_V \sigma(x, y, z) dV, \tag{4.3}$$

$$\bar{\epsilon} = \frac{1}{V} \int_V \epsilon(x, y, z) dV, \tag{4.4}$$

The total strain energy stored in a volume of the homogeneous medium is

$$U = \frac{1}{2} \bar{\sigma} : \bar{\epsilon} dV, \tag{4.5}$$

and the strain energy of the heterogeneous medium is

$$U' = \frac{1}{2} \int_V \sigma(x, y, z) : \epsilon(x, y, z) dV. \tag{4.6}$$

If periodic boundary conditions are ensured in the RVE, the Hill-Mandel condition can be assumed. This condition states that the strain energy of the homogeneous medium is equal to the strain energy of the heterogeneous medium:

$$U = U'. \tag{4.7}$$

Assuming perfect bonding between the matrix and fibers, the displacement is continuous at the interface. Hence, Gauss theorem can be used on Equation 4.4 to obtain [60]

$$\bar{\epsilon_{ij}} = \frac{1}{V} \int_S (u_i n_j + u_j n_i) dS, \tag{4.8}$$

which relates the macroscopic strains with the surface displacements of the heterogeneous RVE.

The set of periodic boundary conditions that needs to be imposed on the RVE can be obtained from Equation 4.8:

$$\begin{aligned}
u(L_x, y, z) - u(0, y, z) &= \bar{\epsilon}_x L_x \\
v(x, L_y, z) - v(x, 0, z) &= \bar{\epsilon}_y L_y \\
w(x, y, L_z) - w(x, y, 0) &= \bar{\epsilon}_z L_z \\
(v(x, y, L_z) - v(x, y, 0)) + (w(x, L_y, z) - w(x, 0, z)) &= \tfrac{1}{2}\bar{\gamma}_{yz}(L_y + L_z) \\
(u(x, y, L_z) - u(x, y, 0)) + (w(L_x, y, z) - w(0, y, z)) &= \tfrac{1}{2}\bar{\gamma}_{xz}(L_x + L_z) \\
(u(x, L_y, z) - u(x, 0, z)) + (v(L_x, y, z) - v(0, y, z)) &= \tfrac{1}{2}\bar{\gamma}_{xy}(L_y + L_x),
\end{aligned} \tag{4.9}$$

where L_x, L_y and L_z denote the dimensions of the RVE.

Two different techniques are presented here. The first assumes that the composite behaves linearly, i.e., the stiffness remains constant. The second one takes into account a microstructure that represents a fiber buckling in axial compression, and assumes that the stiffness depends on the compressive strain, $\bar{\mathbf{C}} = f(\bar{\epsilon}_z)$.

Although the microstructure characterization from Chapter 3 showed an irregular and random clustering of fibers in the CFRS rods, the microstructure is assumed to be a periodic square arrangement with the average fiber volume fraction V_f obtained in Chapter 3.

4.1 Linear homogenization (short RVE)

This method assumes that the stiffness $\bar{\mathbf{C}}$ is constant. The model assumes an unstressed short RVE with periodic boundary conditions. The homogenization can be performed by applying displacements to the boundaries while complying with the periodic conditions from Equation 4.9. As the material is transversely isotropic, only four load cases need to be analyzed in order to obtain every component of the stiffness matrix.

For example, an effective stress $\bar{\sigma}_x$ can be imposed in the direction X on the boundaries (L_x,y,z) and (0,y,z), while the rest of the components are zero. This effective stress can be applied imposing a relative displacement between the two boundaries, keeping the rest of the boundaries free, and ensuring the periodic boundary conditions from Equation 4.9. Solving the problem, the displacements at the free boundaries can be found, and hence the components of $\bar{\epsilon}$ using Equation 4.8.

Then, using the inverse of Hooke's law:

$$\bar{\epsilon} = \bar{\mathbf{S}} \cdot \bar{\sigma}, \tag{4.10}$$

where $\bar{\mathbf{S}}$ is the compliance matrix, $\bar{\mathbf{S}} = \bar{\mathbf{C}}^{-1}$. As $\bar{\epsilon}$ are known from the solution of the problem, and $\bar{\sigma_x}$ is the only non-zero component of the effective stress, the components of the compliance matrix are $\bar{s}_{xx} = \bar{\epsilon}_x/\bar{\sigma}_x$,$\bar{s}_{xy} = \bar{\epsilon}_y/\bar{\sigma}_x$,$\bar{s}_{xz} = \bar{\epsilon}_z/\bar{\sigma}_x$. This way, solving a longitudinal and transverse strain problem, as well as a longitudinal and transverse shear problem, the full compliance matrix can be obtained, and hence the full stiffness matrix.

4.1.1 Finite element model

The homogenization approach was used with the help of a 3D finite element model using the finite element package ABAQUS/Standard. The short RVE was modeled such that it represents one or more circular fibers surrounded by a matrix in a square arrangement. The RVE was a cube, with $L_x = L_y = L_z = L$. The side length was determined so that the fiber volume fraction was $V_f = \pi r_f^2/L^2$, where $r_f = 3.55\mu$m was the radius of the fibers.

The fibers were modeled as a linear elastic orthotropic material and implemented in ABAQUS with the *ELASTIC, TYPE = ENGINEERING CONSTANTS command. The fiber elements were C3D6 triangular prism.

The matrix was modeled as a hyperelastic incompressible material with Gent's potential (3.5) with $C_1 = 0.2208$ mJ, $C_2 = -0.2591$ mJ and $J_m = 26.8461$ from the fitted experimental data. The potential was implemented using the user subroutine UHYPER coded by López Jiménez [31]. The matrix elements were hybrid square brick elements. Hybrid elements need to be used when the material is modeled as incompressible. A linear material model was also used for the matrix to determine the effect of the hyperelastic model. However, the effect was small for small-strain simulations.

As the strains reached in the simulations were small, the fiber-matrix interface was modeled as perfect, with elements of each phase sharing common nodes. The fibers were aligned with the Z axis, and the X and Y axes were parallel to the principal directions of the square arrangement.

The periodic boundary conditions from Equation (4.9) were imposed to opposite boundaries of the RVE through the *EQUATION command. In order for the *EQUATION command to enforce the boundary conditions correctly, surfaces, edges and corners were grouped up as sets.

Additionally, nodes in opposite surfaces, edges or corners were defined in the same order. This implied that opposite, parallel faces had the same number of nodes and the nodes are at the same locations inside their respective planes. Meshing and selecting sets in ABAQUS/CAE did not guarantee this, and therefore the definition of the ABAQUS input file had to be customized with a MATLAB script. Small errors in the definition of the boundary conditions caused large errors in the prediction of the mechanical properties.

Once opposite sets of nodes were paired, the boundary conditions were applied to three dummy nodes. Imposing displacements on the dummy nodes was enough to define the six deformation cases needed to complete the definition of the stiffness matrix. The dummy nodes were associated with each pair of opposite nodes in opposite boundaries through the *EQUATION command. That ensured that displacement between the nodes was uniform, but allowed for relative displacement between the nodes within a boundary, ensuring periodicity. The displacements applied to the dummy nodes (DN) were such that a effective macroscopic strain was applied:

$$\begin{aligned} \bar{\epsilon}_x L &= U_{DN1} \\ \bar{\epsilon}_y L &= V_{DN2} \\ \bar{\epsilon}_z L &= W_{DN3} \\ \bar{\gamma}_{xy} L &= U_{DN2} + V_{DN1} \\ \bar{\gamma}_{xz} L &= U_{DN3} + W_{DN1} \\ \bar{\gamma}_{yz} L &= V_{DN3} + W_{DN2} \end{aligned} . \tag{4.11}$$

The boundary conditions were applied with nonlinear geometry activated, as one of the materials was modeled as hyperelastic. The average stress was calculated from the reaction forces at the active dummy node. The Poisson's ratio effects were extracted from the displacements of the other dummy nodes.

4.1.2 Model convergence

Simulations were performed on the model described previously with different levels of mesh refinement to ensure a correct prediction of the material stiffness. The effective transverse stiffness was used to analyze the effect of the mesh refinement, as it was observed to be the most sensitive component of the effective stiffness.

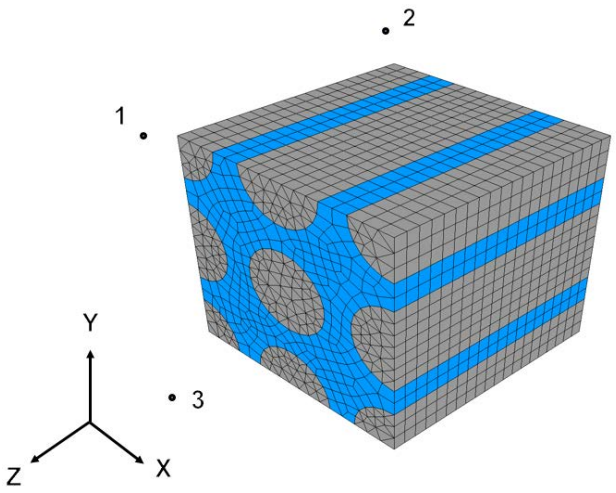

Figure 4.1: Representative Volume Element and dummy nodes associated to the boundaries. Dummy nodes 1, 2 and 3 associate opposite boundaries in the X, Y and Z direction, respectively.

Figure 4.2 shows the influence of the transverse stiffness with the mesh size. Four different sizes were studied, with element sizes of 1, 0.75, 0.5 and 0.25 μm. The number of elements for each size is indicated in the plot. It also compares the effect of pairing sets of boundary nodes with the *EQUATION command. The model converged worse when only the inner nodes in the boundaries were paired. Better results were achieved when edges and corners are paired to each other as well. The association of edges and corners to the dummy nodes depended on each effective stress case.

Initial simulations used a model that was composed of only one fiber surrounded by matrix, and by 4 fibers in a square arrangement. RVEs larger than 4 fibers did not obtain very different results to the 4-fiber solution, and therefore the effective stiffness used in Chapter 5 is based on this RVE.

In an attempt to model the effect of the free surface of the material a different RVE was considered, in which one of the boundaries (the free surface) was not subject to the periodic boundary conditions.

The result of this simulation is a reduction of the transverse stiffness to 60%, and no changes in the shear or the longitudinal stiffness. The stiffness resultant from this model is compared with the regular homogenization in the simulations of the cylindrical rod in Chapter 5.

This model is limited by the assumption of perfect fiber-matrix interface and the absence of random fiber arrangements like the ones observed in the microstructural characterization of the material. The effect of the random microstructure has been previously investigated by López

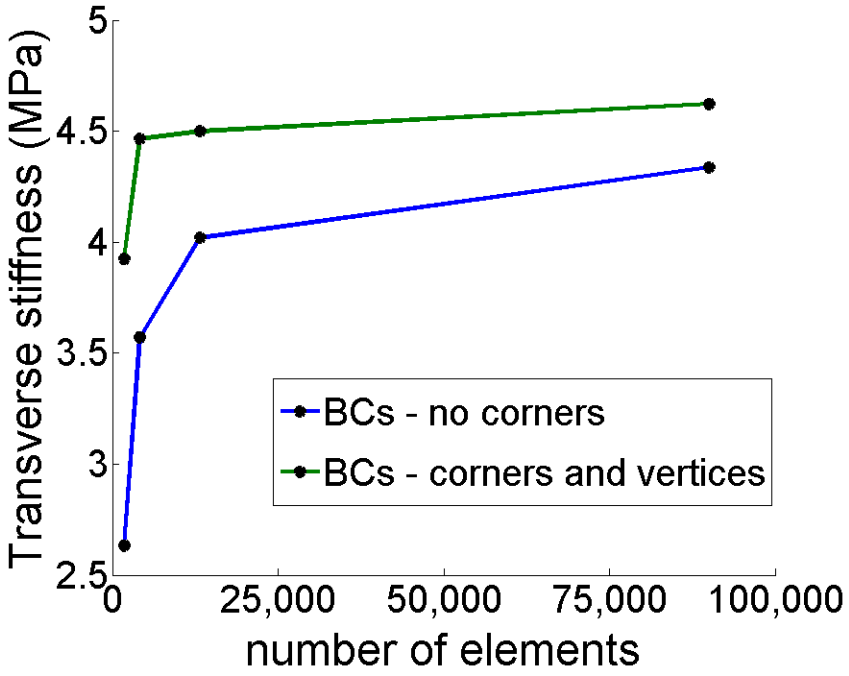

Figure 4.2: Convergence of the transverse stiffness with the number of elements.

Jiménez [31, 32].

4.2 Nonlinear homogenization (long RVE)

The linear homogenization described above predicts the effective stiffness of the microstructure. However, it does not carry any information related to the microbuckling of the fibers. The nonlinear homogenization described in this section assumes that the microstructure presents a wavy imperfection with a wavelength of the order of the microbuckling wavelength. The goal of the model is to obtain the tangent stiffness $\bar{\mathbf{C}}(\bar{\epsilon_z})$ at different values of longitudinal compressive strain $\bar{\epsilon_z} < 0$ of the RVE. We are, therefore, assuming an imperfect buckling path.

The RVE under consideration had a length in the fiber direction of the order of the wavelength λ. Due to the discrepancy on σ_{crit} between the model predictions and the experiments, the analytical models might not predict the correct wavelength. During the experiments on CFRS rods, a spread in wavelengths (1.5 to 2.3 mm) was observed. A length of 1 mm was assumed for a preliminary analysis. However, the effect of different lengths need to be studied. This effect was previously

investigated by Robbins on less than 1 mm wavelengths [54].

The model assumed small strains. For a material in a deformed state, conservation of strain energy was applied to obtain the tangent stiffness matrix due to small displacements from the deformed state:

$$\int \bar{\sigma}(\epsilon_z) : \delta\bar{\epsilon} + \int \delta\bar{\epsilon}^{\mathbf{T}}\mathbf{C}(\epsilon_z) : \delta\bar{\epsilon} dV = \sum P(\epsilon_z) \cdot \delta u + \sum \delta P \cdot \delta u. \tag{4.12}$$

To obtain the stiffness matrix, the nonlinear problem of the buckling microstructure was solved. Then, a periodic homogenization was performed with small perturbations around the deformed state to obtain the stiffness matrix for that deformed state according to Equation (4.12).

4.2.1 Finite element model

A 1-mm-long RVE with a one-fiber square cross-section was considered for this analysis. The material model, element size, and element type were the same as in the previous section. The mesh had a total of 40,000 elements. An imperfection proportional to the buckling eigenmodes or the RVE and with an amplitude 10% of the fiber diameter was added to the geometry. The mesh was customized so that opposite nodes in opposite boundaries were paired, as shown for the short RVE. Figure 4.3 shows the 1-mm RVE at the end of the compression analysis.

Figure 4.3: Representative Volume Element. The long RVE represents a sigle fiber surrounded by matrix, under imperfect buckling.

The RVE was deformed in compression to a total strain of $\epsilon = 4{\cdot}10^{-4}$ mm/mm. ABAQUS/Standard was used to solve the problem, with non-linear geometry activated. The model, due to its geometry and the introduction of an eigenmode as an imperfection, did not converge well. High artificial dampening was needed to obtain the results shown below, with the command *STATIC, STABILIZE.

Once the non-linear analysis was complete, the homogenization was performed with the help of the analysis described above, applying small strains through periodic boundary conditions at

different values of longitudinal strain in compression.

4.2.2 Results

The results shown here represent the effective stiffness matrix components for different values of the compressive strain. The main effect of the compression of the imperfect long RVE is a reduction of the longitudinal stiffness, an increase of the transverse stiffness and the transverse Poisson's ratio, and a reduction of the longitudinal Poisson's ratio, which becomes negative according to the results (Figure 4.5).

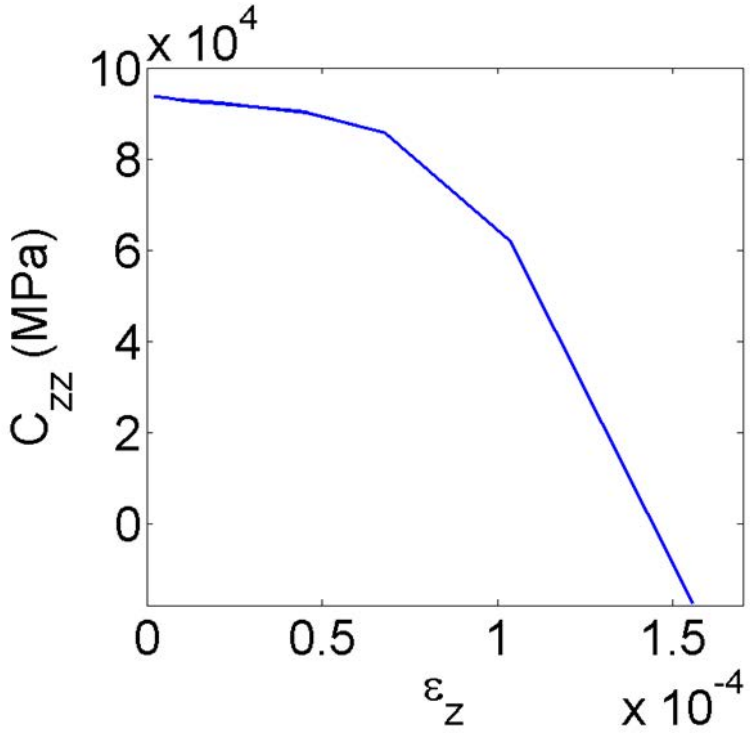

Figure 4.4: Longitudinal stiffness $C_{zz}(\epsilon_z)$ for the long RVE under compression. The initial imperfection had an amplitude equal to 10% the fiber diameter.

The values of the tangent stiffness matrix were stored for each value of ϵ_z. The effect on the effective strain in the rest of the directions was not studied in this model. Due to the difficulty in reaching convergence, longer RVEs were not studied. The effect of the length has been shown to be important, and it is still an open problem that this particular homogenization method did not cover. The effect of random distribution of fibers in the cross-section and the interaction between individual fibers under buckling may also influence the homogenization model, but it was

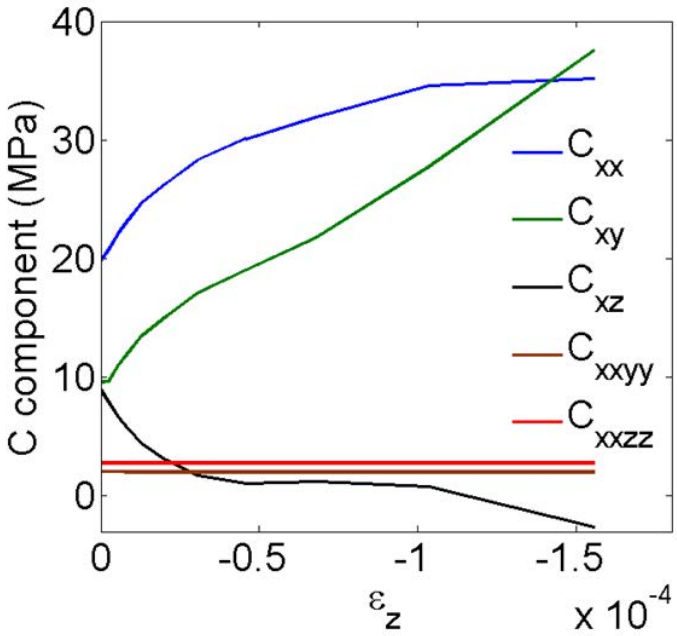

Figure 4.5: Stiffness matrix components $C(\epsilon_z)$.

not studied in this work.

The tangent stiffness values were implemented in a finite element model of the macroscopic problem, which is the unidirectional rod in compression. A comparison between the linear and the nonlinear models is included in the following chapter.

Chapter 5

Simulations on CFRS rods

This chapter describes a series of finite element simulations performed on the 50-mm CFRS rods, representing the experimental conditions for compression and torsion described in Chapter 3. The material models used in this analysis is the result of the homogenization schemes used in Chapter 4. A study of the influence on the macroscopic strength in compression of fiber angles and fiber volume fraction concentrations is included in this chapter.

5.1 Finite element model

For this model, the ABAQUS/Explicit finite element package has been used. Previous attempts using the ABAQUS/Standard solver required extremely fine meshes and high artificial damping due to the lack of convergence. Explicit solvers remove the convergence difficulties, as they advance the kinematic state of the degrees of freedom by direct integration of the equations of motion. However, explicit time integration is only conditionally stable with a minimum stable time increment that cannot be larger than the time for a wave to travel between adjacent nodes (Belytschko et al. [6]). ABAQUS/Explicit estimates the stable time at each increment automatically using

$$\Delta t = \alpha \left(\sqrt{1+\xi^2} - \xi \right) \frac{l_{min}}{c_d}, \tag{5.1}$$

where α is the time-scaling factor, ξ is the fraction of critical damping in highest-frequency mode and l_{min} the shortest length element. The dilatational wave speed is $c_d \approx \sqrt{E/\rho}$.

In quasi-static analysis, the load needs to be applied as smoothly as possible. This was done with the command *AMPLITUDE, DEFINITION = SMOOTH STEP. This command prescribes

a time variation which is a fifth-order polinomial with first and second derivatives equal to zero at the beginning and at the end of the analysis time.

The damping parameters *BULK, VISCOSITY were kept low enough so that the model was not overdamped. Generally, the validity of a quasi-static simulation is assumed if the kinetic energy to internal energy ratio is less than 1%.

The two circular surfaces representing the tips of the rod were paired with two dummy nodes in which the boundary conditions were applied. The elements that were used were C3D8, fully-integrated brick elements.

The boundary conditions were such that they represent the experiments in compression, so the surfaces where the aluminum caps would be are constrained to only move axially. Figure 5.1 illustrates the model. The compression was applied quasi-statically by imposing a displacement in the axial direction to the dummy node associated with one of the surface edges of the rod.

For the torsion simulations, the boundary conditions were such that one of the edges of the rod was fixed and the other rotated with respect to the first.

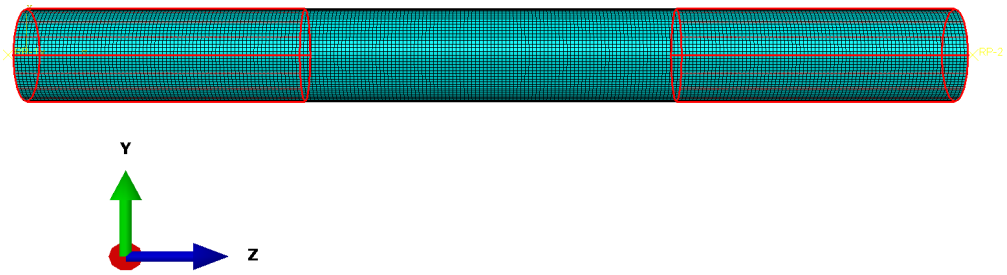

Figure 5.1: Model of the rod. The boundary conditions in the red areas are such that the surface of the rod only moves axially.

When the material from the linear homogenization (short RVE) was considered, it was assumed to be linear, and the stiffness matrix from was implemented with the command *ELASTIC, ORTHOTROPIC. For this material model, ABAQUS/Explicit assumes a quadratic strain energy density function. If the nonlinear model (long RVE) was considered, the material data from the homogenization was compiled in a table with the command *ELASTIC, TYPE = ORTHOTROPIC, DEPENDENCIES = 1. In this case, the material is assumed to be linear within the different intervals of longitudinal strain. The DEPENDENCIES command stores a table with all possible stiffness matrices, and ABAQUS interpolates them according to the dependency variable. The de-

pendency variable is called by the user-defined field subroutine at each time step. For the nonlinear homogenization, the variable of dependency was the longitudinal strain ϵ_z.

5.2 Model results

Figure 5.2 shows the stress in compression as a function of the strain in compression for a rod with zero fiber misalignment and a fiber volume fraction of 40%. The stress was calculated by dividing the reaction force obtained at a dummy node associated with the tip of the rod by the cross-sectional area of the rod. The strain in compression was calculated as the displacement of the same dummy node divided by the total length of the rod.

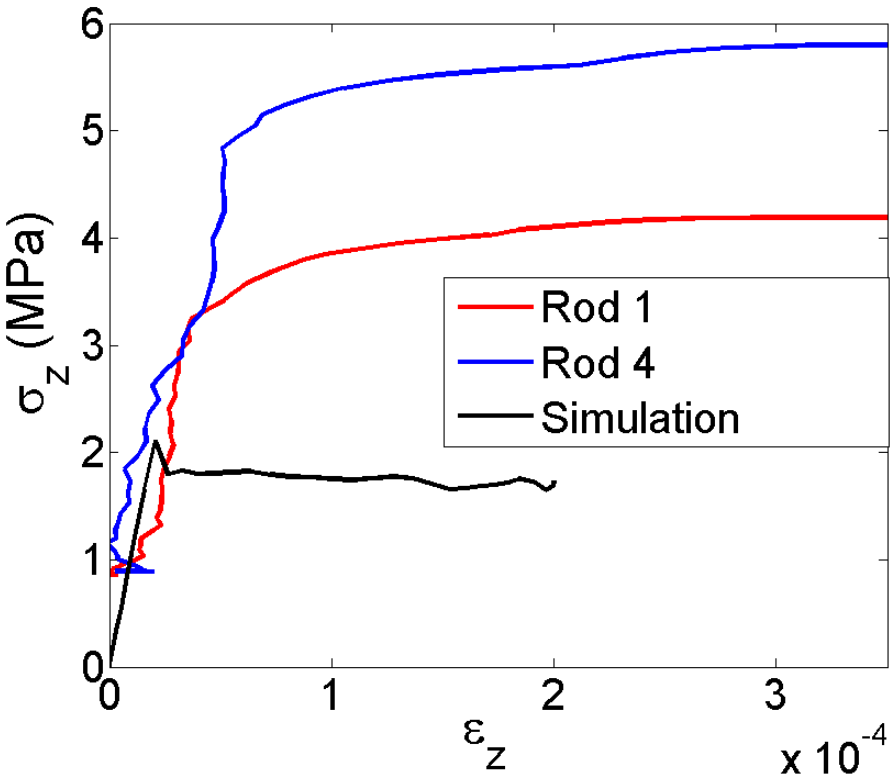

Figure 5.2: Simulation under compression of a 50-mm rod with 40% fiber volume fraction and linear homogenization material model, compared with two experiments.

The simulation shows an overshoot at the instability point. This is minimized by increasing the time interval, and therefore increasing the number of time increments to get to the final solution. Another way to do this is to soften the material at higher strains by implementing the non-linear

material model (long RVE).

The energy analysis (Figure 5.3) shows that the kinetic energy is 1.5% the value of the internal energy. Under longer simulation times, a strain energy under 1% was obtained consistently.

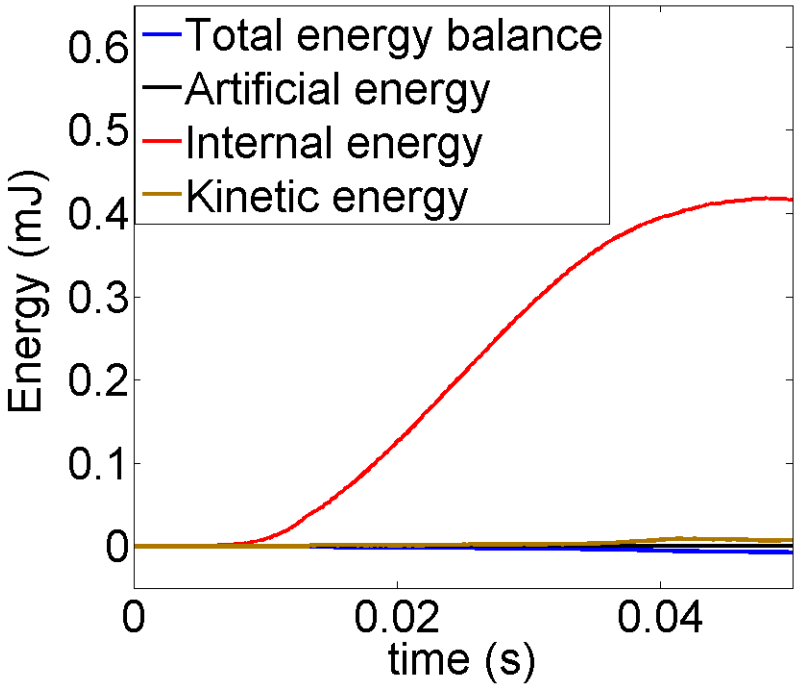

Figure 5.3: Energy balance in the model.

The simulation result is compared with two of the experiments in Figure 5.2. The resulting buckling stress is $\sim 1.6\ MPa$, lower than the stress measured experimentally. However, it is still higher than the values estimated with the analytical models.

Figure 5.4 shows the displacement values at an axial compression strain of 200 $\mu\epsilon$. Figure 5.6 shows the longitudinal shear on the surface of the rod. The deformation in the rod is amplified threefold, and shows a very local kink near the center of the rod. The shear stress changes sign across the kink. Local instabilities are not predicted by material models with a quadratic strain energy density function. The deformation has been scaled 10 times in Figure 5.6 to understand where the onset of microbuckling is originated.

A shear instability seems to be reached at the element level (Figure 5.6). From this points, the instability seems to be propagated through the elements until it forms three kinks that are dominated by the boundary conditions. For a longer compression, the kink seems to localize in the

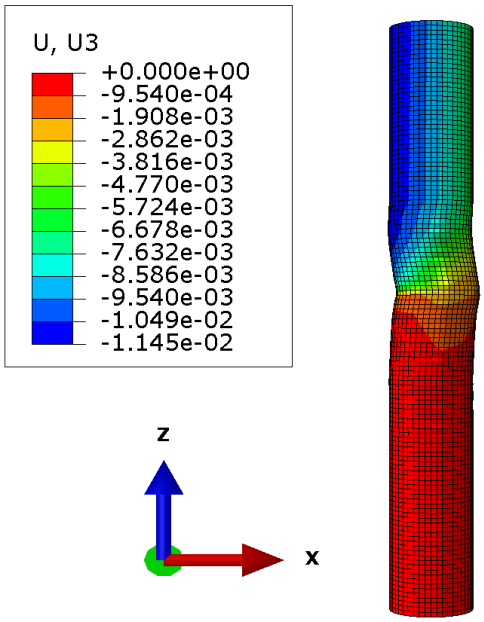

Figure 5.4: Axial displacements at $\epsilon = 200\mu\epsilon$ on a 50-mm buckled rod (post-buckled state). The deformation scale factor is 3 for this plot. Units are in mm.

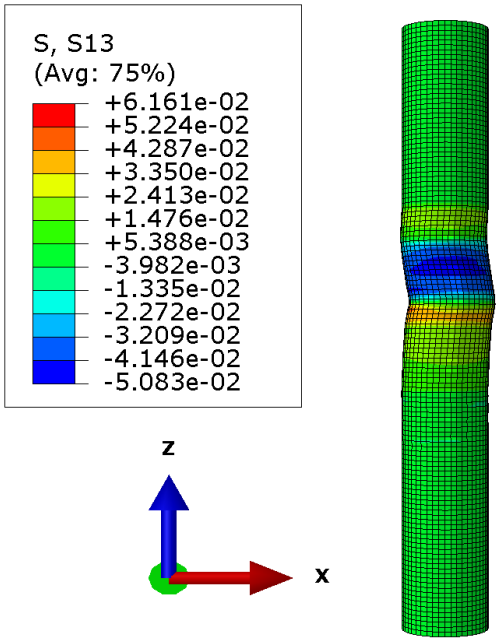

Figure 5.5: Longitudinal shear stresses at post-buckling.

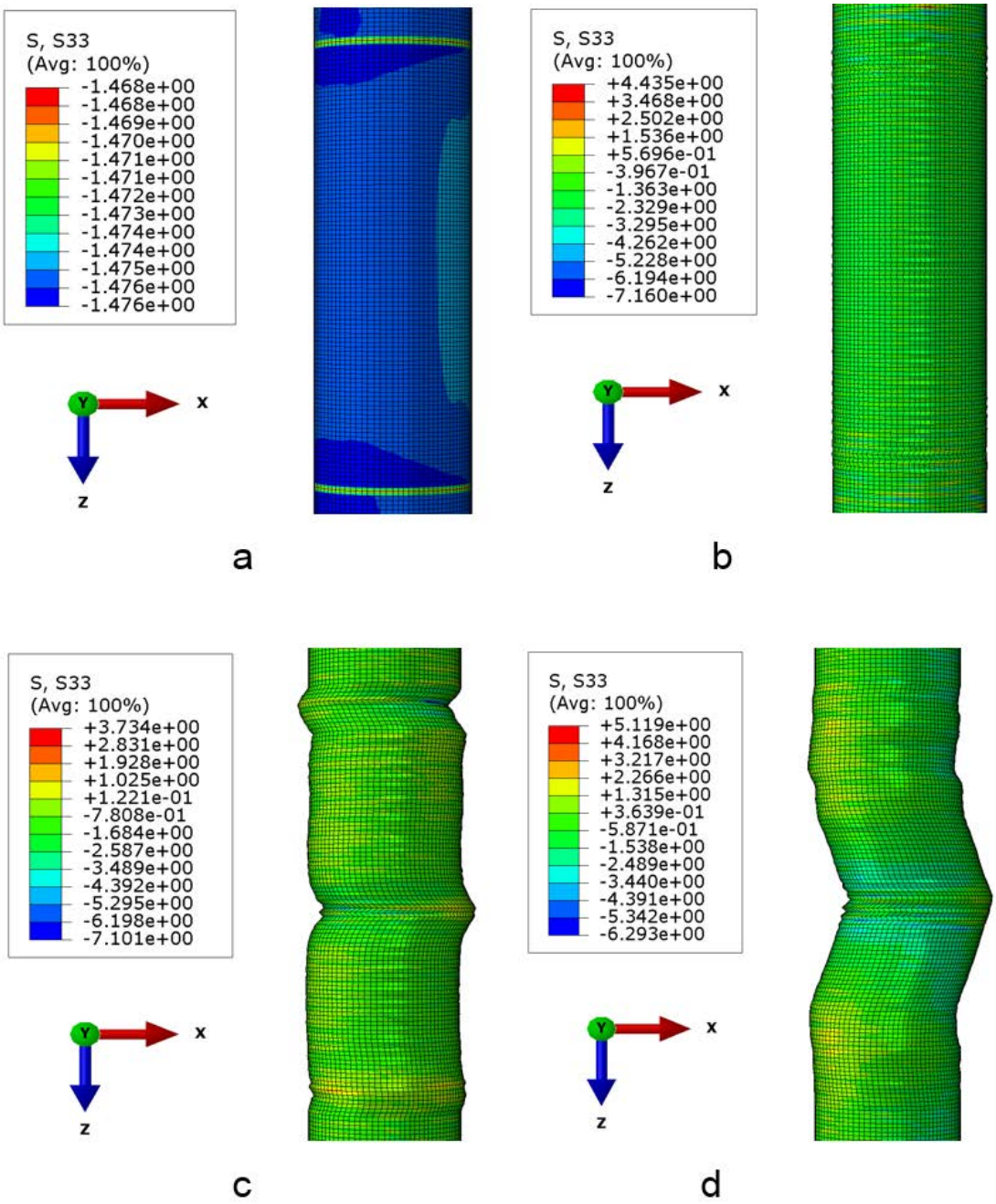

Figure 5.6: Amplified view of the center of the rod under compression. The images represent the rod before the instability is reached (a), right after it becomes unstable (b), the rod under 100 $\mu\epsilon$ (c) and the rod under 200 $\mu\epsilon$ (d). The contour represents the longitudinal stress, and is given in MPa.

center. This suggest that the onset of the instability is dominated by the high orthrotropicity of the material, rather than the macroscopic conditions. Simulations performed with different element sizes did not show an important influence (Figure 5.8). Simulations were run in rods of different lengths as well, obtaining very similar results for the onset of compressive instability.

5.3 Parametric study

Simulations were performed for different definitions of material, mesh size, time interval, or length of the rod. These simulations used a matrix of $E_m = 3$ MPa. Figure 5.7 compares the axial behavior

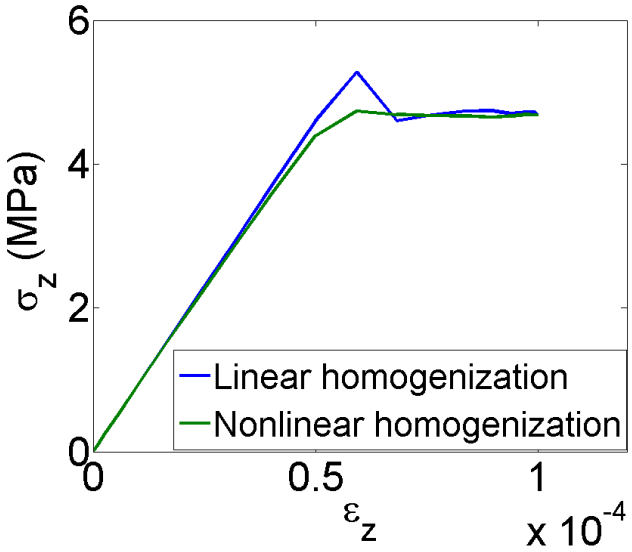

Figure 5.7: Comparison between linear and nonlinear homogenization.

of the rod for linear and nonlinear models. The nonlinear model is the nonlinear homogenization model for a fiber buckling length of 1 mm calculated in Chapter 4. The effect on the macroscopic model is a stress softening that causes the overshoot to disappear without increasing the time interval. The kinetic energy decreased as well. However, the effect of the nonlinear model may be different depending on the length of the assumed microbuckle. An incorrect estimation of the fiber wavelength will lead to a non-accurate prediction of the effect on the microscopic model. Figure 5.8 shows the axial behavior of two rods with a different element size. It seems that the refinement of the mesh increases slightly the critical stress. This simulation was run with the nonlinear model. Figure 5.9 compares the effect of the inclusion of wavy imperfections in the model. This simulation

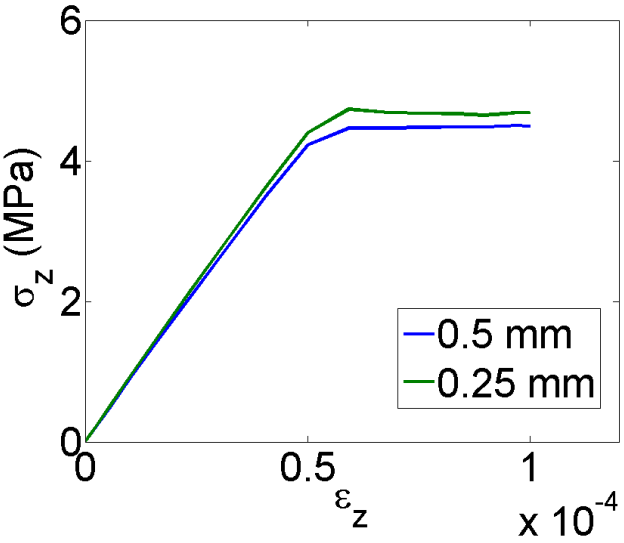

Figure 5.8: Influence of the element size.

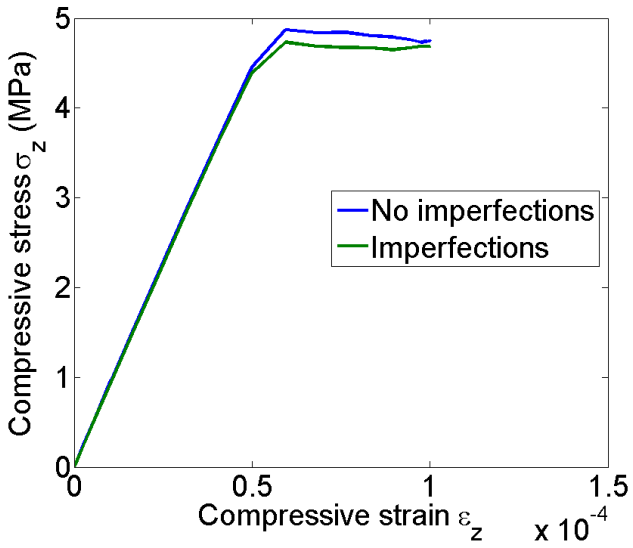

Figure 5.9: Influence of a 0.1 mm sinusoidal imperfection.

was performed with the nonlinear model as well. A sinusoidal imperfection with an amplitude of 0.1 mm and a wavelength equal to the rod length was implemented in the model. The effect of the imperfection is to slightly reduce the critical stress. The reason the effect of imperfections is not very large is because ABAQUS/Explicit introduces dinamic imperfections on the model, and that the onset of instability happens at a much smaller scale than the assumed. Other wavelengths of imperfections would need to be studied to understand this interaction.

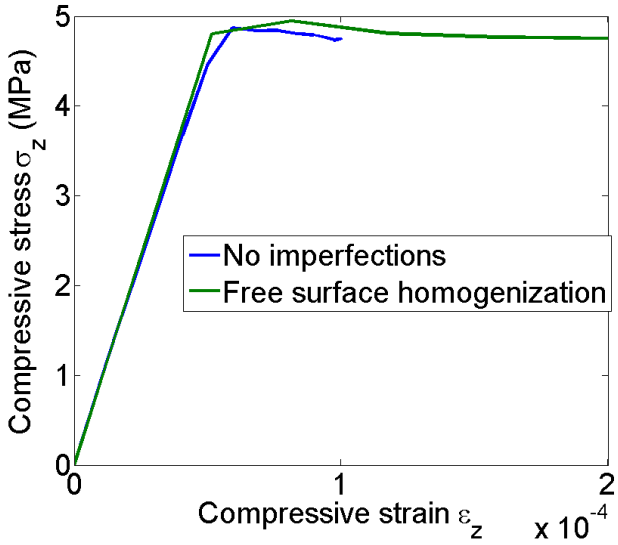

Figure 5.10: Influence of a free surface.

The homogenization model for a free surface was discussed in Chapter 4. A 2-fibers-size RVE had one boundary condition set as non-periodic, while the rest remained periodic. A linear homogenization of that RVE was done, and the results were implemented for the elements along the surface of the rod. The inner elements are modeled with the periodic homogenization. Figure 5.10 shows that there is almost no discrepancy between the two models.

5.4 Effect of fiber volume fraction concentrations

In Chapter 3 it was confirmed that the rods do not have a uniform cross section. Experimental observations suggested that fibers concentrate in the center of the rods, whereas areas where matrix predominates appear near the surface.

The effect of the non-uniform cross section is studied here. To that end, the proposed model of

the cross-section is composed of two uniform zones with volume fractions that are in the range of what has been observed from the micrographs. The average fiber volume fraction is 40%, as this is the one obtained from density ratios.

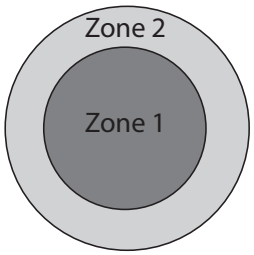

Figure 5.11: Schematic of the rod cross-section in the non-uniform V_f model.

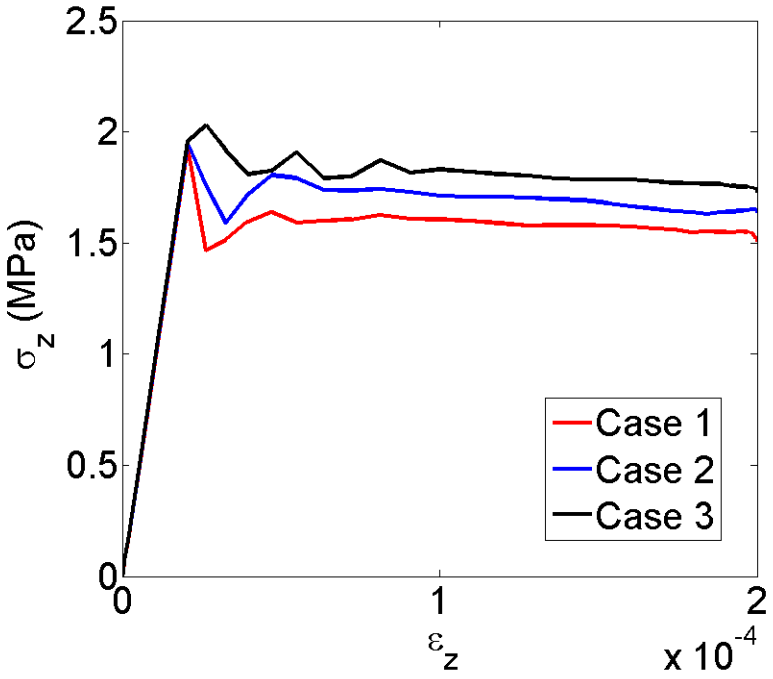

Figure 5.12: Stress-strain plots for the cases in Table 5.1.

The resulting strain-stress behavior under compression for the different cases are affected by

Case	$Zone1$	$Zone2$
1	40	40
2	50	30
3	50	20

Table 5.1: Simulated cases for non-uniform fiber volume fraction (%).

the non-uniformity of the fiber volume fraction. Case 2 and Case 3, with an increasing disparity of fiber volume fractions, shows a slight increase of the strength in compression. The buckling stress seems to be higher for the Case 3, which has the highest concentration of fiber volume fraction in the center of the rod.

5.4.1 Effect of fiber angles

The alignment of the fibers has a great effect on the effective shear stiffness of the composite, and therefore on the critical compressive stress of the rods. To take into account this effect, the stiffness matrix can be rotated. For Voigt notation, the 6x6 stiffness matrix can be transformed using a transformation matrix [12]. For a rotation around the X axis of an angle α, the transformation matrix is:

$$T_{Rx}(\alpha) = \begin{bmatrix} 1 & 0 & 0 & 0 & 0 & 0 \\ 0 & \cos^2(\alpha) & \sin^2(\alpha) & -\sin(2\alpha) & 0 & 0 \\ 0 & \sin^2(\alpha) & \cos^2(\alpha) & \sin(2\alpha) & 0 & 0 \\ 0 & \sin(2\alpha)/2 & -\sin(2\alpha)/2 & \cos(2\alpha) & 0 & 0 \\ 0 & 0 & 0 & 0 & \cos(\alpha) & \sin(\alpha) \\ 0 & 0 & 0 & 0 & -\sin(\alpha) & \cos(\alpha) \end{bmatrix}. \tag{5.2}$$

Analogous transformation matrices can be obtained for rotations around the Y axis. The transformed stiffness matrix can be calculated with

$$C(\alpha) = T_{Rx}(\alpha) C_0 T_{Rx}^T(\alpha) \tag{5.3}$$

and

$$C(\alpha, \beta) = T_{Ry}(\beta) C(\alpha) T_{Ry}^T(\beta), \tag{5.4}$$

assuming we have angles in the X and Y directions. C_0 is the stiffness matrix with zero misalignment. $T_R = T_{Rx}T_{Ry}$ is the total rotation of the fibers around the X and Y directions.

Fiber angles are not the same throughout the rod. Assuming that the fibers are continuous and all of them go through the start and end cross-sections of the rod, there can be different fiber angles inside the rod, but with an average value of zero.

From the experimental measurements in Section 3, a probability function of the fiber angles was estimated. The stiffness of the material is not uniform due to the angles, and therefore an effective global stiffness needs to be estimated. To that end, the probability function of the fiber angles was used. As the stiffness matrix is a function of the fiber angle, a Taylor averaging model has been used to estimate the effective stiffness. This is equal to the expected value for any particular probability density function [25]:

$$E[C(\alpha)] = \int_{-\infty}^{\infty}\int_{-\infty}^{\infty} C(\alpha,\beta)p(\alpha)p(\beta)d\alpha d\beta. \tag{5.5}$$

$p(\alpha)$ and $p(\beta)$ have been taken as equal. The expected value of the stiffness matrix depends on the standard deviation of the normal distribution. Once the expected value of the stiffness matrix was obtained, it was implemented on the finite element model of the rod. Analysis for angle distribution of standard deviation 0.3^0 (the minimum local standard deviation) and 0.92^0 (the overall standard deviation), observed in the characterization of the microstructure in Chapter 3, were compared to the results with no misalignment and experiments. The probabilities for angles in the Y and X direction were taken as equal.

It can be observed in the plots that the measured critical stress is closer to the critical stress obtained with the simulation at a 0.3^o misalignment standard deviation than to the critical stress obtained with no misalignment at all. If the standard deviation of the global distribution of misalignments, i.e., accounting all the measured zones $\sigma_\alpha = 0.92^o$, is used in the simulations, the critical stress increases to 40 MPa.

From these results it can be confirmed that the critical strength in compression of this material is highly sensitive to the fiber angle distributions. This is a direct effect of the highly orthotropicity of the material, due to the great increase in the longitudinal shear stiffness of the composite with the standard deviation of the fiber angle distribution. The model seems to find a "bracing" effect when a standard deviation is consider in a normal distribution of fiber angles, which is symmetric

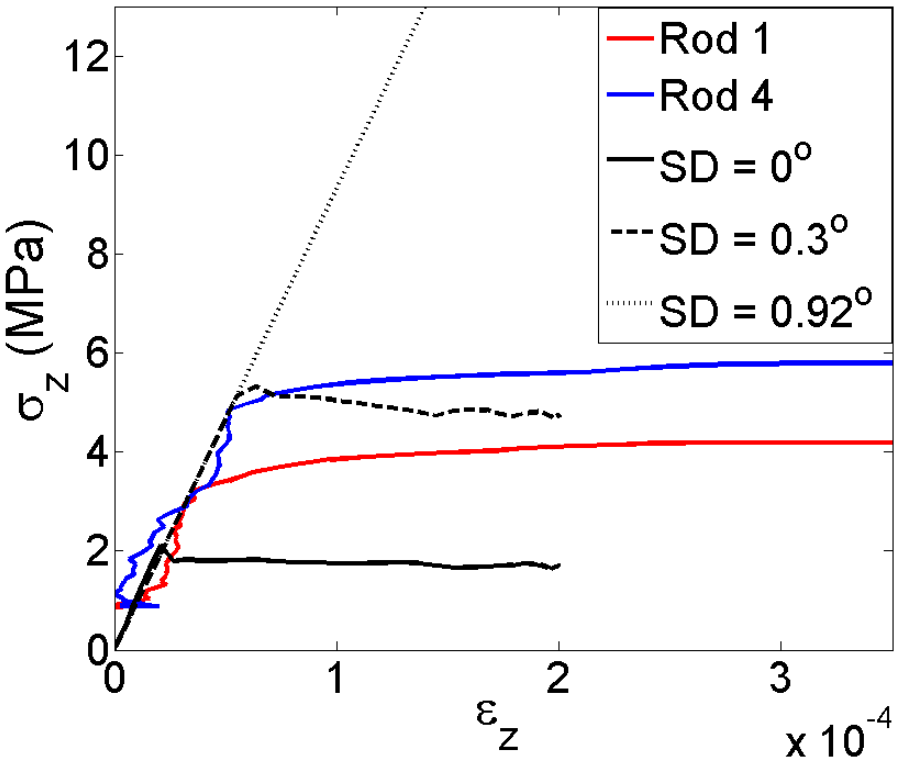

Figure 5.13: Compressive behavior of rods with minimum-local and overall standard deviation angle distributions and comparison with experiments.

respect to the mean. In order to determine the influence of the mean fiber angle on the critical stress, simulations were performed with the corresponding effective stiffness, for uniform angles and for a distribution with a standard deviation of 0.2^o.

Figure 5.14 shows that the compressive strength decreases with the mean fiber angle. The mean has a larger influence for larger values of standard deviation. However, a mean fiber angle effectively increases the shear stiffness of the material. The reason why the strength decreases is because couple components of the effective stiffness matrix are not longer zero when the mean fiber angle is not zero, which breaks the symmetry.

From these results, it can be concluded that the standard deviation, or the presence of symmetric fiber deviations respect to the nominal direction, cause a "bracing" effect that increases the shear stiffness of the material, and therefore increases the compressive strength. The mean angle has a much smaller effect than the standard deviation, and it decreased the compressive strength.

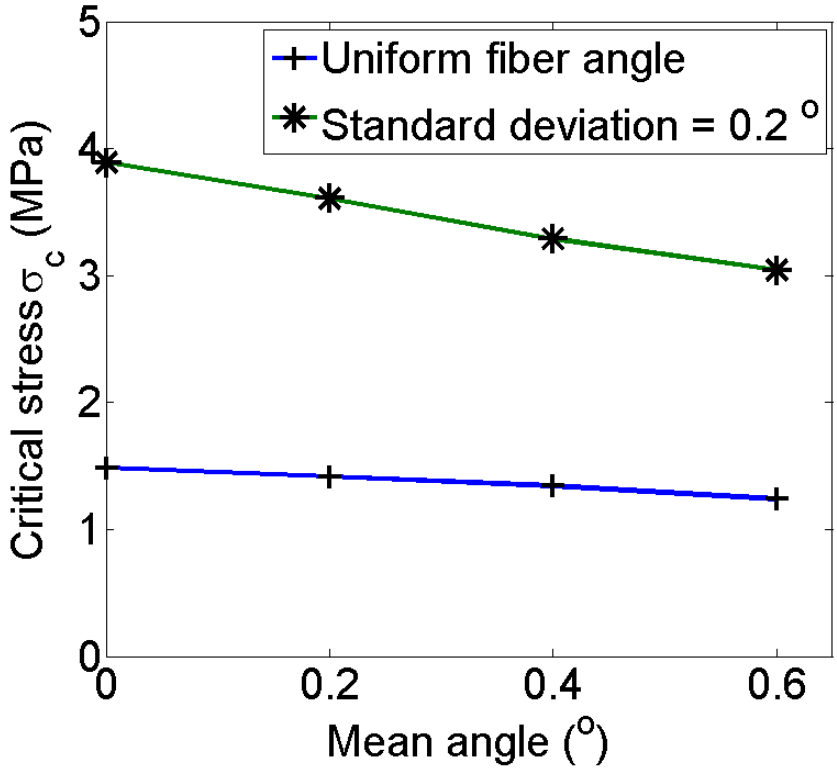

Figure 5.14: Effect of the mean fiber angle on the compressive strength for rods with uniform angles and with a distribution of standard deviation equal to 0.2^o.

The effect of the fiber angles on the CFRS material was also calculated analytically assuming Neo-Hookean phases and using Equation (2.21). For similar angles to the ones used in the simulation, the increase of the critical stress due to the fiber angle was not significant if the analytical approach was considered. This discrepancy was thought to be due to the assumption of a constant angle for the analytical model, whereas an angle distribution with zero mean was considered for the simulations.

5.4.2 Torsion simulations

The orthotropic material model obtained with homogenization was used to calculate the behavior of the rod in torsion and compare it to the experimental measurements. The effect of the standard deviation of the fiber angle distribution was studied as well. The effective shear stiffness (or the effective torsional stiffness) increases when the standard deviation increases. The material model

used for these simulations was the same model used for the simulations of the rod in compression. This simulation were run in ABAQUS/Standard. The applied boundary conditions are such that one of the ends of the rod is clamped, while a prescribed rotation is applied to the other end.

Figure 5.15 plots the evolution of the torque at different values of the torsional angle. Simulations were done for a 50 mm rod with different distributions of the angle misalignment, and compared with the torsional experiment. The effect of the fiber angle distribution on the torsional stiffness, and therefore the shear stiffness G_{xz}, can be seen clearly in this plot.

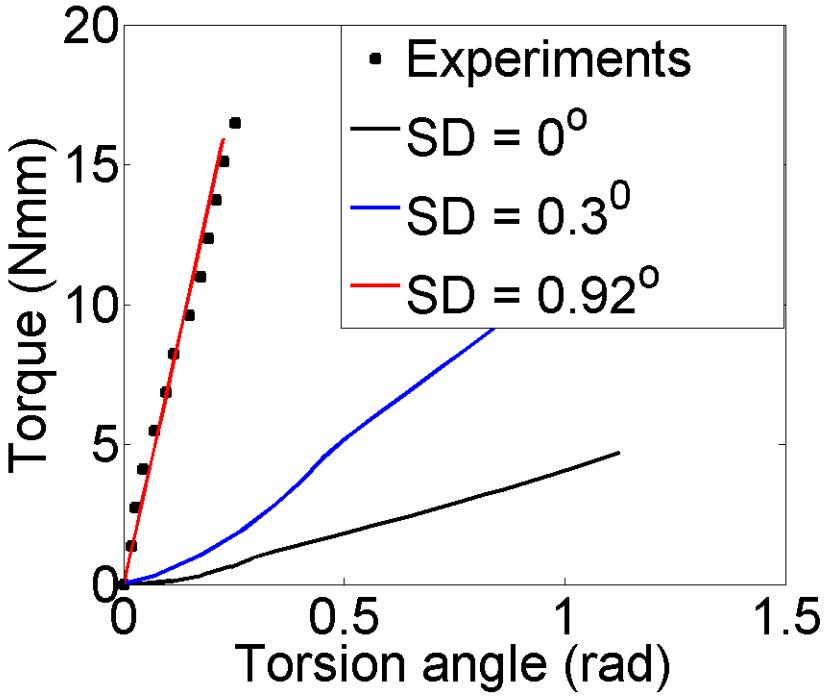

Figure 5.15: Torsional behavior of a 50 mm rod with different fiber standard deviation and comparison with experiments.

The increase of torsional stiffness in each analysis is due to the slight change in angle of the elements when the rod is under torsion. The sudden change in curvature that is observed on the simulation with no misalignment and the case with $\sigma_{alpha} = 0.3^o$ is due to buckling of the elements under longitudinal compression. The longitudinal stress at which those elements are reaching instability coincides with the buckling stress predicted in the previous subsection.

For a misalignment of 0.92^o in standard deviation, the simulation approaches the experiments very well. This indicates that by using the global statistical information of angle misalignment,

the effective shear stress of the composite can be estimated. This, however, is not the case for compressive strength, as the distribution with $\sigma_{alpha} = 0.25^o$ agrees best with the experiments.

It is believed that this discrepancy occurs because the stiffness is dominated by the global material, and the strength is dominated by local effects. Torsional stiffness is a global characteristic of the material, and if non-uniformity exists, it can be averaged to obtain this global property. However, buckling occurs locally. The zones with the smallest shear stiffness buckle first, and that creates local instabilities like the ones observed in the experiments.

The main limitation of the averaging model for the assumed angle distribution is that the interaction between fibers, which can lock at microbuckling when they are not parallel, cannot be evaluated. This model also assumes that scales are separated, i.e., the scale at which the fiber angles change is much smaller than the macroscopic scale of the model. Therefore, imperfections will not have important effects in the onset of the instability.

Modeling these effects with a homogenized non-linear material, and taking into account the different distributions that were measured along the rods, would yield more accurate results, specially during the postbuckling regime. However, the model presented here provides a very important result, which is the effect of small fiber angles on the compressive strength and the torsional stiffness of the composite.

Chapter 6

Dual-matrix composites for foldable shell structures

High strain composites have been proposed for autonomous deployable structures applications in the form of hinges or membrane-like shells with high in-plane but low out-of-plane stiffness. Microbuckling allows the material to reach high strains at a fold while minimizing or completely avoiding fiber damage, and at the same time storing enough strain energy to self-deploy when released.

This type of material, however, cannot be used in applications that require high stiffness out-of-plane, as is the case in laminate shells, or in high transverse and torsional stiffness, as is the case in unidirectional composites. Additionally, these materials present great resistance to bonding to other materials, making it difficult to integrate them as elements in complex deployable structures.

To address this issue, dual-matrix composite shell structures are considered. These structures are made of a continuous laminate that reinforces both stiff and high strain matrices. With this design, the shell can be folded in the regions with a high strain matrix and shows high stiffness out-of-plane in the regions embedded with the high stiffness matrix. With dual-matrix composites, the problem of low stiffness out-of-plane is solved, and the presence of stiff regions provides the capability of being bonded or connected to other structural elements.

There have been several recent approaches to this concept. Todoroki et al. manufactured a "partially foldable" shell made of woven carbon fiber and embedded with epoxy resin and silicone rubber [63]. The structure was folded and deployed while applying heat to several shape-memory alloy (SMA) rods embedded in the material (Figure 6.1). The manufacturing process involved adding heat-cure silicone to the folding regions and adding the epoxy resin after the silicone was

cured.

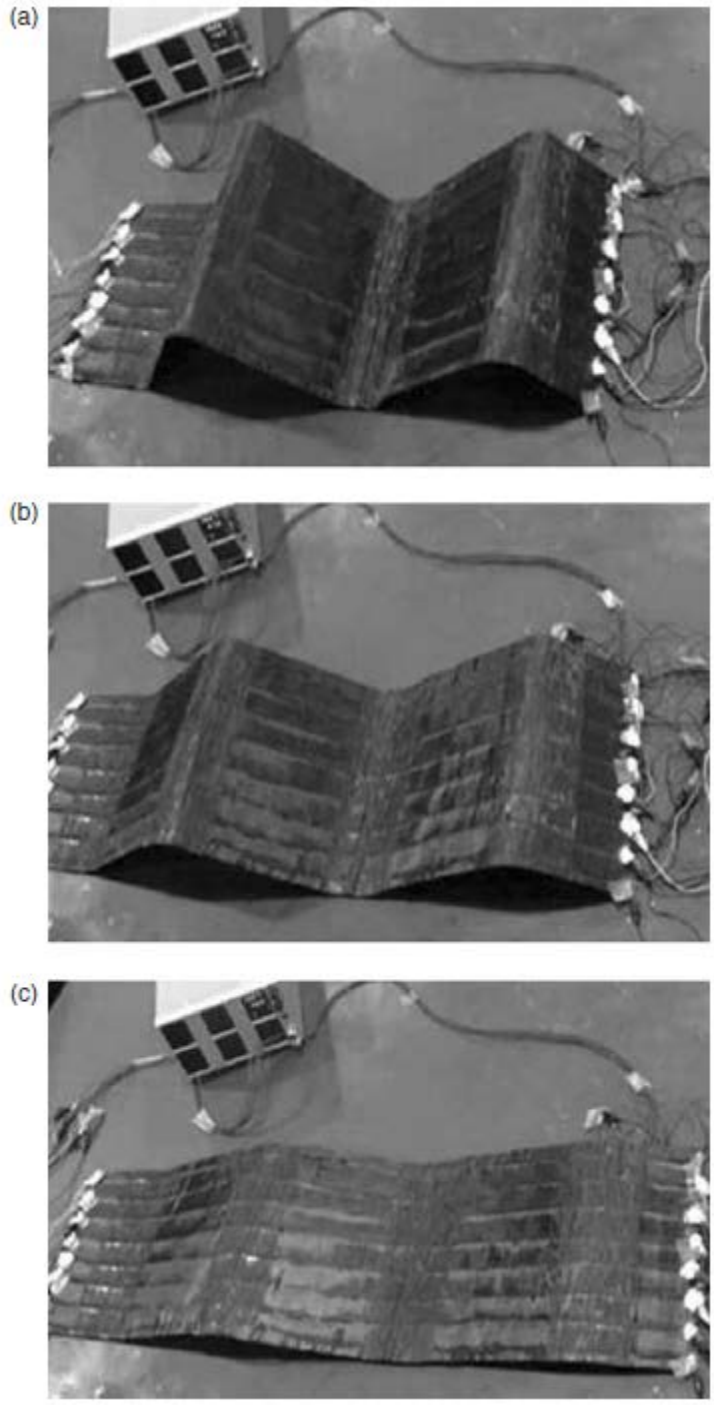

Figure 6.1: Deployment of a dual-matrix carbon composite shell using SMA rods embedded in the mid-plane of the composite, taken from Todoroki et al. [63].

Saito et al. developed a method to fabricate dual matrix woven carbon sheets with silicone and epoxy matrices [57]. In this method, the epoxy resin is cured first, and the silicone is then applied to the dry folding regions. The method incorporates complicated folding patterns to create origami shapes with the use of masks (Figure 6.2). The process was used to fabricate origami honeycomb structures.

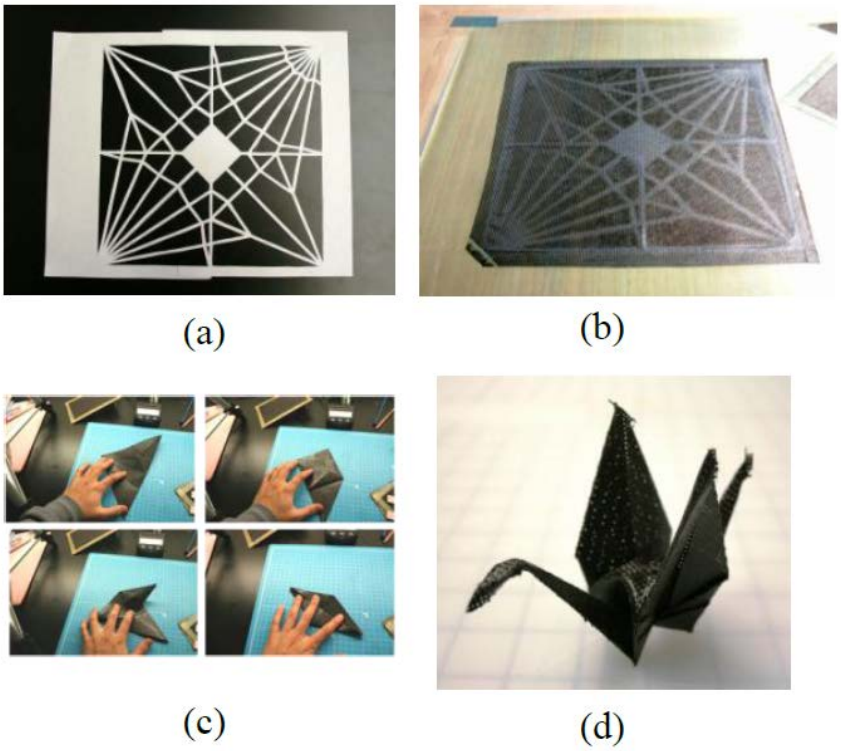

Figure 6.2: Fabrication of an origami crane with a dual-matrix composite. (a) Pattern mask. (b) Dual-matrix composite sheet. (c) Folding process. (d) Final folded shape. Deployment of a dual-matrix carbon composite shell using SMA rods embedded in the mid-plane of the composite. Taken from Saito et al. [57].

Similarly, L'Garde Inc. has worked on dual-matrix carbon shell composites with heat-cure silicone and epoxy resin. Figure 6.3 shows the folding of a Miura-ori woven carbon shell.

In this chapter, the disadvantages of the manufacturing techniques used in the mentioned works are described, a new technique that improves the previous methods is proposed, and several concepts of dual-matrix structures are presented. Additionally, the properties of a quasi-isotropic dual-matrix Astroquartz shell fabricated in the laboratory are estimated, and the pre- and post-fold behavior of dual-matrix Astroquartz hinges is studied.

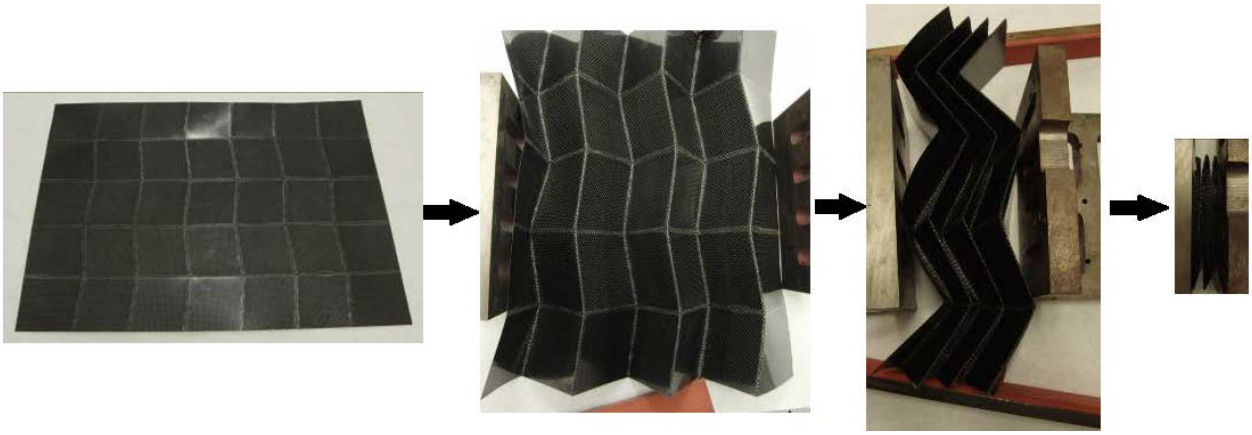

Figure 6.3: Folding of a Miura-ori dual-matrix woven carbon shell. Courtesy of L'Garde.

6.1 Approach

Every dual-matrix manufacturing process described above used a woven carbon cloth, heat-cure silicone rubber, and epoxy matrix. Heat-cure silicones with the desired properties are commercially available, and many of them are NASA-outgassing approved for space applications.

However, there are several problems related to the use of heat-cure silicones for dual-matrix applications:

- Silicone rubbers have low thermal conductivity, causing a slow and non-uniform curing process. This increases the risk of bubbles forming in the silicone, even if vacuum has been applied to the silicone before curing.
- Assuming that the silicone has low enough viscosity to impregnate the woven carbon fabric through the thickness, the slow curing time allows the silicone to flow into undesired regions.
- Another approach is to cure the epoxy resin first. Capillarity may cause the epoxy to flow into dry regions during the curing process, which can cause stiff resin to be present in the folding regions.
- A common issue with heat-cure silicone is that it presents cure inhibition when in contact with other materials or moisture. Attempts to use heat-cure silicone in the laboratory presented inhibition, likely due to the epoxy resin or the sizing of the carbon fibers.

The process described in this chapter attempts to address these issues through the use of an

ultraviolet (UV)-cure silicone. UV curing is a photochemical process in which UV radiation (light in the range of 100 - 400 nm) is used only to initiate the catalytic curing reaction. As the silicone is UV-transparent, the degree of cure through the thickness is uniform. The UV exposure time of this type of silicones can be as low as 0.5 seconds, and the curing can be performed at low temperatures.

Due to the fast curing time, the flow of the silicone towards undesired regions before curing is minimized. UV cure silicones are not as sensitive to other chemicals as heat-cure silicones, presenting less or no inhibition to cure. Additionally, the quick surface cure does not trap voids within the laminate.

UV energy can only penetrate optically transparent material, so it cannot be used with carbon fibers unless each ply is cured separately. While fiberglass is optically transparent, UV energy will not penetrate further than 13 to 19 mm into the material, requiring thick laminates to be cured separately as well.

For these reasons, the materials used to create dual-matrix composites are fiberglass, epoxy and UV-cure silicone.

- Epoxy: the Hexply® 913 epoxy resin delivered in a impregnated film, which, once heated, transfers the resin to the dry fabric. The advantage of using epoxy film over liquid epoxy or pre-impregnated fabric is that the film can be cut in different shapes, allowing a good definition of the geometry of the folding area.

- Silicone: The UV-curing silicone LOCTITE® 5055 ™ has similar mechanical properties to the silicone studied in previous chapters [30]. It has been selected due to its viscosity in an uncured state, which is low enough to spread through the thickness of the glass fabric, and high enough so that the fibers can be impregnated in a controlled way. LOCTITE® 5055 ™ is an alkoxy silicone, which comes in one liquid component. The silicone cures up to a depth time of 4 mm in 60 seconds, with an UV radiation of 70 mW/cm^2 and a wavelength of 365 nm.

- Fiberglass: the triaxial weave fiberglass SAKASE SK-1015 has been used to detail the manufacturing process and to fabricate some prototypes. For stiffer shells, an Astroquartz® II 525 plain weave fabric from JPS composites was used. Astroquartz® II fibers are high-strength fibers with a 99.99% silica content. This material is used in applications in which a low

dielectric loss is required, such as antenna applications.

The properties given by the manufacturers are shown in table 6.1.

Material	ρ (g/cm^{-3})	E (GPa)	Tensile Strength (MPa)
Epoxy	1.23	3.39	65.5
Silicone	0.98	0.002	9.3
Astroquartz®	2.2	72	6000

Table 6.1: Properties of silicone, epoxy, and Astroquartz® (provided by the suppliers). ρ is the density and E the elastic modulus.

6.2 Manufacturing process

In this section, the fabrication of a Miura-ori foldable panel is described to clarify the manufacturing process. Miura-ori is a folding pattern for thin sheets that has been extensively investigated by mathematicians, physicists and engineers [42, 11].

6.2.1 Shell description

The manufactured shell is a two-ply triaxial-weave fiberglass that can be folded trough a Miura-ori pattern [42] (Figure 6.4). The folding lines are 5 mm wide and embedded in silicone matrix. The remainder of the shell is embedded in the stiffer epoxy matrix. The dimensions of the shell are 160 mm long and 130 mm wide, with a thickness of $\sim$0.3 mm.

6.2.2 Fabrication

The manufacturing process is composed of the following steps:

1. The glass fabric is cut with the required geometry and direction of each lamina. It is recommended to use a box cutter and to apply pressure on the fabric near the cut so there is no distortion in the fibers.

2. The individual laminas are extended over a PTFE sheet to avoid any adhesion of epoxy or silicone on the working area.

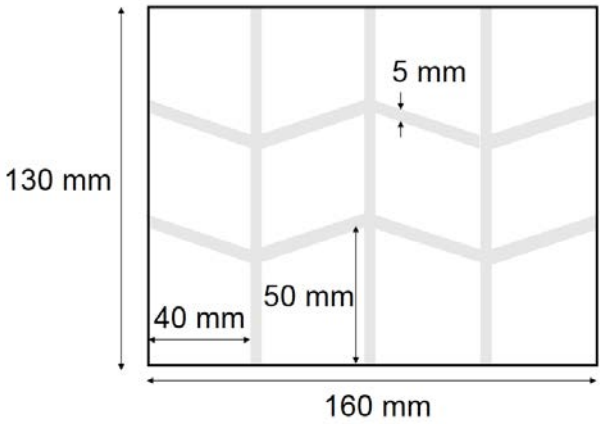

Figure 6.4: Schematic for the Miura-ori shell. The grey area represent the folding lines, which is where the silicone matrix is added.

3. The epoxy film is cut according to the desired geometry. The pattern can be drawn or printed on the back of the protective layer of the epoxy film.

4. The epoxy film is placed on the desired areas of the dry fabric. The distance between epoxy regions should be $\sim$ 5 mm, which will be the width of the fold. The resin can be transferred to the fabric through the application of heat (Figure 6.5). Generally, one layer of epoxy per lamina is needed.

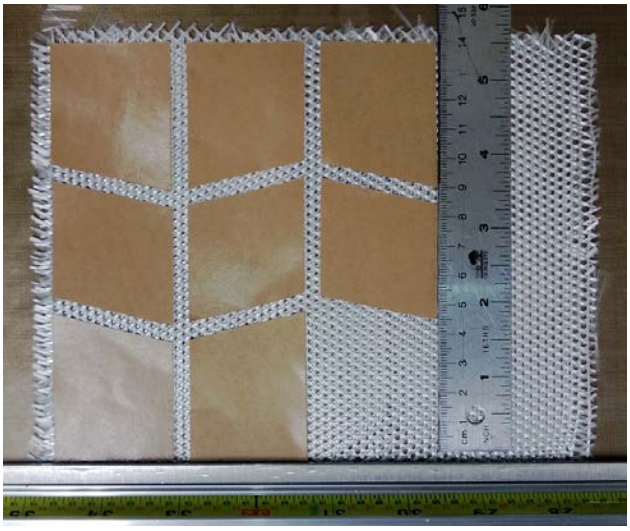

Figure 6.5: Epoxy film pieces placed on the fabric. The brown-colored paper is the protective layer of the epoxy film. The protective layer is kept in place to mask the UV light so the silicone does not cure inside the epoxy areas.

5. The laminate is made by stacking the individual laminas in the required direction. The epoxy protective layer of the last lamina is kept in place to act as a mask during the curing of the silicone. For the Miura-ori shell, two plies are used, both with the same direction.

6. The liquid silicone is applied to the folding lines (Figure 6.6). A syringe can be used to control the amount of silicone applied. For the 2-ply laminate, the estimated amount of silicone added is 0.1 ml/cm^{-2}. To ensure uniformity in the distribution of the silicone, the silicone-impregnated areas are pressed with a polyurethane foam swab. This results in a total volume fraction of fiber in silicone of $V_{f,s} = 50\%$ inside the tows, whereas for the whole cross-section $V_{f,s} = 20 - 30\%$. This is due to the presence of silicone on the surface of the shell and between the plies. The fiber volume fraction in epoxy is $V_{f,e} = 60\%$. The thickness of the shell is ~ 300 μm.

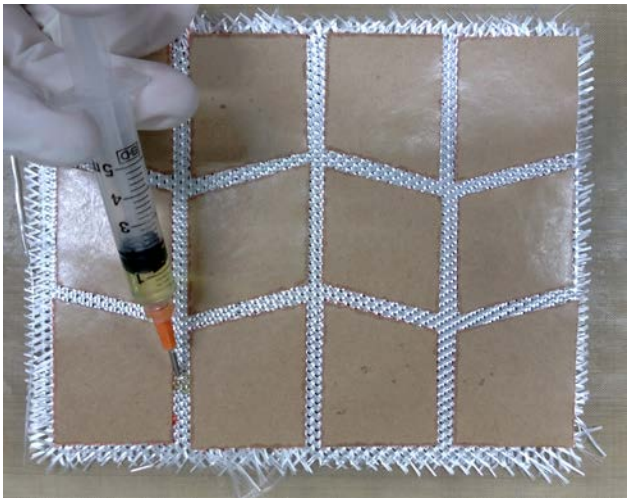

Figure 6.6: Application of the silicone to the dry areas between the epoxy regions.

7. The silicone is cured with a UV lamp. The lamp used to cure the prototype is a Spectroline XX15A. This lamp radiates UV-A light (315 to 400 nm in wavelength) with an intensity of 1.1 mW/cm^2 from a distance of 25 cm. The distance between the lamp and the shell is 4 cm, which results in an irradiance of approximately 40 mW/cm^2 With this exposure, the curing time is no more than one minute for the thickness of this laminate. The silicone that flows outside the folding lines does not cure, due to the masking of the UV light by the epoxy film that has not yet been removed. Having transferred the epoxy to the fabric before the silicone was applied prevents the silicone from spreading too far, as capilarity was reduced. Figure 6.7

shows the shell under the UV lamp during the curing of the silicone matrix.

Figure 6.7: UV curing of the silicone. The epoxy film paper acts as a mask so that the silicone only cures in the exposed area. The curing time is less than one minute.

8. Once the silicone is fully cured, the epoxy protective film is removed from the shell. A release film and a breather is placed on top of the shell. Then, a vacuum bag is placed and sealed with vacuum tape.

9. The epoxy is cured in vacuum for one hour at 125 ^{o}C and 600 kPa.

The Miura-ori shell manufactured with this process was easily folded into a very compact configuration, and the stored strain energy in the folding lines allows it to return to the original state when released. Figure 6.8 shows the shell in the original configuration, in two partially stowed states and in the highest compaction configuration.

The fabricated shell presented a good foldability and was autonomously deployed when released. No fiber failure was observed around the fold lines. The curvature radius of the folds was $\sim$ 1 to 2 mm. Figure 6.8 shows darker areas near the folding lines. This indicates that the matrix and the silicone mixed. However, the regions are small, and they do not seem to be less stiff than the rest of the epoxy regions.

6.3 Examples of deployable dual-matrix composite structures

In this section, two examples of dual-matrix composite concepts are discussed. Another concept that uses a dual-matrix composite shell for a CubeSat antenna application will be detailed in Chapter 7.

One of the concept prototypes that was built in the laboratory is a foldable tubular shell boom. This boom presents two parallel and diametrically opposite hinge lines at each side, which allows

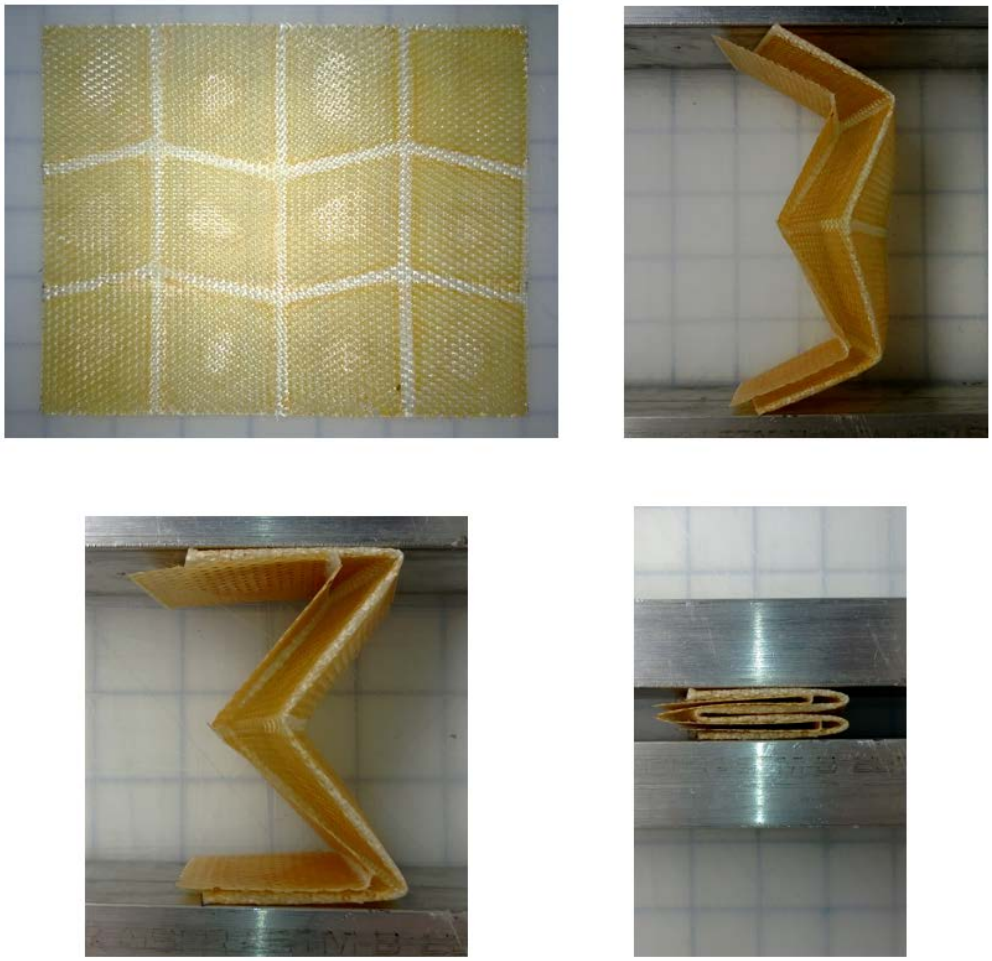

Figure 6.8: Dual-matrix fiberglass Miura-ori shell, from flat to folded configuration.

the boom to be flattened into a rectangular configuration. From the flattened state, the boom can be coiled or s-folded elastically for maximum compaction, and can be flattened as well. Compared to current tape-spring-based booms, this one can potentially reach higher torsional stiffness.

The boom shown in Figure 6.9 is made of a one ply triaxial weave lamina. The silicone was cured on the flat lamina, and the lamina was then impregnated with epoxy and wrapped around a cylindrical mold. The mold used to fabricate the boom was an aluminum tube of 25 mm diameter. The tube was made with a length of 300 mm. The fold lines were made 10 mm wide. The radius of curvature reached in the fold lines is $\sim$ 2 mm.

The hinges showed microbuckling for relatively high values of curvature and a post-microbuckling effect when they were completely folded. The cylinder stored the strain energy of the soft hinges

and the energy of the stiff regions due to the change in curvature that occurs when flattening and coiling. The result was an autonomous deployment from the folded configuration.

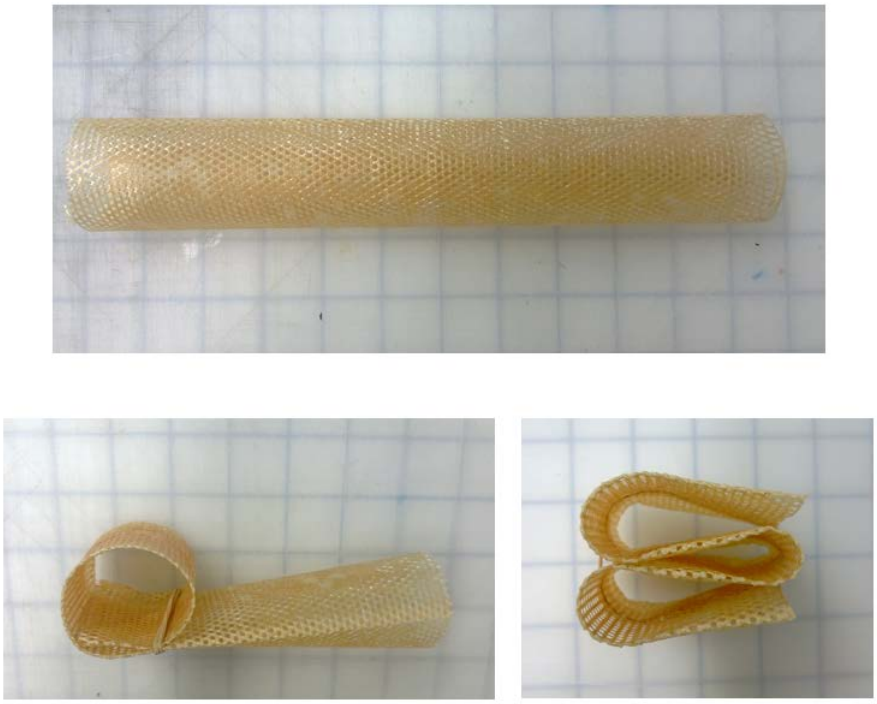

Figure 6.9: Foldable boom, deployed, in a partial coiled configuration, and s-folded.

Another prototype, which combined the techniques above, was a deployable cylindrical shell foldable into a Miura-ori pattern. This structure could support a foldable helical antenna, and can be an alternative design to the helical pantograph proposed by Olson et al. [47]. The conductor for the antenna could be placed on top or integrated with the laminate. More details about foldable antenna concepts will be provided in Chapter 7.

This concept was manufactured in the laboratory in collaboration with G. Olson. The shell was made of a two-ply triaxial weave fiberglass laminate. First, a 2-ply laminate of 250 mm by 380 mm was prepared using the manufacturing technique previously described, using a Miura-ori pattern to define the hinge lines. Then, the laminate was wrapped around a cylindrical aluminum mold.

Figur 6.10 shows the shell deployed, flattened and folded. The compaction ratio is 28:1. The cylindrical shell can be flattened first and then folded by the Miura-ori pattern. The shell can self-deploy using the strain energy stored in both the initially curved epoxy panels and the silicone

creases.

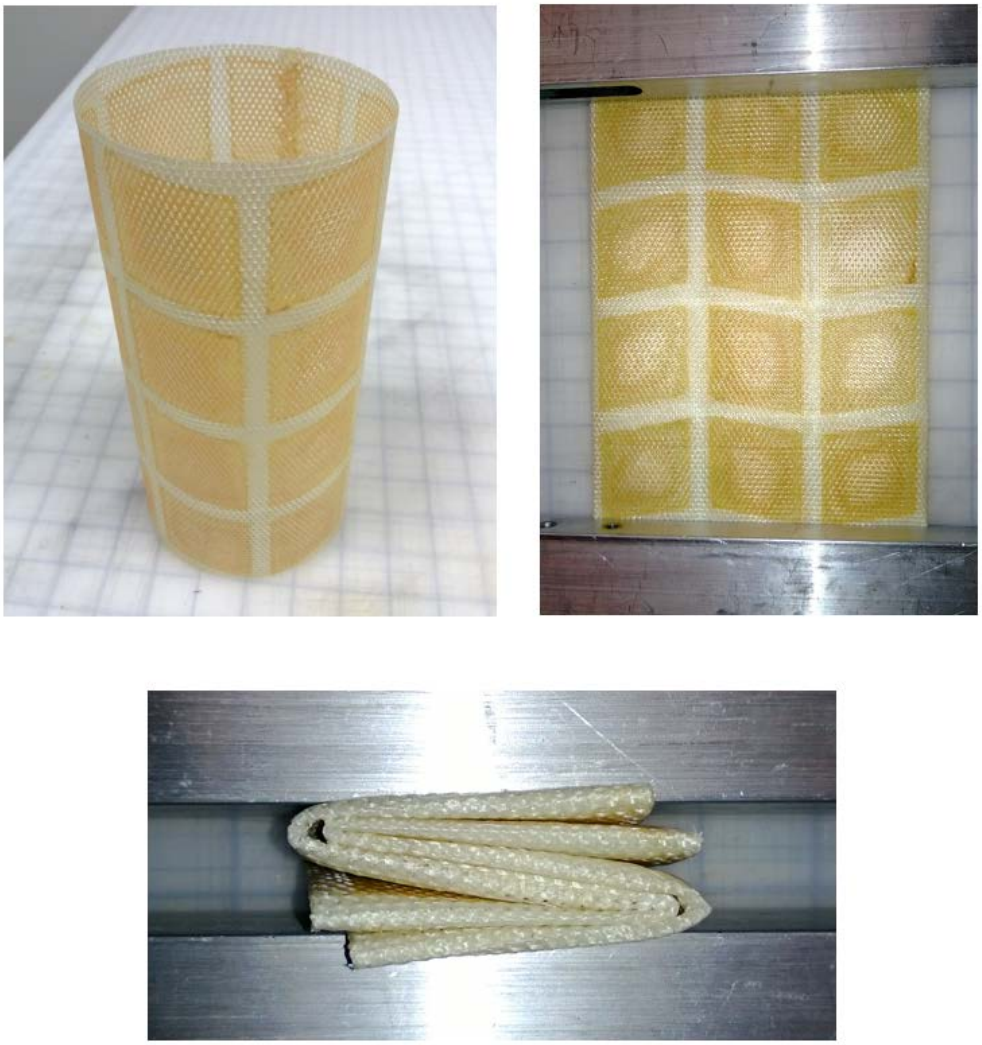

Figure 6.10: Dual matrix fiberglass cylinder, flattened and Miura-ori folded.

The dual-matrix shell concept can be used with many different fold patterns and shell shapes, and is able to achieve extremely tight compaction ratios.

6.4 Quasi-isotropic foldable Astroquartz composite

The prototypes described above use the SAKASE triaxial weave fiberglass. This fabric presents large spaces between fiber tows, reducing its out-of-plane stiffness. For this reason, the Astroquartz® fabric has been used to perform a more detailed characterization.

Many applications require the use of a quasi-isotropic material, i.e., the properties of the material are similar in different directions. Triaxial weave is considered to be quasi-isotropic, as it presents fibers at every 60^o. Symmetry is also desired to avoid coupling stiffnesses, which could cause warpage due to environmental changes.

With a plain-weave fabric, warp and weft tows are woven perpendicularly. Taking the angle of one of the woven tows as a reference, a possible quasi-isotropic symmetric laminate could be $[0/45]_s$, where s indicates the symmetric laminate. This laminate is a 4-ply plain weave that presents tows at every 45^o. However, samples made in the laboratory with this configuration were not sufficiently stiff, so a thicker laminate was required.

The laminate $[\pm 30/0]_s$ is also quasi-isotropic, as it is composed of 6 plain weave laminas that have tows at every 30^o (Figure 6.11). The samples fabricated in the laboratory with this configuration were stiff enough, and enough strain energy was stored at a fold that the deployment was autonomous.

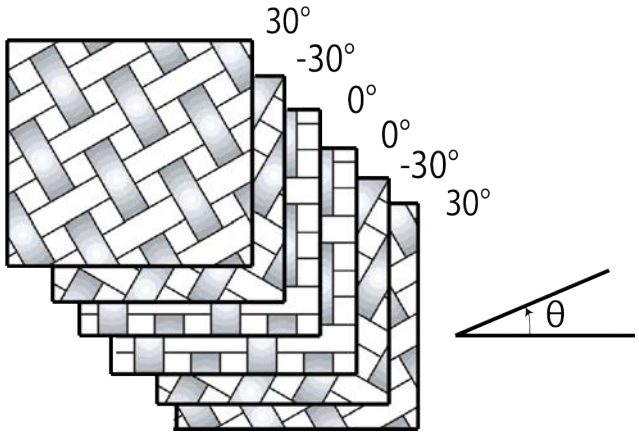

Figure 6.11: Lay-up of the $[\pm 30/0]_s$ plain weave laminate

In this section, the properties of this laminate are estimated with Clasical Laminate Theory (CLT) and classical micromechanical models of the lamina. The results will be used for a structural concept presented in Chapter 7. A brief experimental study of the behavior of the hinge is also included.

Figure 6.12: Astroquartz dual-matrix laminate with silicone hinge, unfolded and folded.

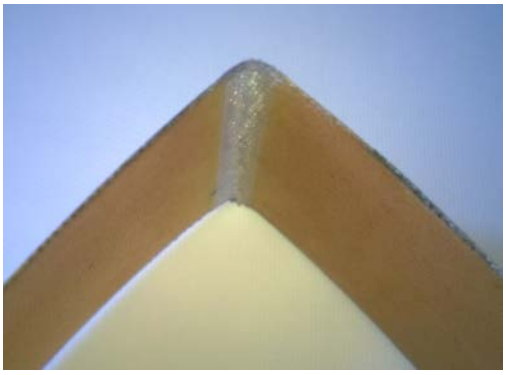

Figure 6.13: Compression side of the hinge folded at $\sim 90^o$.

6.4.1 Estimation of the shell mechanical properties

For woven composites, the in-plane properties can be calculated with good accuracy using CLT. However, this is not the case for the out-of-plane properties for one or two ply woven laminates. To address this problem, the periodic unit cell representing the weave can be homogenized through finite element models, see Ref. [36]. Soykasap found that CLT predictions are in agreement with more accurate finite element models when the laminates have three or more plies [59].

The shell composite analyzed here is made of six woven plies. Therefore, CLT will be used to estimate the mechanical properties. First, the orthotropic material stiffness of the lamina needs to be calculated. In the case of woven composites, studying the microstructure of the material to estimate the fiber volume fraction is not trivial, as the voids between warp and weft are filled with extra resin. For this reason, the dry fabric and the final composite were weighed in an Acculab® VI precision scale. As the densities of the phases are given by the manufacturer, the fiber volume

fraction is:

$$V_f = \frac{V_f}{V_f + V_m} = \frac{m_f/\rho_f}{m_f/\rho_f + m_m/\rho_m}, \tag{6.1}$$

where m and ρ and V are mass, density and volume, respectively. The subscripts m and f indicate matrix and fibers. The resulting volume fractions are:

$$V_f = 59\% \tag{6.2}$$

for the epoxy-Astroquartz laminate, and

$$V_f = 33\% \tag{6.3}$$

at the silicone embedded folds. The fiber volume fraction is lower at the hinges due to the absence of vacuum during the curing of the silicone.

The homogenized properties of the unidirectional yarn are obtained with the help of the following micromechanical models (Ref. [12]). The longitudinal modulus E_1 can be obtained from the rule of mixtures

$$E_1 = V_f E_f + (1 - V_f) E_m. \tag{6.4}$$

where E_f and E_m are the fibers and matrix Young's modulus, respectively.

The transverse modulus can be estimated with the Halpin-Tsai semiempirical relation

$$E_2 = \frac{E_m(1 + \xi\eta V_f)}{1 - \eta V_f}, \tag{6.5}$$

where

$$\eta = \frac{E_{2f} - E_m}{E_{2f} + \xi E_m}, \tag{6.6}$$

The parameter ξ can be obtained from experiments, and is usually assumed to be $\xi = 1$ for glass and carbon composites with high volume fractions.

The Poisson's ratio ν_{12} can also be obtained by the rule of mixtures

$$\nu_{12} = V_f \nu_{12f} + (1 - V_f)\nu_m. \tag{6.7}$$

Finally, to calculate the in-plane shear modulus, the Halpin-Tsai relation can be used:

$$G_{12} = \frac{Gm(1 + \xi\eta V_f}{1 - \eta V_f}, \tag{6.8}$$

where

$$\eta = \frac{G_{12f} - G_m}{G_{12f} + \xi G_m}, \tag{6.9}$$

and the best agreement with experimental results has been found for $\xi = 1$.

The Poisson's ratio values have been assumed $\nu_{12f} = 0.2$, $\nu_{epoxy} = 0.3$ and $\nu_{silicone} = 0.5$. Because all materials have been assumed isotropic, the shear modulus is

$$G = \frac{E}{2(1 + \nu)}. \tag{6.10}$$

The compliance matrix of the lamina, $\mathbf{S}$, is defined as

$$\begin{bmatrix} \epsilon_1 \\ \epsilon_2 \\ \gamma_6 \end{bmatrix} = \begin{bmatrix} S_{11} & S_{12} & 0 \\ S_{12} & S_{22} & 0 \\ 0 & 0 & S_{66} \end{bmatrix} \begin{bmatrix} \sigma_1 \\ \sigma_2 \\ \tau_6 \end{bmatrix}. \tag{6.11}$$

The components of S can be expressed in terms of the homogenized lamina properties

$$\begin{array}{rcl} S_{11} & = & \frac{1}{E_1} \\ S_{22} & = & \frac{1}{E_2} \\ S_{12} & = & S_{21} = -\frac{\nu_{12}}{E_1} \\ S_{66} & = & \frac{1}{G_{12}} \end{array}. \tag{6.12}$$

The lamina stiffness matrix is $Q = S^{-1}$. If the lamina axes $(1, 2)$ are rotated an angle θ with respect to the reference axes (x, y), the stiffness matrix with respect to the reference axes is

$$\begin{bmatrix} Q_{xx} & Q_{xy} & Q_{xs} \\ Q_{yx} & Q_{yy} & Q_{ys} \\ Q_{sx} & Q_{sy} & Q_{ss} \end{bmatrix} = [T]^{-1} \begin{bmatrix} Q_{11} & Q_{12} & 0 \\ Q_{12} & Q_{22} & 0 \\ 0 & 0 & Q_{66} \end{bmatrix} [T]^{-T}, \tag{6.13}$$

where T is transformation matrix

$$[T] = \begin{bmatrix} \cos^2(\theta) & \sin^2(\theta) & 2\cos(\theta)\sin(\theta) \\ \sin^2(\theta) & \cos^2(\theta) & 2\cos(\theta)\sin(\theta) \\ -\cos(\theta)\sin(\theta) & \cos(\theta)\sin(\theta) & \cos^2(\theta) - sin^2(\theta) \end{bmatrix}. \tag{6.14}$$

Classical lamination theory is used to predict the behavior of laminates composed of thin, orthotropic laminas. The behavior of a laminate is given by the ABD matrix

$$\begin{Bmatrix} N \\ \dots \\ M \end{Bmatrix} = \begin{bmatrix} A & \vdots & B \\ \dots & & \dots \\ B & \vdots & D \end{bmatrix} \begin{Bmatrix} \epsilon^0 \\ \dots \\ \kappa \end{Bmatrix}, \tag{6.15}$$

where N are the force resultants, M the moment resultants, ϵ^0 the midplane strains, and κ the midplane curvatures of the shell. A represents the extensional stiffness, B the in-plane/flexure bending stiffness, and D the bending stiffness. The ABD matrix can be found in terms of the lamina stiffness as

$$A_{ij} = \sum_{k=1}^{N} Q_{ij}^k (z_{k+1} - z_k) \tag{6.16}$$

$$B_{ij} = \sum_{k=1}^{N} \frac{1}{2} Q_{ij}^k (z_{k+1}^2 - z_k^2) \tag{6.17}$$

$$C_{ij} = \sum_{k=1}^{N} \frac{1}{3} Q_{ij}^k (z_{k+1}^3 - z_k^3), \tag{6.18}$$

where z_k is the position of the laminate k with respect to the mid-plane.

If the warp and weft directions are considered to be unidirectional laminas in a plain weave composite, the in-plane properties can be approximated well with CLT, but the out-of-plane information is lost.

Soykasap proposed a mosaic model that assumed that each plain weave lamina was divided into subcells occupied by infiltrated yarns [59]. A unit cell of a single plain weave lamina is represented by a 4 x 4 mosaic model. Each unit cell consists of asymmetrical cross-ply laminates, ignoring the continuity and undulation of the fibers. Comparison with finite element models showed that this model is a good approximation for plain weave laminates with three plies or more.

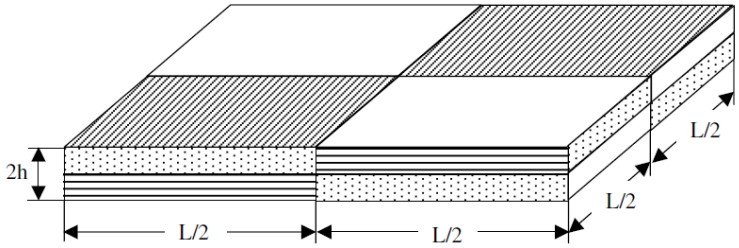

Figure 6.14: Unit cell of the mosaic model, taken from Soykasap [59].

With this model, the 6-ply plain weave laminate can be calculated as if it were composed of 12 laminas, each of which has a stiffness of

$$Q = 0.5 * (Q_{\parallel} + Q_{\perp}). \tag{6.19}$$

For example, the first lamina is a plain weave with one of the fiber directions at an angle $\alpha = 30^o$ from the reference axis. The first and second equivalent unidirectional laminas would have an effective stiffness

$$Q = 0.5 * (Q_{30} + Q_{-60}). \tag{6.20}$$

This model has been used to calculate the extensional and bending stiffness matrix of the AQ-reinforced epoxy and the AQ-reinforced silicone. $B = 0$ due to the symmetry of the laminate. The thickness was measured $t = 0.35$ mm for the epoxy and $t = 0.5$ mm for the silicone.

$$A_{AQ,epoxy} = \begin{bmatrix} 8828 & 2542 & 0 \\ 2542 & 8828 & 0 \\ 0 & 0 & 3143 \end{bmatrix} \text{N/mm}, \tag{6.21}$$

$$D_{AQ,epoxy} = \begin{bmatrix} 93 & 36.7 & 6.7 \\ 36.7 & 93 & -6.7 \\ 6.7 & 6.7 & 43.6 \end{bmatrix} \text{Nmm}, \tag{6.22}$$

$$A_{AQ,silicone} = \begin{bmatrix} 4457 & 1486 & 0 \\ 1486 & 4457 & 0 \\ 0 & 0 & 1485 \end{bmatrix} \text{N/mm}, \tag{6.23}$$

$$D_{AQ,silicone} = \begin{bmatrix} 79.1 & 44.7 & 11.9 \\ 44.7 & 79.13 & -11.9 \\ 11.9 & 6.7 & 44.7 \end{bmatrix} \text{ Nmm.} \tag{6.24}$$

The behavior of the shell is isotropic and fiber-dominated. The in-plane stiffness of the silicone laminate is about one half the stiffness the epoxy laminate, while the out-of-plane stiffness of the silicone laminate is comparable to the out-of-plane stiffness of the epoxy laminate. This is due to the greater thickness of the silicone laminate.

The out-of-plane stiffness was measured with four-point bending experiments. The estimated ABD matrix will be used in Chapter 7 to model a dual-matrix composite structure with the same laminate configuration.

6.4.2 Experimental characterization of the fold

The most probable source of error of the analytical model of the composite is the out-of-plane stiffness. To validate the results, bending tests were performed in full epoxy-cured laminates. Bending tests on laminates with a central silicone hinge (Figure 6.13) were carried out as well. The samples were fabricated in the laboratory with the characteristics of the laminate studied in the previous section.

The experimental setup was the same as in the four-point bending tests described in Chapter 3, shown in Figures 3.12 and 3.13. In these experiments, $h = s = 25$ mm. The geometry of the hinges is shown in Figure 6.17. The full epoxy laminates are similar to the sample shown in Figures 6.13 and 6.15, but without a hinge region. The vertical deflection of the center of the samples was measured with a laser extensometer. The load was measured with a 50 N load cell in the Instron 5569.

Figure 6.16 shows the dependence of the moment with the bending curvature of the shell. The stiff epoxy-cured samples bent elastically, and the linear slope of the plots can be fitted to obtain the out-of-plane stiffness $D_{11} = D_{22}$. The initial nonlinearity of the plots is thought to be a result of fiber misalignment, which caused stiffness coupling ($B \neq 0$). The stiffness coupling causes some initial out-of-flatness on some samples, which can justify the initial non-linearity in the plot.

The average of the linear regions of the plot gives a $D_{11} \approx 110$ Nmm, which is in relatively good agreement with the prediction $D_{11} = 93$ Nmm. To calculate the bending component, the width of

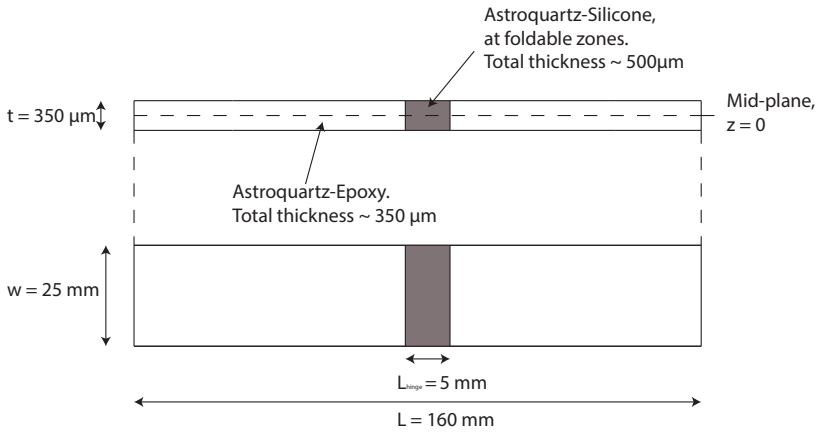

Figure 6.15: Schematics of the hinge samples manufactured in the laboratory. The laminate is the $[\pm 30, 0]_s$ plain weave laminate studied in the previous section, cured with silicone matrix in the hinge area (in grey), and with epoxy in the rest of the sample.

the sample, $w = 25$ mm, was used. The out-of-plane behavior is very sensitive to the thickness of the composite, i.e., small variations in the thickness of the laminate can cause large variations on the out-of-plane stiffness.

Finally, four-point bending tests was performed on the hinge samples (Figure 6.15). Figure 6.18 shows the comparison of the behavior of an epoxy laminate sample, a hinge sample before being folded, and the same sample after being folded. Figure 6.13 is an example of a folded hinge.

Before being folded, the hinge samples have a stiffness $D_{11} \approx 98$ Nm, higher than the predicted $D_{11} = 79$ Nm. This shows that the behavior of the laminate is fiber-dominated. The hinge was then folded 180^o. The fold was done manually, obtaining a curvature radius at the fold of ~ 2 mm. After being folded, the hinge clearly showed a decrease in bending stiffness. The initial stiffness, i.e., before the moment reaches 5 Nmm, is the same as the prefolded sample. For moments higher than that value, the hinge starts softening until it reaches a new linear behavior, with tangent stiffness of ~ 9 Nmm. The behavior also presents some hysteresis.

The moment at which the stiffness of the hinge starts decreasing is believed to be the onset of microbuckling in one of the laminas. After that moment, and for higher values of bending curvature,

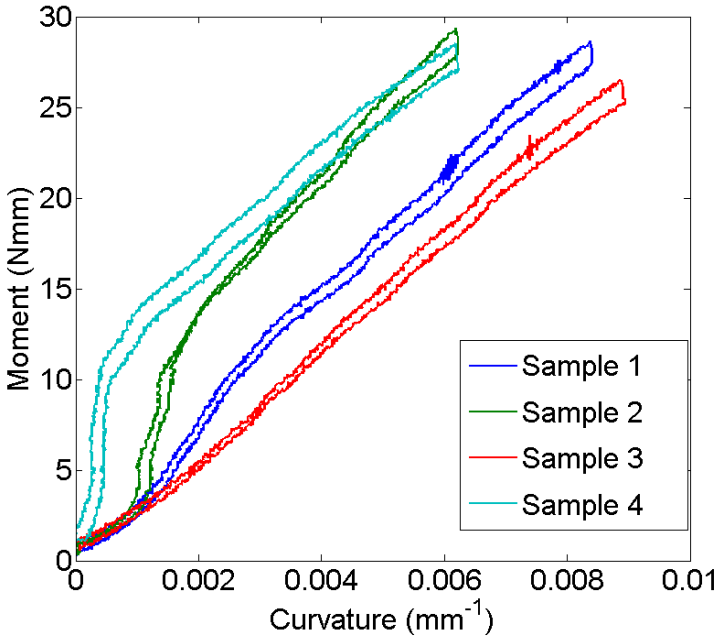

Figure 6.16: Bending tests of AQ-epoxy samples.

a post-microbuckling behavior is observed. Small residual waviness of the fiber was observed after folding and releasing the hinge. Effects such as the interaction of the microbuckled fibers with the rest of the fibers in the plain weave, and the interaction of those fibers with the rest of the laminate, should be studied in detail to ensure a better understanding of the bending and stiffness degradation behavior of the hinge.

The reduction of the hinge stiffness measured in this chapter will be taken into consideration in Chapter 7 for a preliminary analysis as an approximation of the out-of-plane behavior of the hinge lines in a foldable structure.

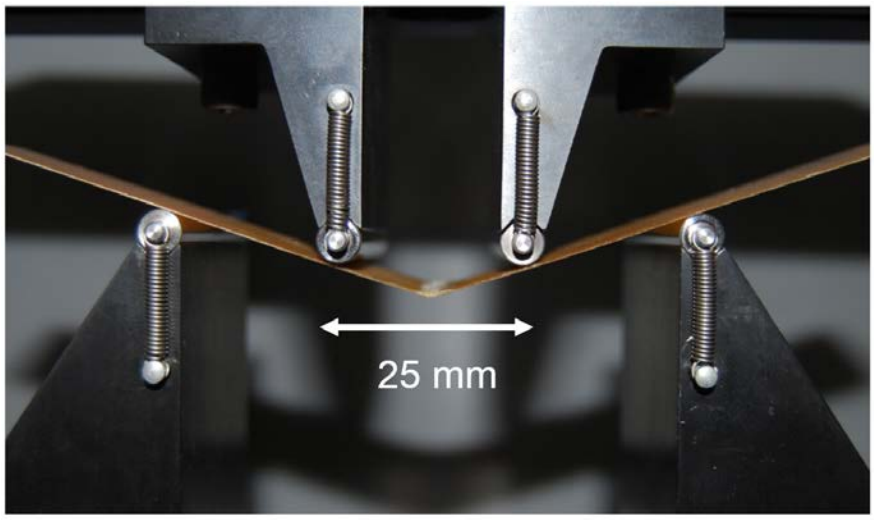

Figure 6.17: Four-point bending test setup.

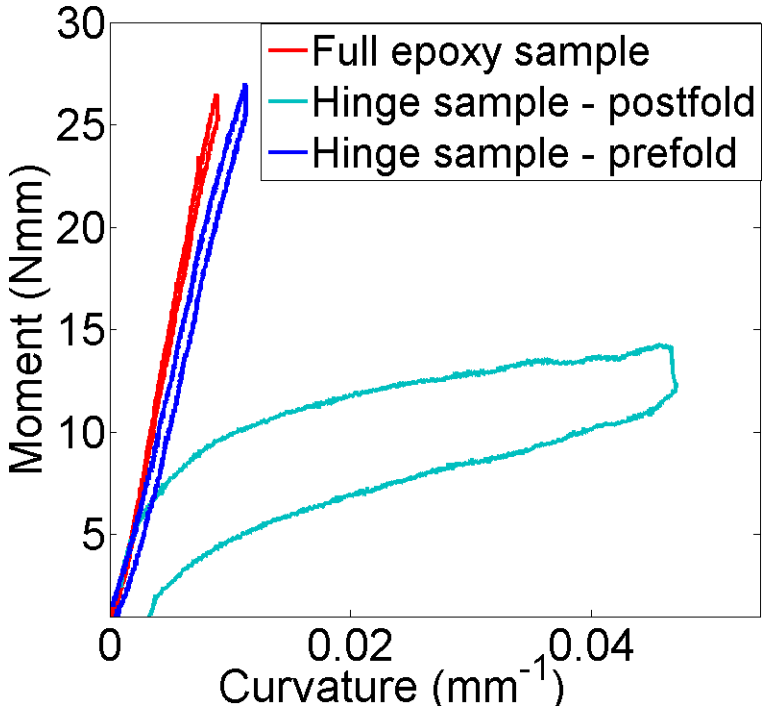

Figure 6.18: Bending tests of one AQ-epoxy sample and one hinge sample, before and after being manually folded.

Chapter 7

Deployable antenna concept for CubeSat applications

CubeSats are miniaturized satellites that are defined by the standard unit 1U of 10 x 10 x 10 cm. CubeSats can stack along one axis to form 2U, 3U, or 6U configurations. CubeSats originated in 1999 from a multi-university program developed at California Polytechnic State University and Stanford University with the purpose of helping universities worlwide to perform research in space science and exploration. Small companies and government organizations have also benefited from this technology.

The tightly constrained volume available in a CubeSat limits the capabilities of the payloads and the performance of subsystems such as power and communications. The predominant choice for a communications system in CubeSats are dipole or monopole antennas. These types of antennae are easy to stow in a CubeSat and commercially available, but tend to be limited by low efficiency and low gain. To improve bandwidth and efficiency, it is desirable to utilize antenna designs that currently are only present on large satellites, due to their greater size and complexity.

The size of an antenna is inversely proportional to its frequency, which makes packaging a high-gain and high-frequency antenna into a CubeSat challenging. Olson et al. [47] proposed several concepts for deployable wideband antennas compatible with CubeSats and operating in the 250-500 MHz range, covering part of both the Very High Frequency (VHF) and Ultra High Frequency bands (UHF), and with circular polarization. The design of these concepts allows them to be stowed in small compaction ratios, through structures such as pantographs or foldable shells.

One of these concepts was a conical log spiral antenna with a thin conductor attached to or embedded in a conical foldable shell. Patented by Dyson in 1958, conical log spirals provide wide-

band, broad-lobed unidirectional circularly polarized radiation in the direction of the cone's tip (Figure 7.1).

Figure 7.1: Conical log spiral antenna, taken from Dyson [18].

The concept was based on the flattening and folding of the shell and the folding of the shell in the flattened configuration into a Miura-ori pattern 7.2. The design presented in Figure 6.10 portrays the implementation of this concept for a structure supporting a quadrifilar helix antenna.

This chapter presents the use of the dual-matrix manufacturing technique and the material model for the quasi-isotropic laminate from Chapter 6 in designing the structure supporting a conical log spiral antenna.

This research is still ongoing, and is done with the support of AFOSR and in collaboration with Prof. Joseph's Constantine's group at California State University, Fullerton, which conducts the antenna design.

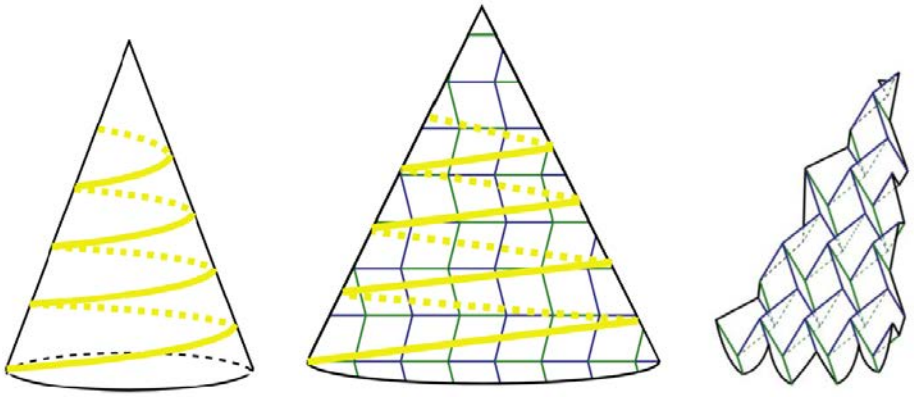

Figure 7.2: Miura-ori foldable conical log spiral antenna, proposed in Olson et al. [47].

7.1 Design parameters

For a conical log spiral antenna, the spiral dimensions vary in a log-periodic manner, and the radiation is directed outside of the smallest element. Designs performed by Prof. Constantine show two conical log spirals, see Figure 7.3, and operate at the desired band (250-500 MHz).

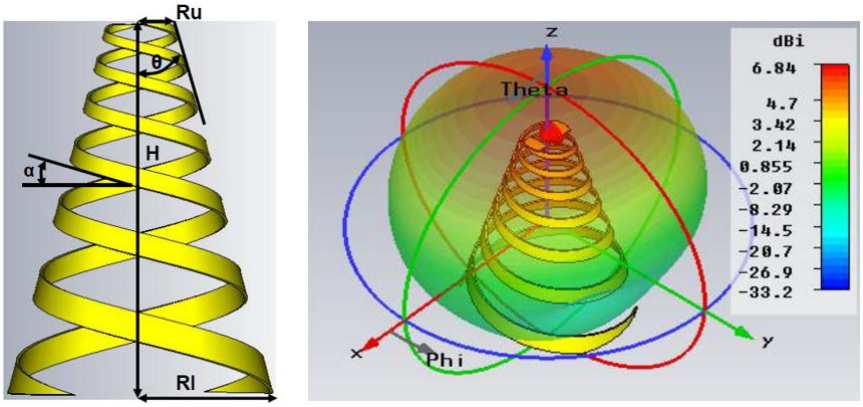

Figure 7.3: Conical log spiral antenna design and 3-D radiation pattern at 250 MHz. Courtesy of Prof. Joseph Constantine.

The conical log spirals are made of a conductor whose thickness must be larger than the skin depth of the conductor material. At high frequencies, the AC current flows mostly between the outer surface and a depth inside a conductor called the skin depth. Precisely, the skin depth is defined as the distance a wave travels in a lossy medium to reduce its value by 36.8%.

The conductor material and thickness depend on the skin depth at the minimum operating frequency (250 MHz), as the skin depth is inversely proportional to the frequency f. The skin

depth δ also depends on the conductor resistivity and relative permeability, ρ and μ_R, respectively:

$$\delta = \sqrt{\frac{\rho}{\pi f \mu_0 \mu_R}}, \tag{7.1}$$

where $\mu_0 = 4\pi \cdot 10^{-7}$ Vs/Am is the vacuum permeability.

The volume available in the CubeSat and the geometry of the antenna need to be considered to design the packaging scheme. The CubeSat stowage requirement allows the antenna to be packaged in a space no larger than 20 x 10 x 5 cm. The conical antenna geometries proposed here are based on preliminary designs of the conical log spiral.

- **Antenna 1**: The first design is a truncated cone with base radius $R_b = 21$ cm, top radius $R_t = 10$ cm, and height $h = 15$ cm. The dimensions have been chosen so that the length of the generator of the cone, $L_g = 19$ cm, is smaller than the longer dimension of the CubeSat (20 cm).

- **Antenna 2**: The second design is a larger truncated cone with base radius $R_b = 23$ cm, top radius $R_t = 5$ cm, and height $h = 15$ cm.

Figure 7.4 compares the size of the cones with the size of the 2U CubeSat.

7.2 Approach

A dual-matrix Astroquartz shell composite has been chosen to support the conductors that form the antenna, with the plain weave laminate $[\pm 30, 0]_s$ that was studied in Chapter 6. In this section, the integration conductor-shell and the packaging schemes chosen to stow the antenna into the available space are described.

7.2.1 Conductor

The conductor needs to be thin to minimize its effect on the folding capabilities of the dual-matrix shell. Additionally, the thickness needs to be $t \geq 2\delta$, where δ is the skin depth of the metal.

Beryllium copper is a copper alloy with 0.5-3 % beryllium that exhibits high strength and good conductivity. Thin beryllium copper sheets can reach high curvatures, but may break when folded

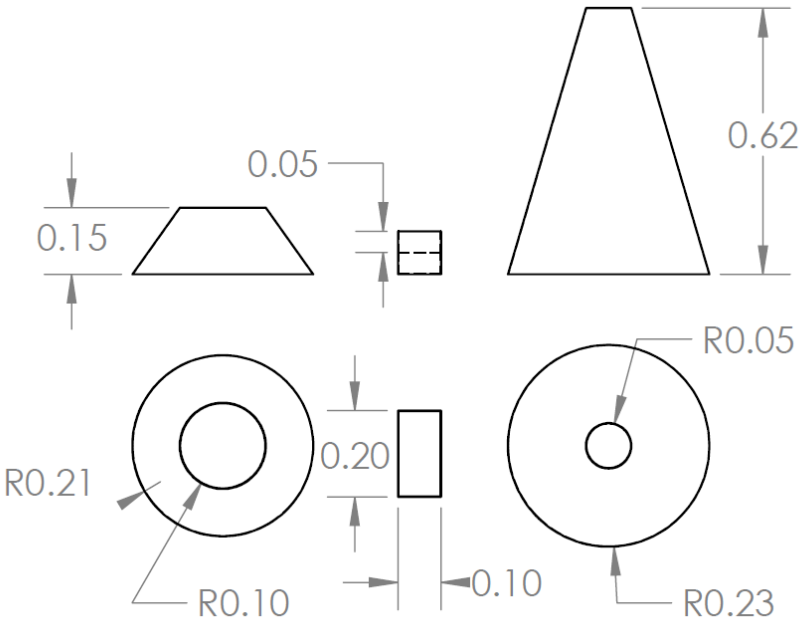

Figure 7.4: Front and top view of the cones and the 2U CubeSat. The cone dimensions compared with the volume available in the cubesat (20 x 10 x 5 cm). Units are in meters.

into sharp kinks. Another option may be printing the metallic conductor on the laminate, during or after the fabrication of the laminate. Conductive metallic tapes may be used as well.

The conductor used here is a phosphor bronze woven mesh from TPW Inc., with 325 wires per inch and a wire diameter of 28 μm. Phosphor bronze is an alloy with 94.8% copper, 5% tin and 0.2% phosphorous. This material has good physical properties, fair electrical conductivity and moderate cost. The skin depth of bronze at 250 MHz is $\delta \sim 6$ μm. The wire diameter is larger than δ, potentially making this material suitable for the antenna application.

The mesh can be folded into very sharp kinks, and it shows a distortion when fold that the filaments maximum strain does not reach the ultimate strain and the mesh does not break. The low stiffness of the mesh minimizes the effect on the folding capabilities of the laminate. Additionally, the conductivity is not affected by folding. Slabs of this material that were previously folded were tested in Prof. Constantine's laboratory, showing good radiation behavior.

The conductor is integrated in the dual-matrix shell by embedding it in the laminate mid-plane. The mesh allows the UV light to penetrate enough so that the silicone is well cured through the thickness of the laminate. Figure 7.6 shows schematically how the conductor is embedded on the

composite.

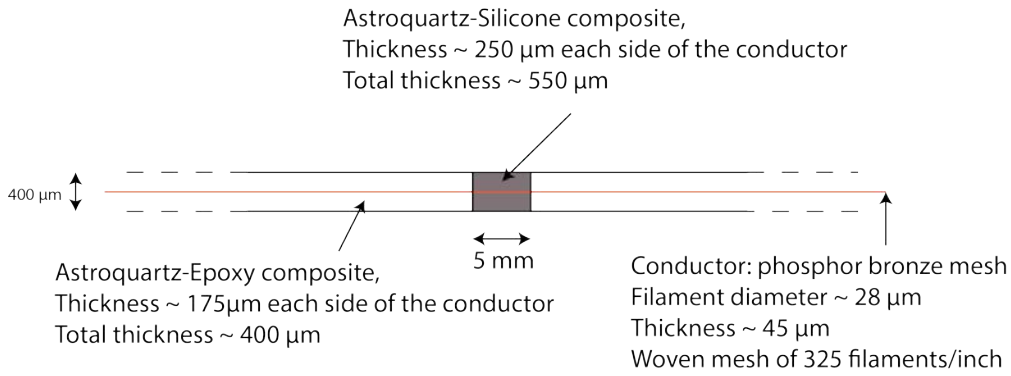

Figure 7.5: Thickness view of the composite shell with hinge and conductor.

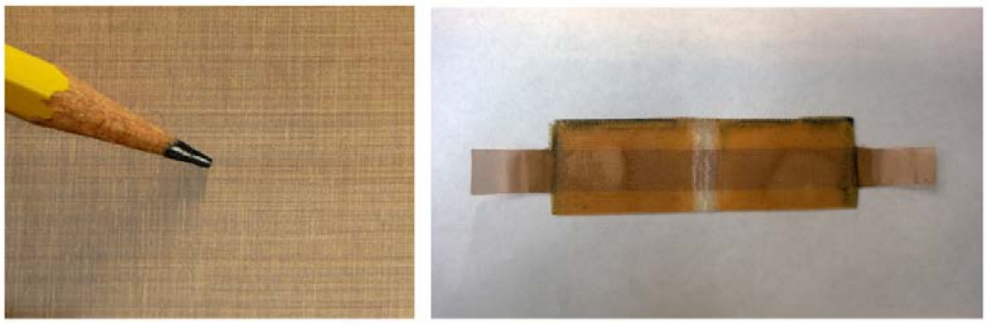

Figure 7.6: Phosphor bronze conductive mesh (left) and conductor embedded in the dual-matrix laminate (right).

7.2.2 Packaging schemes

- Antenna 1: The length of the generator of the truncated cone is $L_g = 19$ cm, which is smaller than the longer dimension of the available space in the CubeSat. Therefore, the packaging may be achieved by flattening the cone and z-folding the flattened shell into trapezoidal panels with length equal to the generator of the cone and width smaller than 10 cm. Figure 7.7 shows the packaging scheme.

  The number of stiff panels on the shell must be even so that the cone can be flattened, and the creases must be meridional to the cone. The minimum number of equally spaced folds that allow the folded configuration to fit in the CubeSat is 14, with a minimum thickness

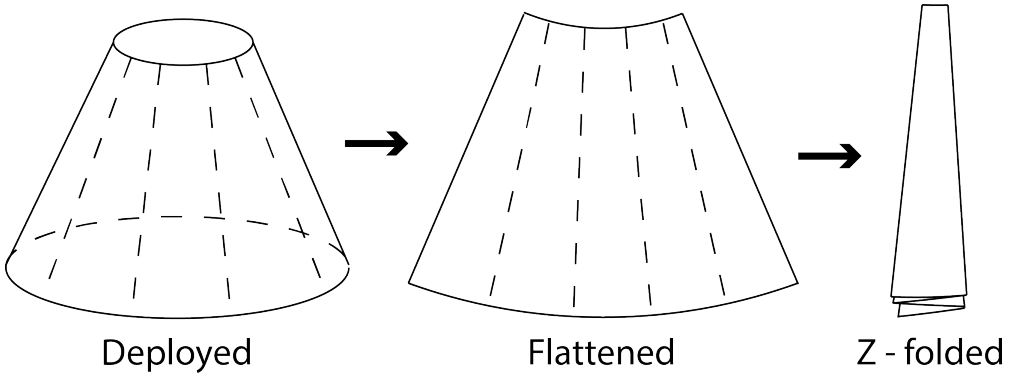

Figure 7.7: Packaging scheme for Antenna 1.

of the resulting folded shell of 7 mm. The design presented below contains 18 folds, with a crease line at every 20^o.

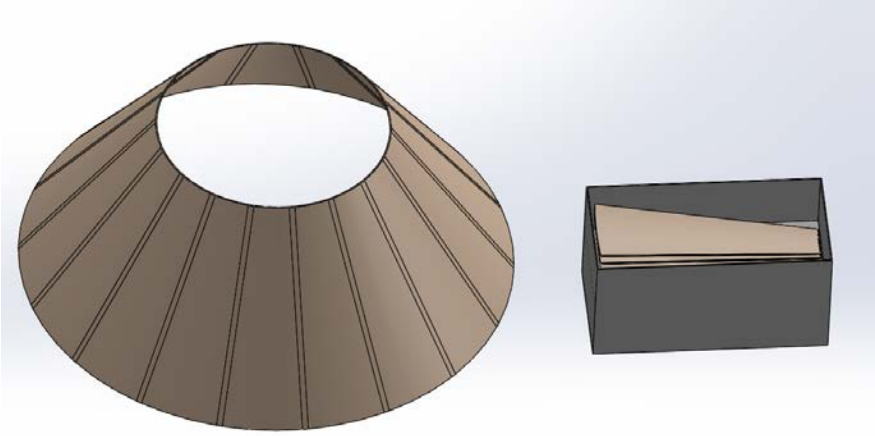

Figure 7.8: Representation of the deployed conical shell with 18 crease lines, and folded shell inside the CubeSat.

- Antenna 2: the larger dimensions of this shell require a packaging scheme similar to the one proposed by Olson et al. (Figure 7.2), which used a Miura-ori pattern. The approach taken here is a modification of the regular Miura-ori pattern, in which the straight crease lines of the regular Miura pattern form a polar configuration. This pattern, called a tapered Miura-ori, is rigid-foldable, i.e., the folding scheme allows continuous motion without the need for twisting or stretching the panels between the creases.

  The geometry was described by Gattas et al. [22]. The pattern can be described by the basic unit, which is formed by four adjacent panels, whose radial lines meet at a common center

point (Figure 7.9). The angle ρ between the polar lines is constant. Panels that are at the same distance from the center are identical in size, and the panel side length increases for each radial ring j.

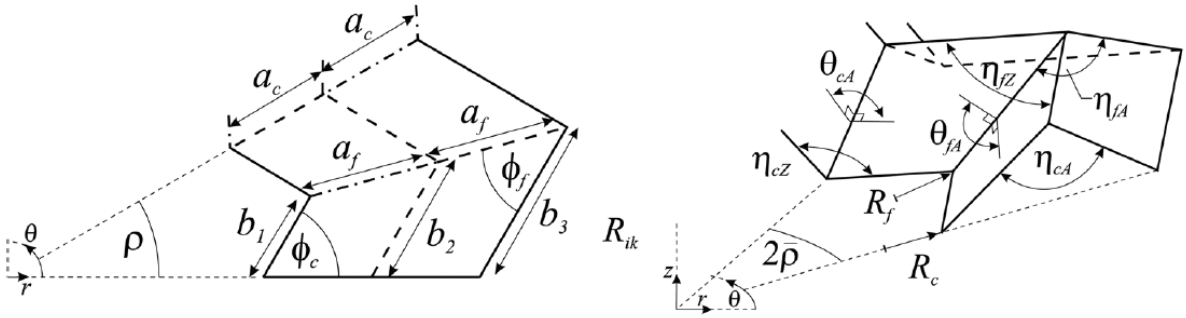

Figure 7.9: Tapered Miura-ori: crease pattern (flat configuration) and partially folded configuration. Taken from Gattas et al. [22].

From the flat configuration in Figure 7.9, the pattern can be defined by the following equations

$$\phi_f = \phi_c - \rho \tag{7.2}$$

$$a_c = a_f \sin\phi_f / \sin\phi_c \tag{7.3}$$

$$b_j = b_1 + (j-1)a_c \sin\rho / \sin\phi_f, \tag{7.4}$$

where j indicates the corresponding radial ring, and $j = 1$ for the panel closest to the center. The dihedral and edge angles can be determined from the folded configuration in 7.9, with

$$\cos\eta_{cZ} = \sin^2\phi_c \cos\theta_{cA} + \cos^2\phi_c \tag{7.5}$$

$$\cos\eta_{cA} = \sin^2\phi_c \cos\theta_Z - \cos^2\phi_c \tag{7.6}$$

$$(1+\cos\eta_{cZ})(1-\cos\eta_{cA}) = 4\cos^2\phi_c \tag{7.7}$$

$$\cos\eta_{fZ} = \sin^2\phi_f \cos\theta_{fA} + \cos^2\phi_f \tag{7.8}$$

$$cos\eta_{fA} = sin^2\phi_f \cos\theta_Z - \cos^2\phi_f \tag{7.9}$$

$$(1+\cos\eta_{fZ})(1-\cos\eta_{fA}) = 4\cos^2\phi_f. \tag{7.10}$$

The fold can be parameterized using the folded angular parameter and the smaller and larger radius of the panel vertex

$$\bar{\rho} = (\eta_{cZ} - \eta_{fZ})/2 \tag{7.11}$$

$$R_{cj} = b_j \sin(\eta_{fz}/2)/\sin\bar{\rho} \tag{7.12}$$

$$R_{fj} = b_j(\pi - \sin(\eta_{cz}/2)/\sin\bar{\rho}. \tag{7.13}$$

These nine equations define ten variables in the folded configuration, so the folding has only one degree of freedom. Therefore, the geometry pattern can be defined with 6 parameters, and any folded configuration can be defined with a single configuration variable.

This pattern can be applied to a flattened cone, as shown in Figure 7.10. The Miura-ori radial folds are the same meridional folds along the generator of the cone, which are also used for flattening. Therefore, the final pattern is independent on the crease lines that allow the cone to be flattened.

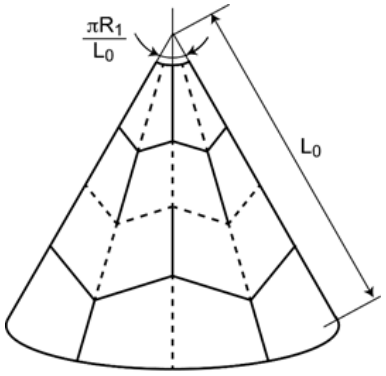

Figure 7.10: Flattened cone with a tapered Miura-ori pattern.

The parameters that define the geometry are the angle between generators of the flattened cone, $\theta = \pi R_1/L_0$, where L_0 is the length of the truncated generator and R_1 is the radius of the top of the truncated cone. If the dimensions of the Antenna 2 design are considered, $\theta = 50.9^o$, and $L_0 = 64.3$ cm.

The number of trapezoidal panels in the azimuthal and radial direction, m and n respectively,

can determine two other parameters of the pattern from θ and L_0:

$$\rho = \frac{\theta}{m} \tag{7.14}$$

$$a_f = \frac{L_0}{n}, \tag{7.15}$$

to fit the pattern to the geometry of the flattened cone. The other two parameters to consider are the angle of the azimuthal creases with respect to the radial ones, ϕ_A, and the azimuthal length of the first panel,

$$b_1 = r_1 sin\rho / sin\phi_c, \tag{7.16}$$

where r_1 is given by the distance of the closest end of the radial lines to their common center, also given by the geometry of the flattened cone. Therefore, 3 parameters of the pattern are given by the geometry, and the other 3 need to be chosen so that the folded configuration fits inside the 2U CubeSat.

The width of the final folded configuration depends directly on a_f, and therefore a minimum number of panels in the radial direction, n, has to be chosen so that the final width is less than 10 cm. For the geometry in consideration, $n = 8$ is the minimum number of panels. The maximum length of a panel is equal to half the perimeter of the base of the cone divided by the number of azimuthal panels, m. This results in a minimum m of 4 so that the panels fit in the 20 x 10 area of the CubeSat.

The folding initial, intermediate, and final configurations have been calculated using the equations above with the help of Gattas' MATLAB Miura-ori toolbox [28]. To reduce the number of panels in the pattern, the minimum number $m = 4$ and $n = 8$ has been considered. This gives a total number of panels equal to 32. The total thickness is therefore $t = 2mnt_{panel} \sim 2.4$ cm, therefore fitting inside the 5 cm CubeSat depth.

The solution of the problem is a final folded configuration with a length $L = 19.32$ cm and a width $w = 7.8$ cm, obtaining a compaction ratio of $\sim 72 : 1$.

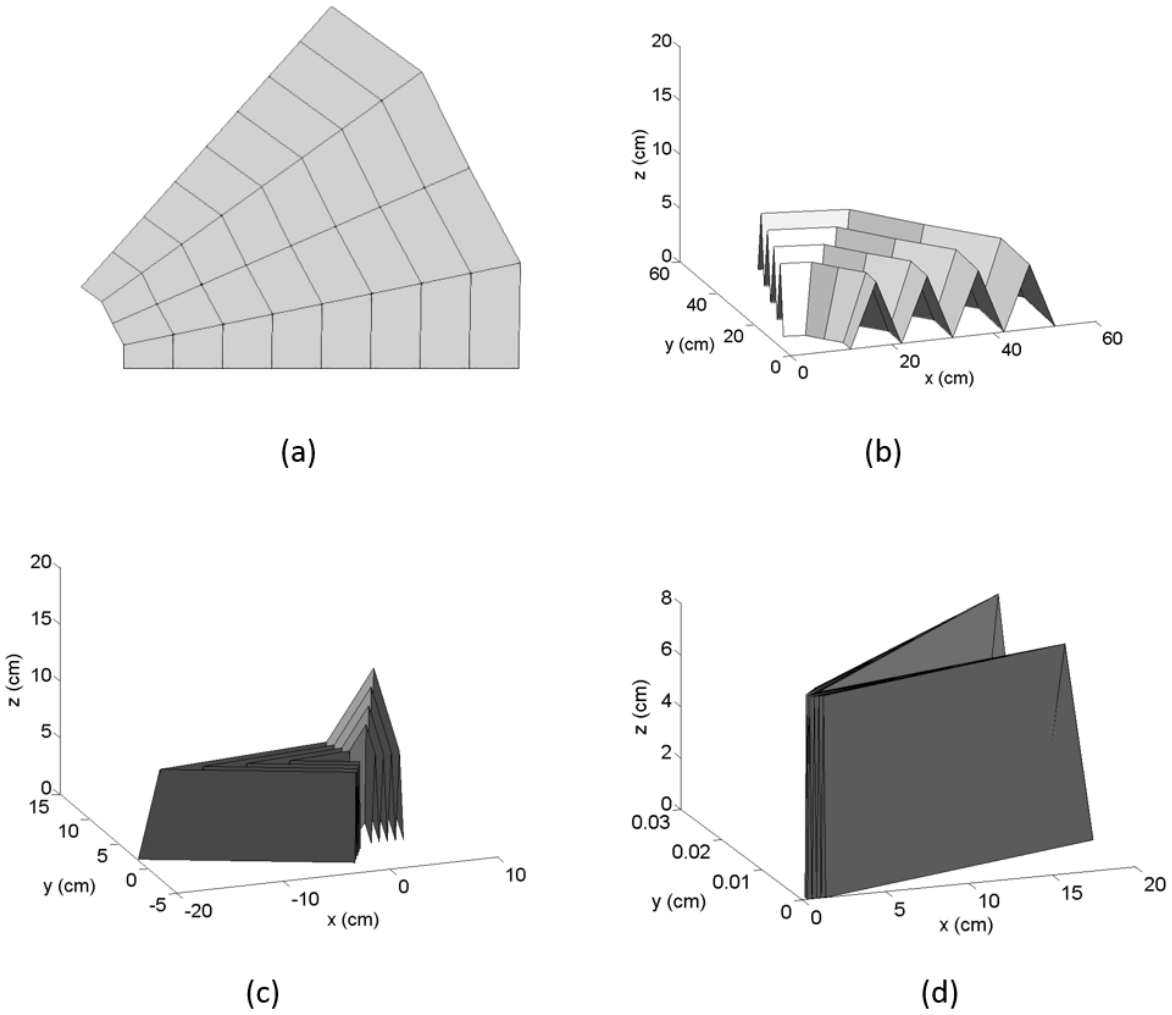

Figure 7.11: Solution of the tapered Miura-ori calculated in MATLAB. a) Folding pattern. b) Configuration for $\theta_{cA} = 177^o$. c) Configuration for $\theta_{cA} = 164^o$. d) Configuration for $\theta_{cA} \sim 0^o$ (fully folded).

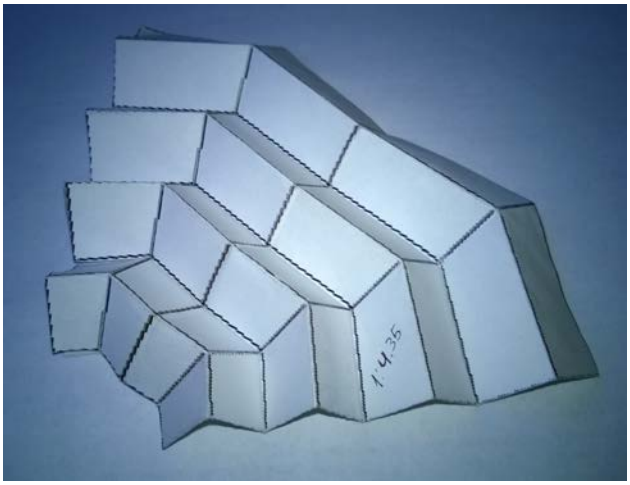

Figure 7.12: Paper model of the tapered Miura-ori pattern. Scale is 1:4.35 with respect to the actual antenna geometry.

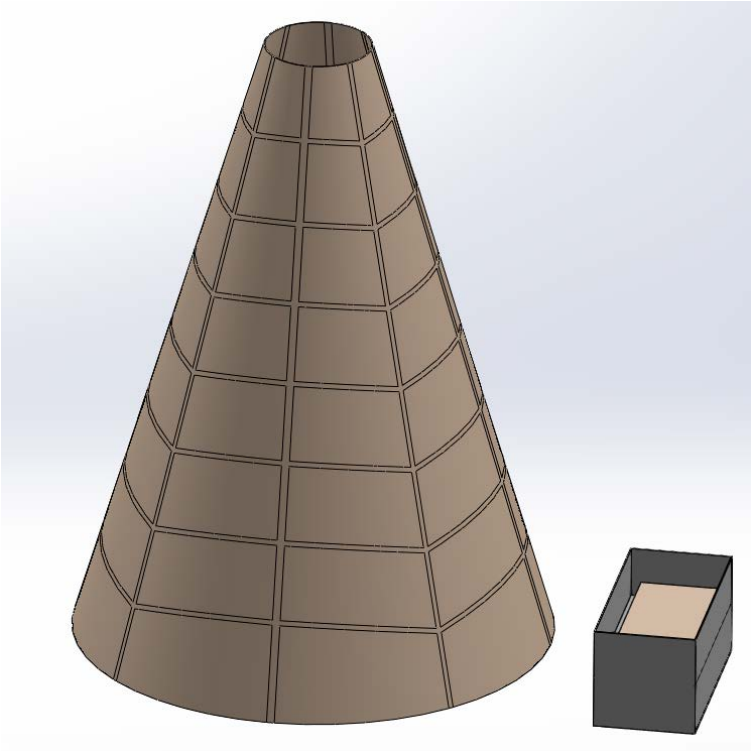

Figure 7.13: Representation of the deployed tapered-Miura ori shell, and folded configuration inside the CubeSat.

7.2.3 Attachment to the CubeSat bus

There are still plenty of design choices to be made with respect to the attachment of the antenna to the CubeSat bus, including the distance and relative position of the antenna with respect to the bus, feeding point, existence of a ground plane, etc.

For the simulations described in the next section, the antenna is assumed to be attached to the bus by six pin-jointed rods that eliminate the six rigid solid degrees of freedom. In the models, three points of the base of the antenna are connected to three points in the bus. The connections are such that two rods connect each point of the antenna to two different points in the bus. The rods need to be stowed inside the 2U CubeSat, so they may be telescopic, hinged, or simply tubes with internal springs, such as the ones found in "push-up" toys [5]. The base of the antenna is assumed to be parallel to the bus and at a distance of 10 cm. This configuration is similar for both antennas, see Figure 7.14.

Figure 7.14: Representation of the pin-jointed rod connections of the conical shell.

7.3 Frequency analysis of the system

One of the first steps of a structural design is to investigate the natural frequencies of the structure to ensure that the natural modes of vibration are away from environmental forcing frequencies.

The natural frequencies have been calculated for both antenna configurations using ABAQUS/Standard with boundary conditions that simulate the pin-jointed connections between the antenna and the

bus. The simulations have been performed without loading.

The material model used is the one calculated in Chapter 6 for the $[\pm 30/0]_s$ laminate. The stiff panels are made of the Astroquartz/epoxy laminate (Equations (6.21) and (6.22)), and the crease lines are made of the Astroquartz/silicone laminate (Equations (6.23) and (6.24)). However, if the antenna is assumed to have been folded and deployed, the out-of-plane stiffness is reduced. This reduction is considered here, although the experiments showed a initial linear behavior of the after-fold hinge that matched the linear behavior of the stiff laminate. In this model, the out-of-plane bending stiffness D is 10% of the pre-folded stiffness, using a similar value to the stiffness found in the experiments. As a limit case, a bending stiffness of 1% of the pre-folded stiffness has been analyzed. The effect of the conductor has not been taken into account for this analysis.

7.3.1 Model description

The model is formed with quadrilateral shell elements with reduced integration S4R. The mesh size is ~ 5 mm in most of the model, except through the crease lines, where a size of ~ 1 mm is used. The number of elements used for the model of the wide antenna design was 46000, while for the long design it was 98000 elements.

The linear material model was implemented through the ABAQUS command *SHELL GENERAL SECTION. The boundary conditions were chosen such that three pairs of dummy nodes (each pair representing one point in the CubeSat bus) are connected to three pairs of nodes at the base of the shell with pin-jointed rods. The pin-jointed rods were assumed to be rigid and were implemented using the multi-point constraint *MPC, PIN.

The eigenfrequencies were obtained with the ABAQUS perturbation analysis module. A total of 10 natural frequencies and modes were obtained for both antenna designs.

7.3.2 Analysis and results

Table 7.1 summarizes the results of the eigenfrequency simulations. The frequencies shown are the first, second and third eigenfrequencies for both designs. Results are given for a crease out-of-plane stiffness of 10% and 1% of the original, $D_{creases} = 0.1 D_{AQ,silicone}$ or $D_{creases} = 0.01 D_{AQ,silicone}$.

Both antennas seem to have a higher natural frequency than the commonly required $f \sim 1$ Hz. With the crease material model at a 10% out-of-plane stiffness of the pre-fold stiffness, which agrees

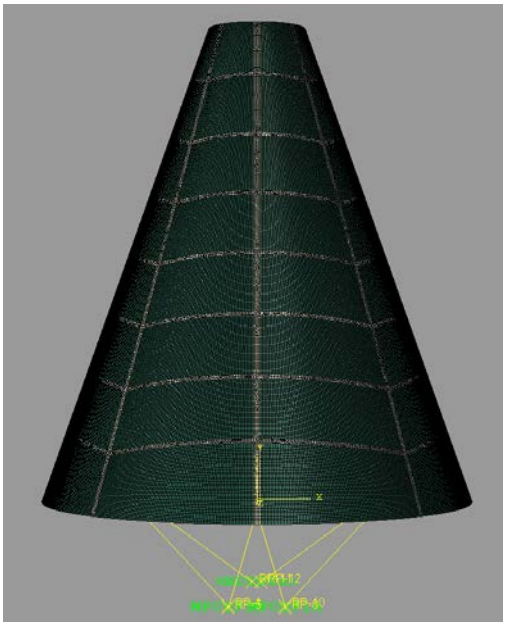

Figure 7.15: ABAQUS model of the dual-matrix conical shell with pin-jointed rod connections.

Shell	f_1 (Hz)	f_2 (Hz)	f_3 (Hz)
Antenna 1, 10% stiffness	6.15	7.13	12.1
Antenna 1, 1% stiffness	3.02	3.61	6.83
Antenna 2, 10% stiffness	7.81	8.46	15.4
Antenna 2, 1% stiffness	4.22	4.47	8.54

Table 7.1: Three first natural frequencies of the conical shells, for different values of the out-of-plane stiffness of the creases.

with the bending experiments on the hinge, frequencies of 6.15 and 7.81 Hz are obtained. With a ten-fold reduction of stiffness the natural frequencies are reduced by half, and are still above the usual frequency requirements.

The taller antenna has a higher natural frequency due to the smaller number of creases along the generators of the cone. The mode shapes indicate that there is no visible influence of the horizontal creases. The reduction of stiffness only causes sharp kinks in the mode shapes, except for the Antenna 1 third mode, in which the shape changes completely.

7.4 Fabrication of a prototype

A prototype of the Miura-ori foldable cone shell was manufactured in the laboratory. The geometry of the folding pattern is more simple than the design above. The prototype was constructed with the SAKASE fiberglass triaxial weave, so panels of plain weave carbon fiber were added to the laminate to add stiffness and shape instability. The folded shell was capable of deploying autonomously when released. Figure 7.18 shows the conical shell deployed, stowed, and folded in intermediate configurations.

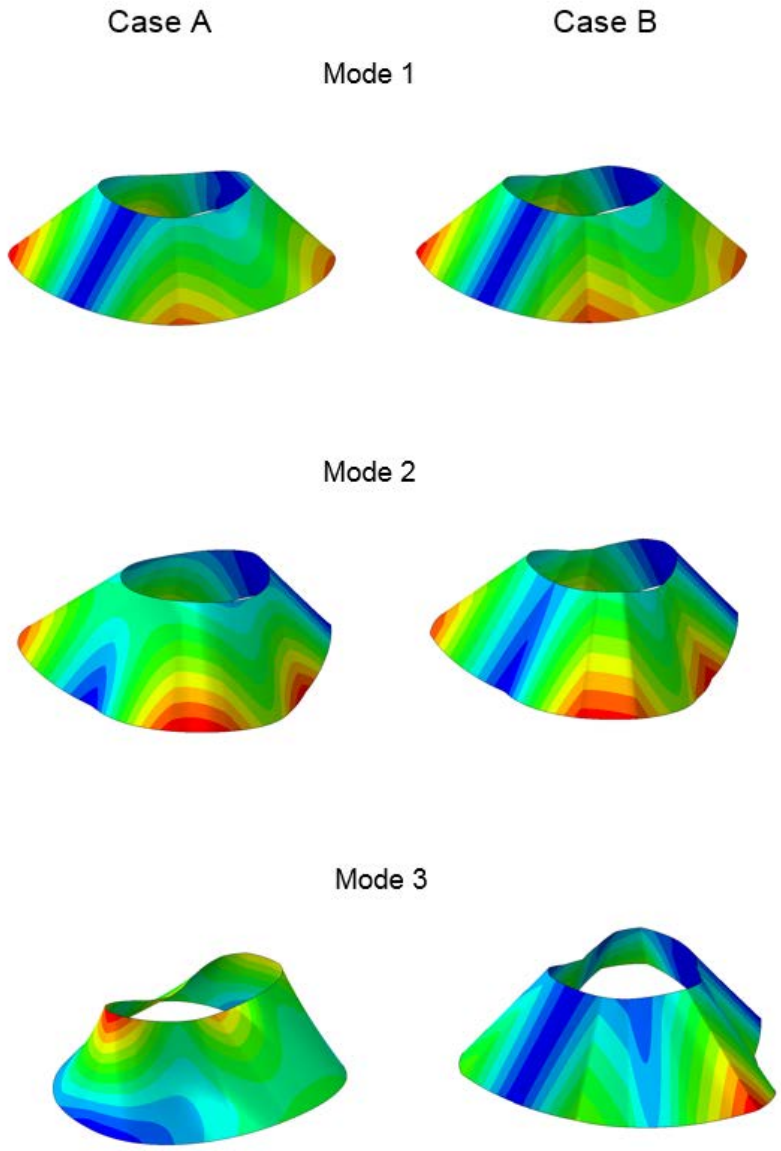

Figure 7.16: Mode shapes for the 3 first natural frequencies in the Antenna 1. For Case A, $D_{creases} = 0.1D_{AQ,silicone}$, and for Case B,$D_{creases} = 0.1D_{AQ,silicone}$.

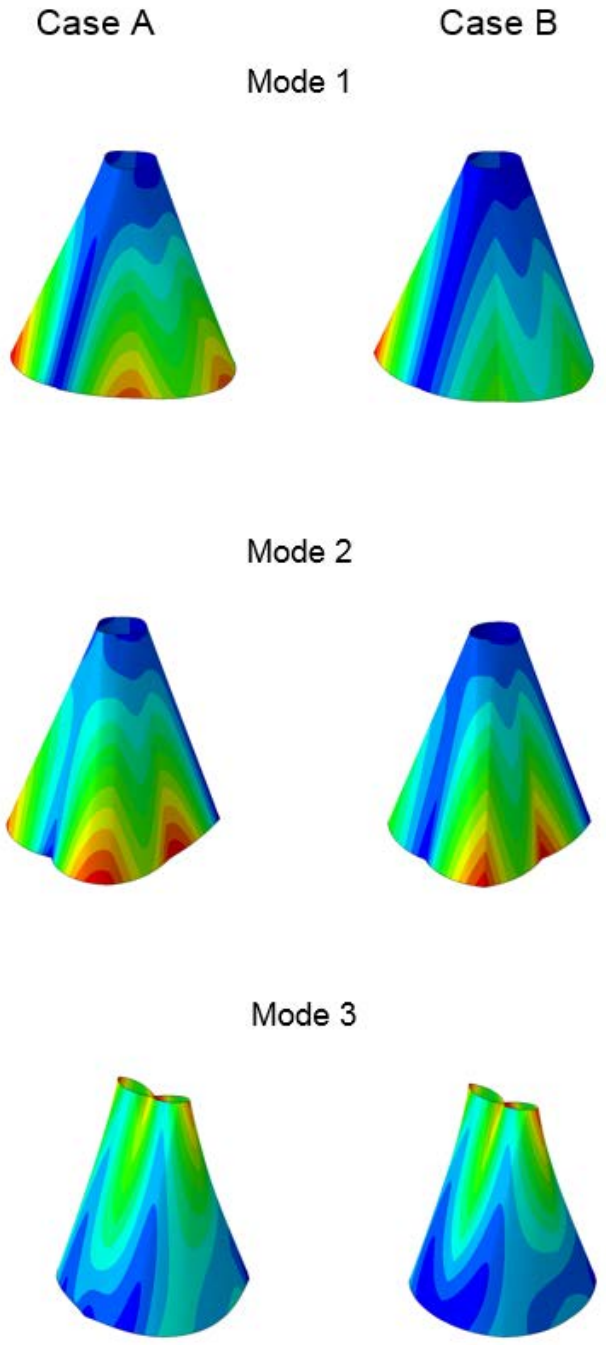

Figure 7.17: Mode shapes for the 3 first natural frequencies in the Antenna 2. For Case A, $D_{creases} = 0.1 D_{AQ,silicone}$, and for Case B, $D_{creases} = 0.01 D_{AQ,silicone}$.

Figure 7.18: Tapered Miura-ori conical shell manufactured in the laboratory, in different stages of deployment.

Chapter 8

Conclusions

This chapter concludes this thesis discussing the findings and limitations of the present work. It also proposes some potential lines of future research.

8.1 Findings and discussion

This thesis has investigated the strength in compression of a high-strain composite material, has described an alternative manufacturing technique for dual-matrix composite shells, and has proposed an application for dual-matrix composite shells to support log-periodic conical antennas for CubeSats.

High strain fiber composites can be folded into high curvatures, making them a potential candidate for energy-storing deployable structures. However, their low compressive strength due to fiber microbuckling puts them in disadvantage compared to traditional composites for applications where a load in compression is present. The use of stiffer elastomeric matrices may improve the strength in compression of this material.

Another factor that influences the strength in compression of unidirectional high-strain composites is the small variation of fiber angles with respect to the nominal fiber direction. The results presented in this thesis find that fiber angle variation increase the shear stiffness of the composite, which is the property that dominates the strength in compression of the material.

This effect was found through the experimental characterization in compression of unidirectional carbon fiber-reinforced silicone (CFRS) rods. The strength in compression found in the experiments was one order of magnitude larger than the analytical predictions of several models found in the literature. These models predict both the failure of the microstructure, i.e., microbuckling; or

the instability in compression of a homogeneous anisotropic material. All models conclude that the shear stiffness of the composite influences the critical strength in compression of the material. Therefore, it was believed that the discrepancy was due to the presence of small fiber angles in the material, which largely increased the effective shear modulus.

To investigate this effect, micrographs of the rods were taken to measure the fiber angles respect to the nominal fiber direction. Normal distributions of the fiber angles with respect to the nominal direction were obtained. The minimum local fiber angle distribution in 1 x 1 mm regions was found to have a very small mean, of 0.1^o, and a standard deviation of 0.3^o. The overall distribution throughout all the micrographs had a mean of 0.23^o and a standard deviation of 0.92^o.

In order to measure the longitudinal shear stiffness of the material, which influences the strength in compression, torsion tests were performed on rods of different lengths. The results on both lengths were consistent and repeatable, and therefore seemed independent on the end conditions. Measured values of the torsional stiffness predicted a value of the longitudinal shear stiffness much higher than the value estimated analytically, but closer to the shear stiffness estimated for the overall fiber angle distribution in the rods.

To develop a tool that allowed for the study of the effect of fiber volume fraction distribution and fiber misalignment on the CFRS rods, a periodic homogenization model was used to determine the effective properties of the composite. These properties were assumed to be linear, as the composite failure was reached at very small strains. This model assumed that the fibers were set in a square arrangement, and ignored the presence of random clustering of fibers in the cross-section.

In order to identify the effect of fiber microbuckling on the effective stiffness of the material, a non-linear homogenization model was constructed in a long RVE that represented a matrix-surrounded fiber with a microbuckling wavelength of 1 mm, which is close to the minimum wavelength observed in the experiments. The initially-imperfect RVE was compressed along the fiber direction, and the stiffness matrix of the RVE was computed at several steps to determine the influence of the strain in compression on the effective stiffness. This model was limited by the fact that only one wavelength was considered, and might have not been the correct one, as displacement measurements were taken in only part of the surface of the rod. The lack of convergence of the analysis made it difficult to obtain results for longer wavelengths. Another limitation resided in the consideration of just one fiber, instead of investigating microbuckling of a random cross-sectional

distribution of fibers. The effect of the strain in the other directions on the effective stiffness was not considered either.

These homogenization models were used to represent the linear material model in a finite element model of a CFRS rod under compression. To avoid convergence issues, the model was implemented in ABAQUS/Explicit. The results on strength in compression obtained from the finite element model were not in agreement with the experiments, assuming uniform volume fraction and parallel fibers to the nominal direction. The first instability that appeared in the model was at the element level. After reaching the strength in compression, the model generated kinks in the center and in the ends of the unconstrained regions of the rod, showing a clear dependence on the boundary conditions. Simulations for different mesh sizes showed that the dependence of the mesh size on the critical strength was small. Results were similar for the linear homogenization model and the nonlinear homogenization model with the 1-mm RVE.

Fiber angle distributions were implemented in the model through a Taylor averaging model, which estimated the effective stiffness of the material through the calculation of the expected value of the stiffness matrix for a particular the fiber angle distribution. Results for the local distribution of minimum standard deviation and the overall distribution of the CFRS rod samples were computed. Increasing the mean or the standard deviation of a fiber angle normal distribution resulted in a increase of the effective shear stiffness. Simulations show that a increase of the mean slightly decreases the strength in compression, as coupling elements in the stiffness matrix are not longer zero. An increase of the standard deviation, however, largely increases the strength in compression. This "bracing" effect of the fibers is captured with the expected value of the stiffness, however the actual interaction between fibers cannot be captured with this model.

Simulation results showed that the strength in compression found in the experiments is in agreement with results obtained for the measured local distribution of angles with minimum standard deviation. It was concluded then that the minimum local fiber angles standard deviation determines the minimum strength in compression of the material. When the overall fiber angle distribution was implemented in the model, the critical strength was found to be as high as ~ 40 MPa. Through a finite element simulation in torsion, the results from experiments were captured with the overall fiber angle distribution, confirming that the measured shear stiffness is the effective global shear stiffness of the material for the global angle distribution.

A particular use for high-strain composites is on foldable shell - membranes. These structures are characterized for being very soft out-of-plane, and for requiring external systems to ensure shape stability in the deployed configuration. A way to obtain foldable shells which have a relatively high out-of-plane stiffness is the use of dual-matrix composite shells. However, manufacturing these shells presented great difficulty due to factors such as excessive resin flow and mixing and curing inhibition. The main contribution of this thesis to the development of dual-matrix composites is the improvement of the manufacturing method, minimizing mixing and curing inhibition, through the use of a UV-cure silicone as the matrix material for the foldable lines in a fiberglass composite shell, whereas the matrix is a epoxy resin elsewhere.

The dual-matrix structural concepts created in the laboratory showed good foldability, along with a good out-of-plane stiffness and shape stability. Experimental measurements on dual-matrix hinges made of a quasi-isotropic plain weave Astroquartz, UV-cure silicone and epoxy resin showed that the pre-folded silicone hinge is as stiff as a regular epoxy. After folding, its stiffness is reduced to at least 10% of the pre-folded stiffness. This reduction of stiffness is due to the residual waviness of the fibers after being folded.

Dual-matrix composites can be useful for deployable shell structures that require high compaction. This is the case of deployable structures in CubeSats. This material may be used to support a log-periodic conical antenna for a CubeSat mission. A preliminary design of two conical structures, with origami-inspired folding patterns; the integration of the conductor in the structure, and the attachment to the CubeSat, have been described in this thesis. A vibration analysis using a conservative, linear material model for the hinge lines, which are $\sim 1\%$ softer out-of-plane than the original hinge, shows a minimum frequency of at least 3 Hz, which indicates that dual-matrix shells might be suitable for this particular application.

8.2 Future work

Understanding microbuckling strength in high-strain composites will help to ensure that these materials are applicable to deployable structures. The effect of small fiber angles observed in this thesis shows that high-strain composites could be potentially useful as flexural hinges that are able to carry small compression loads. Further work is necessary to confirm what has been observed in this thesis. Experimental work on samples designed with various small fiber angle variations is

necessary to validate these observations. Another solution to increase the strength in compression is the use of stiffer matrix materials in high-strain composites..

The material modeling can also be improved by considering the effect of random fiber clustering on the cross-section of the material. It would also be interesting to study the interaction between fibers of different angles, to see if fibers are locked during microbuckling due to this interaction. In this thesis, the fiber angle effect has been studied with an averaging model. However, it would be interesting to observe the effect the presence of random angle distributions in different regions of the material. A full non-linear homogenized material model would also be necessary to study the postbuckling behavior of the material, and to validate the results obtained in this thesis. The study of long RVEs representing different microbucking wavelengths would help to achieve a better understanding of the interaction between micro- and macro- instabilities.

Manufacturing dual-matrix composites does not have to be limited to fiberglass composites. Future work may investigate alternative ways to combine two matrices in a continuous fabric while avoiding mixing and inhibition. The folding behavior of dual-matrix composite hinges cannot only be explained by fiber microbuckling when the folds reach sharp kinks. A more detail study of the damage in both fibers and matrix, as well as the interaction between warp and weft fibers, and fibers on different laminas within the laminate, needs to be pursued. It would be also interesting to study the deployment mechanics and the stowage time influence on the deployment. The effect of cyclic loading on the hinge stiffness is another possible line for future work.

The application of dual-matrix composites for a CubeSat antenna that has been explained in this thesis is a preliminary design. Further work needs to be done on the antenna design, structure and antenna interaction with the CubeSat, and deployment mechanisms. The effect of the conductor material on the hinge behavior is expected to be small, but it also needs to be investigated.

Bibliography

[1] Agoras, M., Lopez-Pamies, O., and Ponte-Castañeda, P. Onset of macroscopic instabilities in fiber-reinforced elastomers at finite strain. *Journal of the Mechanics and Physics of Solids 57*, 11 (2009), 1828–1850.

[2] Argon, A. S. Fracture of composites. *Treatise on Materials Science & Technology 1* (1972), 79–114.

[3] Barbero, E. J. *Introduction to composite materials design*. Taylor & Francis, 1998.

[4] Barbero, E. J., and Tombin, J. A damage mechanics model for compression strength of composites. *International Journal of Solids and Structures 33*, 29 (1996), 4379–4393.

[5] BelleEnfants.co.uk. Push-up toy. `http://www.belleenfants.co.uk/shop/products/traditional-wooden-push-up-toy-soldier/`. Accessed: 3–1–2014.

[6] Belytschko, T., K, L. W., and B, M. *Nonlinear Finite Elements for Continua and Structures*. Wiley, 2000.

[7] Budiansky, B. Micromechanics. *Computers and structures 16*, 1-4 (1983), 3–12.

[8] Budiansky, B., and Fleck, N. A. Compressive failure of fibre composites. *Journal of Mechanics, Physics and Solids 41*, 1 (1993), 183–211.

[9] Campbell, D., Lake, M. S., and Mallick, K. A study of the bending mechanics of elastic memory composites. In *45th AIAA/ASME/ASCE/AHS/ASC Structures, Structural Dynamics, and Materials Conference, Palm Springs, CA* (2004), American Institute of Aeronautics and Astronautics.

[10] Christensen, H. M. Material instability for fiber composites. *ASME Journal of Applied Mechanics 61*, 2 (1994), 476–477.

[11] Conti, S., and Maggi, F. Confining thin elastic sheets and folding paper. *Arch. Rational Mech. Anal. 187* (1008), 1–48.

[12] Daniel, I. M., and Ishai, O. *Engineering mechanics of composite materials*. Oxford, 1994, second edition.

[13] Daniel, I M. Failure Mechanisms. `http://composites.northwestern.edu/research/micromechanics/failmech.htm`. Accessed: 2–4–2014.

[14] Datashvili, L., Baier, H., Wehrle, E., T, K., and Hoffmann, J. Large shell-membrane space reflectors. In *51st AIAA/ASME/ASCE/AHS/ASC Structures, Structural Dynamics, and Materials Con- ference, Orlando, Florida* (2010), American Institute of Aeronautics and Astronautics.

[15] deBotton, G., and Schulgasser, K. Bifurcation of orthotropic solids. *ASME Journal of Applied Mechanics 63* (1996), 317–320.

[16] Drapier, S., Grandidier, J.-C., and Potier-Ferry, M. Towards a numerical model of the compressive strength for long fibre composites. *Journal of Mechanics and Solids 18* (1999), 69–92.

[17] Drapier, S., Grandidier, J.-C., and Potier-Ferry, M. A structural approach of plastic microbuckling in long fibre composites: comparison with theoretical and experimental results. *International Journal of Solids and Structures 38* (2001), 3877–3904.

[18] Dyson, J. D. A survey of the very wide band and frequency independent antennas – 1945 to the present. *Journal of Research of the National Bureau of Standards 66*, 1 (1962), 1–6.

[19] Fleck, N. A. Compressive failure of fiber composites. *Advances in Applied Mechanics 33*, 6/7 (1997), 43–117.

[20] Francis, W. H., Lake, M. S., and Mayes, J. S. A review of classical fiber microbuckling analytical solutions for use with elastic memory composites. In *47th*

AIAA/ASME/ASCE/AHS/ASC Structures, Structural Dynamics, and Materials Conference, Newport, Rhode Island (2006), American Institute of Aeronautics and Astronautics.

[21] Francis, W. H., Lake, M. S., Schultz, M. R., Campbell, D., Dunn, M., and Qi, H. J. Elastic memory composite microbuckling mechanics: Closed-form model with empirical correlation. In *48th AIAA/ASME/ASCE/AHS/ASC Structures, Structural Dynamics, and Materials Conference, Honolulu, Hawaii* (2007), American Institute of Aeronautics and Astronautics.

[22] Gattas, J. M., Wu, W., and You, Z. Miura-base rigid origami: parameterizations of first level derivative and piecewise geometries. *Journal of Mechanical design 135* (2013).

[23] Gent, A. N. Elastic instabilities in rubber. *International Journal of Non-Linear Mechanics 40* (2005), 165–175.

[24] Geymonat, G., Müller, S., and Triantafyllidis, N. Homogenization of nonlinearly elastic materials, microscopic bifurcation and macroscopic loss of rank-one convexity. *Archive for Rational Mechanics and Analysis 122* (1993), 231–290.

[25] Grimmett, G., and Stirzaker, D. *Probability and Random Proceses*. Oxford, 2001.

[26] Hexcel. AS4 carbon fiber. `http://www.hexcel.com/Resources/DataSheets/Carbon-Fiber-Data-Sheets/AS4.pdf`. Accessed: 5–1–2012.

[27] Jelf, P. M., and Fleck, N. A. Compression failure mechanisms in unidirectional composites. *Journal of Composite Materials 26*, 18 (1992), 2706–2726.

[28] Joe Gattas. Rigid Origami Toolbox. `http://joegattas.com/rigid-origami-toolbox/`. Accessed: 3–1–2014.

[29] Kyriakides, S., Arseculeratne, R., Perry, E. J., and Liechti, K. M. On the compressive failure of fiber reinforced composites. *International Journal of Solids and Structures 32*, 6/7 (1995), 689–738.

[30] Loctite. Loctite 5055. `https://tds.us.henkel.com/NA/UT/HNAUTTDS.nsf/web/88C664FFAF9001438525775E006CE0B0/$File/5055-EN.pdf`. Accessed: 3–14–2013.

[31] Lopez Jimenez, F. Mechanics of thin carbon fiber composites with a silicone matrix. *Dissertation (Ph.D.), California Institute of Technology* (2011).

[32] Lopez Jimenez, F. Modeling of soft composites under three-dimensional loading. *Composites Part B: Engineering 59* (2014), 173–180.

[33] Lopez Jimenez, F., and Pellegrino, S. Failure of carbon fibers at a crease in a fiber-reinforced silicone sheet. *ASME Journal of Applied Mechanics 80*, 1 (2012).

[34] Lopez Jimenez, F., and Pellegrino, S. Folding of fiber composites with a hyperelastic matrix. *International Journal of Solids and Structures 49*, 3/4 (2012), 395–407.

[35] Lopez-Pamies, O., and Ponte-Castañeda, P. On the overall behavior, microstructure evolution, and macroscopic stability in reinforced rubers at large deformations. *Journal of the Mehanics and Physics of Solids 54* (2000), 831–863.

[36] Mallikarachchi, H. M. Y. C., and Pellegrino, S. Quasi-static folding and deployment of ultrathin composite tape-spring hinges. *Journal of Spacecraft and Rockets 48*, 1 (2011).

[37] Mathworks. Hough transform. `http://www.mathworks.com/help/images/detect-lines-in-images.html`. Accessed: 3–1–2014.

[38] Mejia-Ariza, J. M., Guidanean, K, Murphey, T. M., and Biskner, A. Mechanical characterization of l'garde elastomeric resin composite materials. In *51st AIAA/ASME/ASCE/AHS/ASC Structures, Structural Dynamics, and Materials Conference, Orlando, Florida* (2010), American Institute of Aeronautics and Astronautics.

[39] Mejia-Ariza, J. M., and Murphey, T. W. Flexure hinge and strut design for concentrated strain deployable trusses. In *49th AIAA/ASME/ASCE/AHS/ASC Structures, Structural Dynamics, and Materials Conference* (2008), American Institute of Aeronautics and Astronautics.

[40] Merodio, J., and Ogden, R. W. Material instabilities in fiber-reinforced nonlinearly elastic solids under plane deformation. *Archives of Mechanics 54*, 5-6 (2002), 525–552.

[41] Merodio, J., and Ogden, R. W. Instabilities and lost of ellipticity in fiber-reinforced compressible non-linearly elastic solids under plane deformation. *International Journal of Solids and Structures 40* (2003), 4707–4727.

[42] Miura, K. Method of packaging and deployment of large membranes in space. *The Institute of Space and Astronautical Science report 618* (1985).

[43] Mix, A. W., and Giacomin, A. J. Standarized polymer durometry. *Journal of Testing and Evaluation 39*, 4 (2011), 1–10.

[44] Murphey, T. W. Large strain composite materials in deployable structures. In *ICCM-17, 17th International Conference on Composite Materials, Edimburgh, Scotland* (2009), International Conference on Composite Materials.

[45] Murphey, T. W., Meink, T., and Mikulas, M. M. Some micromechanics considerations of the folding of rigidizable composite material. In *42nd AIAA/ASME/ASCE/AHS/ASC Structures, Structural Dynamics, and Materials Conference, Seattle, WA* (2001), American Institute of Aeronautics and Astronautics.

[46] Nikon. NIS–Elements imaging software. `http://www.nikon.com/products/instruments/lineup/bioscience/img_soft/index.htm`. Accessed: 3–1–2014.

[47] Olson, G. M., Pellegrino, S., Costantine, J., and Banik, J. Structural architectures for a deployable wideband uhf antenna. In *53rd AIAA/ASME/ASCE/AHS/ASC Structures, Structural Dynamics and Materials Conference, 23-26 April 2012 Honolulu* (2012), American Institute of Aeronautics and Astronautics.

[48] Parnes, R., and Chiskis, A. Buckling of nano-fibre reiforced composites: a re-examination of elastic buckling. *Journal of the mechanics and physics of solids 50* (2002), 855–870.

[49] Peel, L. D. Fabrication and testing of orthotropic and extreme poisson's ratio elastomer composites. In *SAMPE 2008, Long Beach, CA* (2008), Society for the Advancement of Material and Process Engineering.

[50] Peel, L. D., Mejia, J., Narvaez, B., Thompson, K., and Lingala, M. Development of a simple morphing wing using elastomeric composites as skins and actuators. *ASME Journal of Mechanical Design 131*, 9 (2009).

[51] Pinte-Castañeda, P. Second-order homogenization estimates for nonlinear composites incorporating field fluctuations. *Journal of the Mehanics and Physics of Solids 50* (2002), 737–757.

[52] Ponte-Castañeda, P. Exact second-order estimates for the effective mechanical properties of nonlinear composite materials. *Journal of the Mehanics and Physics of Solids 44* (1996), 827–862.

[53] Ponte-Castañeda, P., and Tiberio, E. A second-order hmogenization procedure in finite elasticity and applications to black-filled elastomers. *Journal of the Mehanics and Physics of Solids 48* (2000), 1389–1411.

[54] Robbins, D. Analysis of fiber microbuckling in elastomeric composites. In *51st AIAA/ASME/ASCE/AHS/ASC Structures, Structural Dynamics and Materials Conference, Orlando, Florida, April 2010* (2010), American Institute of Aeronautics and Astronautics.

[55] Rosen, B. W. *Mechanics of composite strenghtening.* Fiber composite materials, American Society for Metals, Metals Park, Ohio, 1965.

[56] Rudykh, S., and deBotton, G. Instabilities of hyperelastic fiber composites: micromechanical versus numerical analyses. *Journal of Elasticity 106* (2011), 123–147.

[57] Saito, K., Pellegrino, S., and Nojima, T. Manufacture of arbitrary cross-section composite honeycomb cores based on origami techniques. In *Proceedings of the ASME 2013 IDETC/CIE, Portland, OR, August 2013* (2013), American Society of Mechanical Engineering.

[58] Sickingger, C., and L, H. Deployment strategies, analysis and tests for the cfrp booms of a solar sail. In *European Conference on Spacecraft Structures, Materials and Mechanical Testing* (2002).

[59] Soykasap, O. Micromechanical models for bending behavior of woven composites. *Journal of Spacecraft and Rockets 43*, 5 (2006), 1093–1100.

[60] Sun, C. T., and Vaidya, R. S. Prediction of composite properties from a representative volume element. *Composites Science and Technology 56* (1996), 171–179.

[61] Sutton, M. A., Orteu, J. J., and Schreier, H. W. *Image Correlation for Shape, Motion and Deformation Measurements*. Springer, 2009.

[62] Timoshenko, S. P., and Gere, J. M. *Probability and random proceses*. McGraw-Hill, New York, second edition, 1961.

[63] Todoroki, A., Kumagai, K., and Matsuzaki, R. Self-deployable space structure using partially flexible cfrp with sma wires. *Journal of Intelligent Material Systems and Structures 20* (2009), 1415–1424.

[64] Triantafyllids, N., and Abeyaratne, R. Instabilities of a finitely deformed fiber-reinforced elastic material. *ASME Journal of Applied Mechanics 50* (1983), 149–156.

[65] Triantafyllids, N., and Schnaidt, W. C. Comparison of microscopic and macroscopic instabilities in a class of two-dimensional periodic composites. *Journal of Mechanics and Physics of Solids 41*, 9 (1993), 1533–1565.

[66] Waas, A. M., Babcock, C. D. J., and Knauss, W. G. Prediction of composite properties from a representative volume element. *ASME Journal of Applied Mechanics 57* (1990).